INVESTIGATION OF ELECTROCATALYTIC PERFORMANCE OF PRUSSIAN BLUE ANALOGUES FOR WATER SPLITTING

A THESIS SUBMITTED TO

THE GRADUATE SCHOOL OF ENGINEERING AND SCIENCE OF

BILKENT UNIVERSITY

IN PARTIAL FULFILLMENT OF THE REQUIREMENTS FOR THE

DEGREE OF

MASTER OF SCIENCE IN

CHEMISTRY

By

Elif Pınar ALSAÇ

September 2017

INVESTIGATION OF ELECTROCATALYTIC PERFORMANCE OF PRUSSIAN BLUE ANALOGUES FOR WATER SPLITTING

By Elif Pınar ALSAÇ

September 2017

We certify that we have read this thesis and that in our opinion it is fully adequate, in scope and in quality, as a thesis for the degree of Master of Science.

_____

Ferdi Karadaş (Advisor)

_____

Ömer Dağ

_____

Burak Ülgüt

_____

Emren Nalbant Esentürk

_____

Yavuz Dede

Approved for the Graduate School of Engineering and Science:

_____

Ezhan Karaşan

Director of the Graduate School

ABSTRACT

INVESTIGATION OF ELECTROCATALYTIC PERFORMANCE OF PRUSSIAN BLUE ANALOGUES FOR WATER SPLITTING

Elif Pınar ALSAÇ

M.S. in Chemistry
Advisor: Ferdi KARADAŞ
September 2017

Research on H_2 production has recently been directed to the development of cost-efficient and robust heterogeneous catalysts for splitting of water. While several Prussian blue analogues (PBAs) have been investigated as water oxidation catalysts, the field lacks a comprehensive study that focuses on the design of the ideal PBA for efficient water oxidation. Herein this thesis, a series of PBAs with different cyanide precursors were investigated to study the effect of hexacyanometal group to their electrocatalytic catalytic water oxidation activities. Cyclic voltammetry, chronoamperometry, and chronopotentiometry measurements reveal the close relation between the electron density of electroactive cobalt sites and electrocatalytic activity, which is also confirmed by Infrared and XPS studies. pH dependent cyclic voltammetry studies were also performed to gain insight about the catalytic mechanism and electronic structure of cyanide-based systems, to identify possible intermediates, and assign the rate-determining step of the process.

In addition, a N-donor ligand, 1-heptyl 4-(4 pyridyl) pyridinium bromide, was used to prepare a new pentacyanoferrate complex. This complex was used to make a new series of PB analogues to investigate the effect of the change in the morphology to electrocatalytic water oxidation performance. Synthesis, characterization, and electrochemical experiments were performed to investigate electrocatalytic properties of PB analogues. With this synthesis route, the electroactive cobalt sites are increased approximately two-fold. It is observed that amorphous nature has positive impact on the catalytic activity when compared to cobalt hexacyanoferrates. A current density of 1 $mA.cm^{-2}$ was achieved at an overpotential of 421 mV, which is much lower than those obtained with metal hexacyanometalates.

Given the promising catalytic activities of several cobalt-based systems and the robustness of Prussian blue analogues in harsh catalytic processes including water oxidation, a Co-Co Prussian blue analogue was investigated as a Hydrogen evolution catalyst for the first time. Co-Co Prussian Blue modified FTO electrode demonstrated a significant Hydrogen evolution activity with an onset overpotential of 257 mV, a Tafel slope of 80.2 $mV.dec^{-1}$, and a turnover frequency of 0.090 s^{-1} at an overpotential of 250 mV. Comparative XPS, Infrared, and XRD studies performed on pristine and post-catalytic electrodes confirm the stability of the catalyst.

Keywords**:** Energy, Water Oxidation, Prussian Blue, Water Oxidation Catalyst, Hexacyanide, Pentacyanide, Cyanide, Water Reduction Catalyst, Hydrogen Evolution Catalyst, Electrocatalysis.

ÖZET

PRUSYA MAVİSİ TÜREVLERİNİN SUYUN AYRIŞMASI İÇİN ELEKTROKATALİTİK AKTİVİTELERİNİN İNCELENMESİ

Elif Pınar ALSAÇ

Kimya, Yüksek Lisans

Tez Danışmanı: Ferdi KARADAŞ

Eylül 2017

Hidrojen üretimindeki araştırmalar son zamanlarda suyun bölünmesi için uygun maliyetli ve dayanıklı heterojen katalizörlerin geliştirilmesine yönelmiştir. Su oksitleyen katalizörler olarak çeşitli Prusya mavisi türevleri araştırılmış olmasına rağmen, su oksidasyonu için verimli ve ideal Prusya mavisi türevlerinin dizaynına odaklanan kapsamlı bir araştırma yapılmamıştır. Bu tezde, farklı siyanür prekursörleri olan bir dizi PBA, hekzasiyanometal grubunun elektrokatalitik su oksidasyonu aktivitelerine olan etkisi araştırılmıştır. Çevrimsel voltametrik, kronoamperometrik ve kronopotansiyometre ölçümleri, elektroaktif kobalt alanlarının elektron yoğunluğu ile elektrokatalitik aktivite arasındaki yakın ilişkiyi ortaya çıkarmakta ve bu çalışmalar da Infrared ve XPS gibi karakterizasyon teknikleri ile doğrulanmıştır. Siyanür bazlı sistemlerin katalitik mekanizması ve elektronik yapısı hakkında fikir edinmek, muhtemel ara stepleri tanımlamak ve sürecin hız kısıtlama basamağını atamak için pH bağımlı çevrimsel voltametri çalışmaları da yapılmıştır.

Bu çalışmaya ek olarak, morfolojideki değişikliğin, su oksidasyon kabiliyetinde amorf pentasiyanoferrat koordinatlı PB üretmek için 1-heptil 4- (4-piridil) piridinyum bromür olan bir N verici ligand kullanılarak etkisi araştırılmıştır. PB için katalitik aktivite üzerindeki gelişmeleri gözlemlemek için sentez, karakterizasyon ve elektrokimyasal deneyler gerçekleştirilmiştir ve sonuç olarak bu sentez yoluyla, elektroaktif kobalt merkezleri yaklaşık iki kat artmıştır. Amorf yapının, kobalt heksasiyanoferratlara kıyasla, katalitik aktivite üzerinde olumlu etkisi olduğu gözlemlenmiştir. 1 $mA.cm^{-2}$'lik bir akım yoğunluğu için metal heksasiyanometalatlardan çok daha düşük olan 421 mV aşırı potansiyel elde edilmiştir.

Çeşitli kobalt bazlı sistemlerin umut verici katalitik aktiviteleri ve prusya mavisi türevlerinin su oksidasyonu da dahil olmak üzere katalitik proseslerde dayanıklılığı göz önüne alındığında, Co-Co Prusya mavisi türevi, ilk kez bir hidrojen çıkışı katalizörü olarak kullanılmıştır. Co-Co Prusya Mavisi modifiyeli elektrot ile, 250 mV'lık bir aşırı potansiyel, 80.2 $mV.dec^{-1}$'lik bir Tafel eğimi ve 0.090 s^{-1}'lik bir devir frekansı ile önemli bir katalitik aktivite gözlemlenmiştir. Katalitik aktivite öncesi ve sonrası karşılaştırmalı XPS, Infrared ve XRD çalışmaları da katalizörün stabilizesini doğrulamıştır.

***Anahtar Sözcükler*:** Enerji, Suyun Oksitlenmesi, Prusya mavisi, Su oksitleyici katalizör, Hekzasiyanür, Pentasiyanür, Siyanür, Su redükleyici katalizör, Hidrojen eldesi, Electrokataliz.

ACKNOWLEDGEMENT

First, I would like to express my deepest gratitude to my advisor Asst. Prof. Ferdi Karadaş for not only for his excellent supervising in the project but also for his enthusiasm, motivation, patience, kindness and trust over the course of my studies. He gave me sufficient time and opportunity to explore new areas throughout my research. I would like to thank him for encouraging me to go to Toronto under tough circumstances. I am so grateful to have the chance to work with him. I will always remember what he has taught me, and follow his lead.

I am sincerely thankful to the examining committee members, Prof. Ömer Dağ, Asst. Prof. Burak Ülgüt, Assoc. Prof. Emren Esentürk, and Assoc. Prof. Yavuz Dede for their valuable time and feedback. I would like to thank The Scientific and Technological Research Council of Turkey, TÜBİTAK, for the financial support under project no: 215Z249.

I am thankful to all of present and former members of Karadaş group, Dr. Satya Vijaya Kumar Nune, Dr. Emine Ülker, Zeynep Kap, Sina Sadigh Akbari, Merve Aksoy, Gamze Ulusoy, Ceyla Asker, Emine Ayşe Turhan, Aysun Başaran, and Büşra Altınsoy, for providing a peaceful and friendly environment. Especially, I would like to express my gratitude to Dr. Satya Vijaya Kumar Nune for his endless encouragements and friendship. I also would like to thank Dr. Emine Ülker for her guidance, and contributions to works.

My special thanks to my friends in Department of Chemistry, Gülbahar Saat, Elif Özdemir, Merve Tohumeken, Aybegüm Samast, Muammer Yaman, Can Berk Uzundal, Ezgi Yılmaz, Emre Köken, Nüveyre Canbolat, Özge Bayrak, and Canan Erdoğan for their valuable friendships over the years.

Last but not the least, I would like to thank my parents Meryem and Resul Alsaç for their sacrifices and patience throughout my education, and unconditional love. To my sister Filiz, I say thank you for all of your support and understanding and also help in editing the thesis. I thank my brother Ümit for his all kinds of assistance during my education, he has been a good role model for me. Glad to have you all.

To my family and my beloved niece Elif

"As you start to walk on the way, the way appears."

Rumi

TABLE OF CONTENTS

LIST OF FIGURES

LIST OF TABLES

Abbreviations

υ	: Potential scan rate
Γ	: Surface coverage (surface concentration)
μ	: Micro
η	: Overpotential
λ	: Wavelength
ν	: Wavenumber
A	: Area
A	: Ampere
Å	: Angstrom
Ag/AgCl	: Silver/Silver Chloride Reference Electrode
C	: Coulomb
CA	: Chronoamperometry
CP	: Chronopotentiometry
CPE	: Controlled Potential Electrolysis
CV	: Cyclic voltammetry
DMF	: N, N- Dimethylformamide
E	: Potential
E^o	: Standard redox potential
$E_{1/2}$	: Half-wave potential
eV	: Electron volts
$E_{1/2}$	: Half-wave potential
EDAX	: Electron Dispersive X-ray spectroscopy

F : Faraday's constant

FTIR : Fourier Transform Infrared Spectroscopy

FTO : Fluorine doped Tin Oxide

GI-XRD : Grazing Incidence X-Ray Diffraction

HER : Hydrogen Evolution Reaction

HPPB : 1-heptyl 4-(4 pyridyl) pyridinium bromide

I : Current

i_o : Exchange Current Density

j_o : Current Density

K : Kelvin

KPi : Potassium Phosphate Buffer Solution

M : Molarity

NHE : Normal Hydrogen Electrode

PB : Prussian Blue

PBA : Prussian Blue Analogue

PS : Photosensitizer

PXRD : Powder X-Ray Diffraction

RT : Room Temperature

SEM : Scanning Electron Microscopy

TOF : Turnover Frequency

TON : Turn Over Number

XPS : X-Ray Photoelectron Spectroscopy

XRD : X-ray Diffraction

WOC : Water Oxidation Catalysis

WRC : Water Reduction Catalysis

XPS : X-ray Photoelectron Spectroscopy

CHAPTER 1

INTRODUCTION

1.1. TRANSITION METAL CYANIDE CHEMISTRY

1.1.1. The Cyanide Ion (CN^-) as a Ligand

There has been ample research on cyanide based materials due to unique binding mode of the cyanide group to metal ions. The cyanide ion is one of the most well-known and frequently used ligands to form coordination complexes with dimensionalities ranging from 0D (molecular) to 3D. Its unique spectroscopic properties and strong bonding to metal ions lead to the formation of robust cyanide based coordination compounds, which have potential applications in electronics, magnetism, and catalysis. The major feature of cyanide ion is its capability to stabilize metal ions with a wide range of oxidation states and stereochemical configurations.[1]–[3]

Cyanide ion is a negatively charged ligand and has a tendency to form a strong sigma (σ) bond with a metal ion. There is a lone pair effective on both carbon and nitrogen. It is isoelectronic with N_2, CO, and NO^+ and the electronic configuration of the ground state of CN^- is $(1\sigma)^2$ $(2\sigma)^2$ $(3\sigma)^2(4\sigma)^2(1\pi)^4(5\sigma)^2$ and the correspondence of this configuration is triple bond consisting of 1 σ-bond and 2 π- bonds between C and N atoms.[4] Figure 1.1 shows the molecular orbital diagram of the cyanide ion. 5σ orbital is the highest occupied molecular orbital (HOMO) and $2\pi^*$ is lowest unoccupied molecular orbital (LUMO).

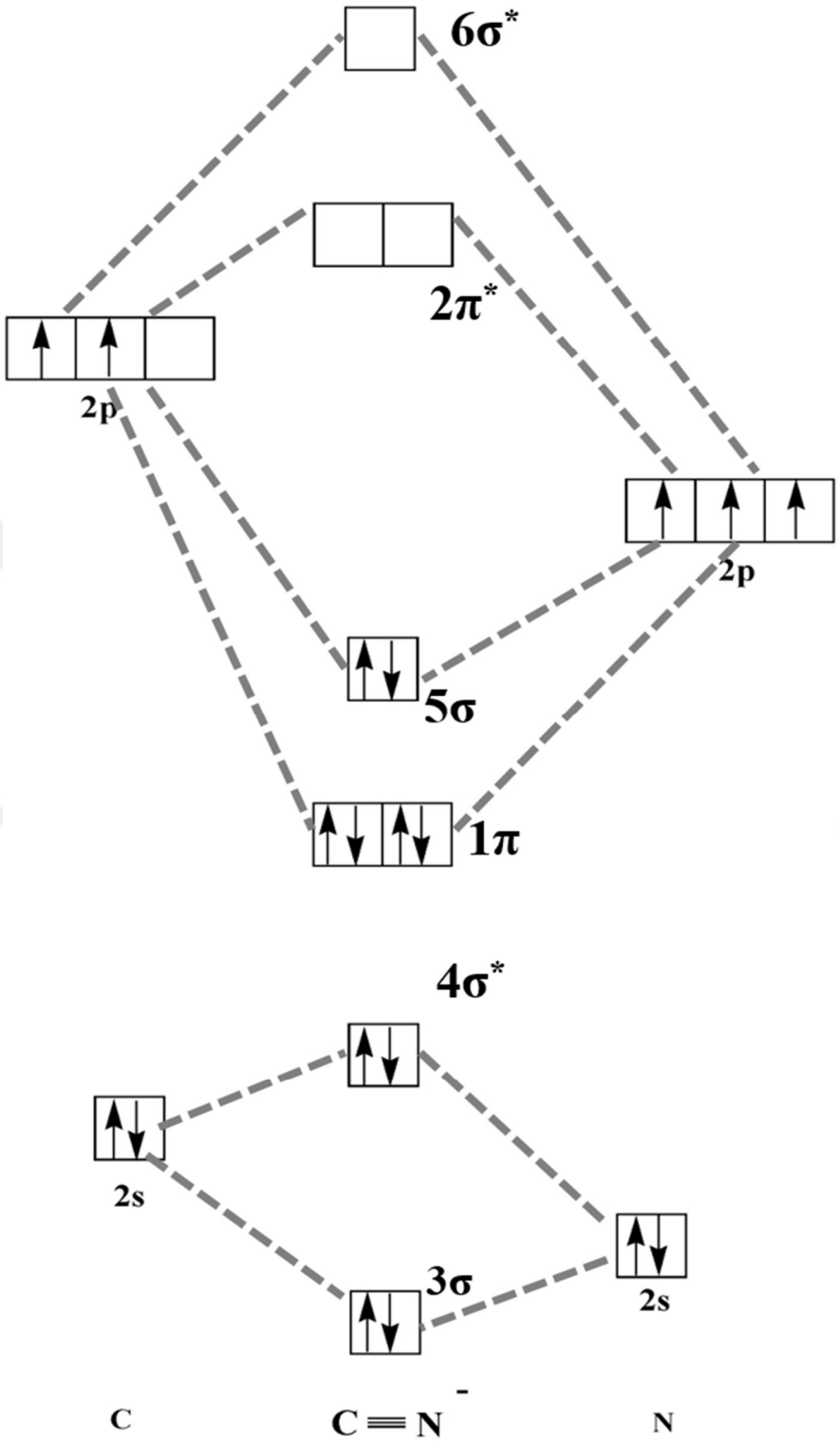

Figure 1. 1. Molecular orbital diagram of cyanide ion

When cyanide ions binds to a transition metal, the metal ion can coordinate up to eight cyanide ligands and its oxidation state can vary from zero to +5.[5] The cyanide can be both monodentate and bidentate. The binding modes of cyanide ligand are displayed in Figure 1.2.

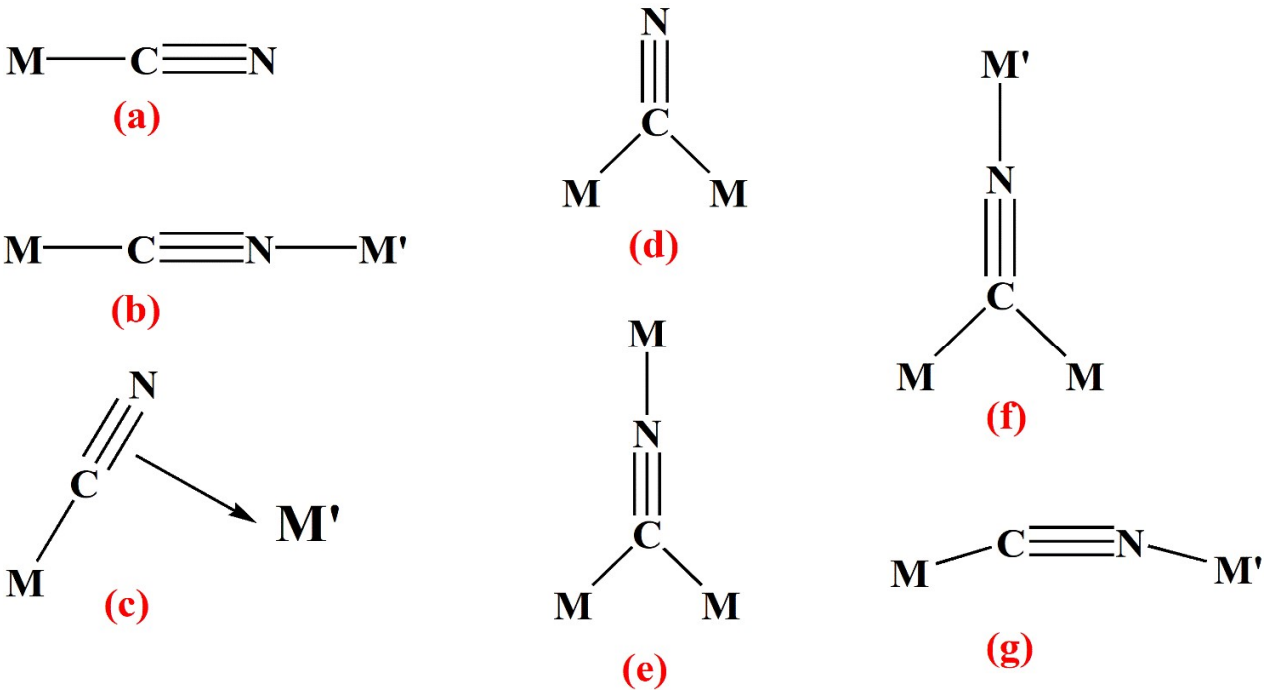

Figure 1. 2. Binding modes of cyanide ligand with metal ions

Cyanide ligand is a strong-field ligand, when carbon atom is used for coordination rather than the nitrogen atom .[6] Therefore, the two most common binding modes of cyanide ligand are linear C-bound terminal binding modes (Figure 1.2(a) and 1.2(b)). The other binding modes in Figure 1.2. are less frequent.[1]

The distance of the triple bond is reported as 1.16 Å and vibrational frequency of $\upsilon(CN^{-1})$ is obtained at 2080 cm^{-1} for free cyanide ion aqueous phase.[7] When it reacts with a metal, two types of interactions are observed; i) a σ- donation from the ligand to the metal ion and ii) a π back donation from the metal to the cyanide ligand.. The schematic representation of σ- donation and π- back bonding ability of cyanide ion is illustrated in Figure 1.3. The σ- donation and π- back

bonding ability of cyanide ion contributes to the stabilization of both high and low oxidation numbers it means that this ability allows it to have several oxidation states. [5] It is well-known that the σ-donation ability of cyanide ligand predominates the π- back bonding ability of the ligand mainly due to its negative charge and σ* orbital is used for the interaction. Therefore, the interaction between the metal ion and the cyanide ligand leads to a stronger CN bond, which leads to a shift in CN stretch to higher frequencies.

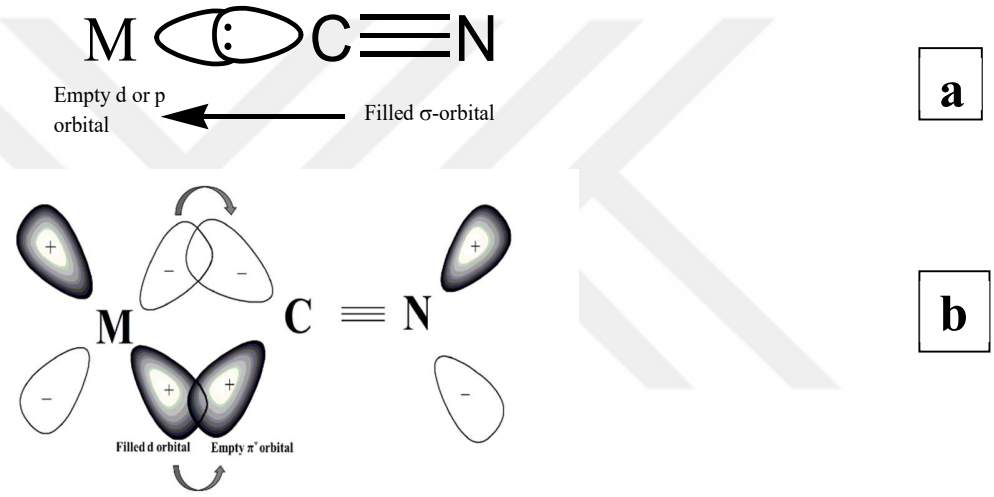

Figure 1. 3. a) σ- donation and b) π- back bonding ability of cyanide ion

According to previous studies, the change in cyanide stretching frequency can be attributed to several factors such as oxidation state, electronegativity, and coordination number. When the oxidation state decreases the metal becomes less electropositive, CN bonds weakens, which results in a decrease the CN stretch. Dunbar et al. clearly stated that the frequency of the vibration stretch of cyanide increases further when the terminal cyanide ligand forms a linear bridging with metals i.e, M-CN-M'.[6] The main reason for this behavior has been well explained in previous studies.

This shift can be because of kinematic coupling when the second metal is attached and also the N lone pair exhibits an antibonding character.[8]–[10] The cyanide ion is a very strong field ligand and this ability leads to the formation of low-spin octahedral [$M^{II}(CN)_6$] or tetrahedral [$Co^{II}(CN)_4$] coordination compounds while it is high-spin case for nitrogen binding metal ion.[11]

1.1.2. Prussian Blue Analogues (PBAs)

Prussian blue is one of the oldest synthetic coordination compounds known, while the scientific literature on PB compounds has emerged particularly in the last 25 years.[6]

Despite the lack of earlier scientific studies on PB, it has a noteworthy history. It is the first known coordination compound. PB, also known as ferric hexacyanoferrate ($Fe_4[Fe(CN)_6]_3$), was discovered as a synthetic pigment for paintings and fabrics by German artist Johann Jacob Dieshbach accidentally in early 1700s.[12] The first synthesis was as follows: Cochineal red pigment with alum was extracted with iron sulfate and potash. However, potash was contaminated with hexacyanoferrate and a particular blue colored colloid was obtained when iron sulfate solution was added.[13] The synthesis procedure was reported in 1724 for the first time by an English naturalist and geologist John Woodward in the journal of *Philosophical Transactions of the Royal Society*.[14] After a while the pigment was used in many paintings and photographs in with the beginning of the 18th century by many artists including Van Gogh, Hokusai, Monet, and Picasso (Figure 1.4) because of its valuable properties such as stability, insensitivity to light, and inexpensiveness compared to its alternatives.

Figure 1. 4. Under the Wave off Kanagawa (Kanagawa oki nami ura). Katsushika Hokusai (1830-1832). Polychrome woodblock print, color and ink are on the paper, 25.7 x 37.9 cm. Both PB and traditional indigo dyes were used to show an indirect nuance in painting. [15]

1.1.2.1. Structure of Prussian Blue

The original PB, $Fe_4[Fe(CN)_6]_3 . xH_2O$ is a mixed- valence compound, which holds both high spin +3 and low spin +2 oxidation states of iron. The reaction of the synthesis of original PB is:

$$\mathbf{4FeCl_3\ (aq) + 3K_4[Fe(CN)_6]\ (aq)} \xrightarrow{xH_2O} \mathbf{[Fe^{II}Fe^{III}(CN)_6].\ xH_2O + 12KCl\ (aq)}$$

The crystal structure of Prussian blue and some of its analogues were first studied by Keggin and Milles with the help of Ardeer Factory X-Ray Analysis.[16] Then Ludi et al. studied the crystal structure of PB more extensively. The growth of fine crystals of PB is rather difficult due to the high rate of the reaction. Ludi et al. came up with a novel method to crystallize PB. The compound was dissolved in 10 M HCl solution and due to very slow diffusion of water, they could obtain the

crystal compound in three months and determined the exact structure of the crystal.[17] They reported the crystal structure of PB as P*m*3*m* by using electron and neutron diffraction method in 1977. In addition, the pattern reveals that the crystallographic radius of CN^- specifically, the distance between Fe^{2+} ion and C atom is 1.92 Å and the distance between Fe^{3+} and nitrogen is 2.03 Å in this Fe^{2+}/Fe^{3+} mixed valence coordination network.[17] Two different octahedral metal centers are present in the unit cell, which are used to construct a face centered cubic cell (fcc). In this case, the lattice structure of PB has been constructed where Fe^{2+} ions are bound through carbon atoms while Fe^{3+} is bonded with nitrogen. [18] Because of 4:3 valence ratio, one fourth of hexacyanoferrate sites are vacant and in order to proceed the charge neutrality and thus the octahedral vacant spaces are filled with water molecules at empty nitrogen sites.[19]

Furthermore, the mixed valency in the PB structure allows it to have many combinations of the transition metals in the general structure of $M[M'(CN)_6].xH_2O$ with metals having different oxidation states. These metal hexacyanometalate structures are isostructural with the original Prussian blue one. The general fcc structure of MHCMs is shown in Figure 1.5.

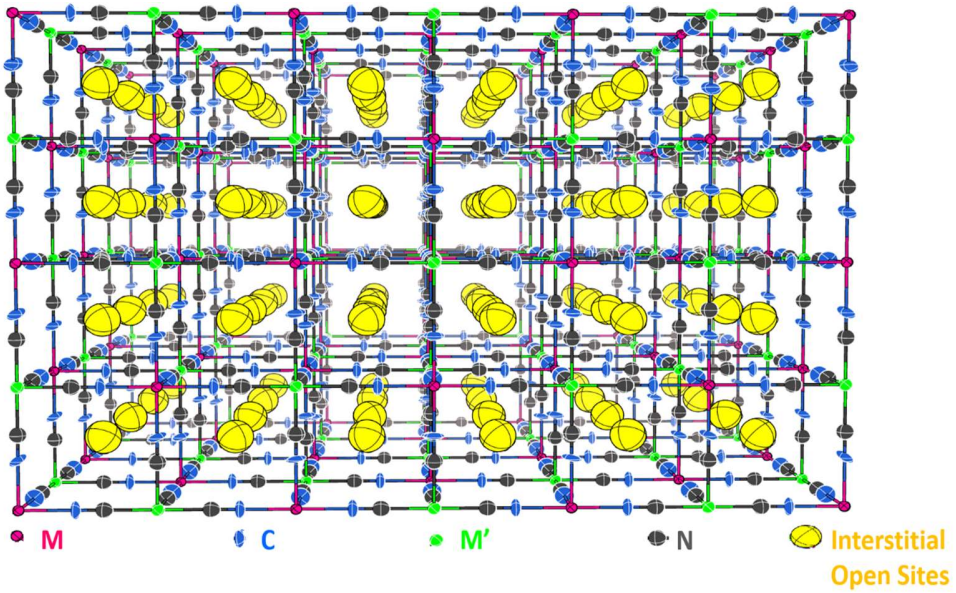

Figure 1. 5. The structure of PB type fcc unit cell structure

PBAs could be both soluble and insoluble in water depending on the presence of counter cation (K^+, Na^+, Li^+ Ca^{2+} etc.) in the structure. The soluble form includes counter cation in order to compensate the charge neutrality. The alkali metal cations are located at the cavities of interstitial open sites of the three dimensional PB structure.[13] Even though the terminology is used to distinguish two types of PB analogues, they are, in fact, highly insoluble in water.[20]

Recent investigations on Prussian blue and its analogues have pushed the scientific community to extensively study for a wide range of applications involving magnetism,[21], [22] energy storage and conversion,[23]–[25] electrochromic materials,[26] biosensensing and biomedical applications,[27], [28] electrode materials,[29] catalytic applications,[30] and gas separation[31], [32] due to their unique properties such as rigidity, specific redox properties, ionic conductivities, immense thermal and chemical stability, porosity, easy preparation, and inexpensiveness.[33]

1.1.3. The Pentacyanoferrate Chemistry

Iron is considered to be one of the most common metals among transition metal cyanide complexes. Other than Prussian blue, mono- substituted cyanoferrates have also been used extensively to synthesize various inorganic complexes. Compounds that are synthesized from pentacyanoferrates have first been prepared in the beginning of 20^{th} century while most of the systematic studies emerged after 1970s.

One of the common substituted pentacyanoferrate complex is sodium nitrosopentacyanoferrate (II) complex, $Na_2[Fe(CN)_5NO].2H_2O$, which is a good precursor for many other pentacyanoferrate (II) complexes. Swinehart reviewed the structural and spectral properties of the complex in detail.[34] In this complex the nitrosyl group determines the bonding

properties of the complex rather than cyanide group.[35] Hofmann reported the synthesis methods and characterization of substituted $[Fe(CN)_5L]^{3-}$ (L: NH_3, H_2O, NO_2, or SO_3^{2-}) by starting with nitrosopentacyanoferrate (II).[36]

The pentacyanoferrate complexes could be easily prepared from pentacyanoaminoferrate complex ($[Fe(CN)_5NH_3]^{3-}$ which is a widely used precursor in inorganic syntheses. Aminopentacyanoferrate (II), $Na_3[Fe(CN)_5NH_3].3H_2O$, is very hygroscopic complex and it can be synthesized from commercially available $Na_2[Fe(CN)_5NO].2H_2O$ complex. The properties of $Na_3[Fe(CN)_5NH_3].3H_2O$ have been investigated in detail both spectroscopically and electrochemically four decades before.[37]–[40] It is used as a precursor when it is substituted with N- donor ligands like pyridine, pyrazine bipyridine because of NH_3 ligand's labile character. (Figure 1.6). [41] An increment in cyanide stretch is observed when one of the cyanide ligands is substituted with NH_3 as observed by comparing the Infrared spectra of $[Fe(CN)_5NH_3]^{3-}$ and $[Fe(CN)_6]^{4-}$ complexes. The cyanide stretches of $[Fe(CN)_6]^{4-}$ is 2010 cm^{-1} on the other hand ν(CN) of $[Fe(CN)_5NH_3]^{3-}$ is 2033 cm^{-1}. This phenomenon could be explained with CN stretching modes of the complexes. NH_3 ligand is a σ-donor and CN^- is both σ- donor and π- acceptor ligand. For this reason, in the $[Fe(CN)_5NH_3]^{3-}$ complex, there is no π- back donation ability, this is because there is a blue shift in CN stretching band.

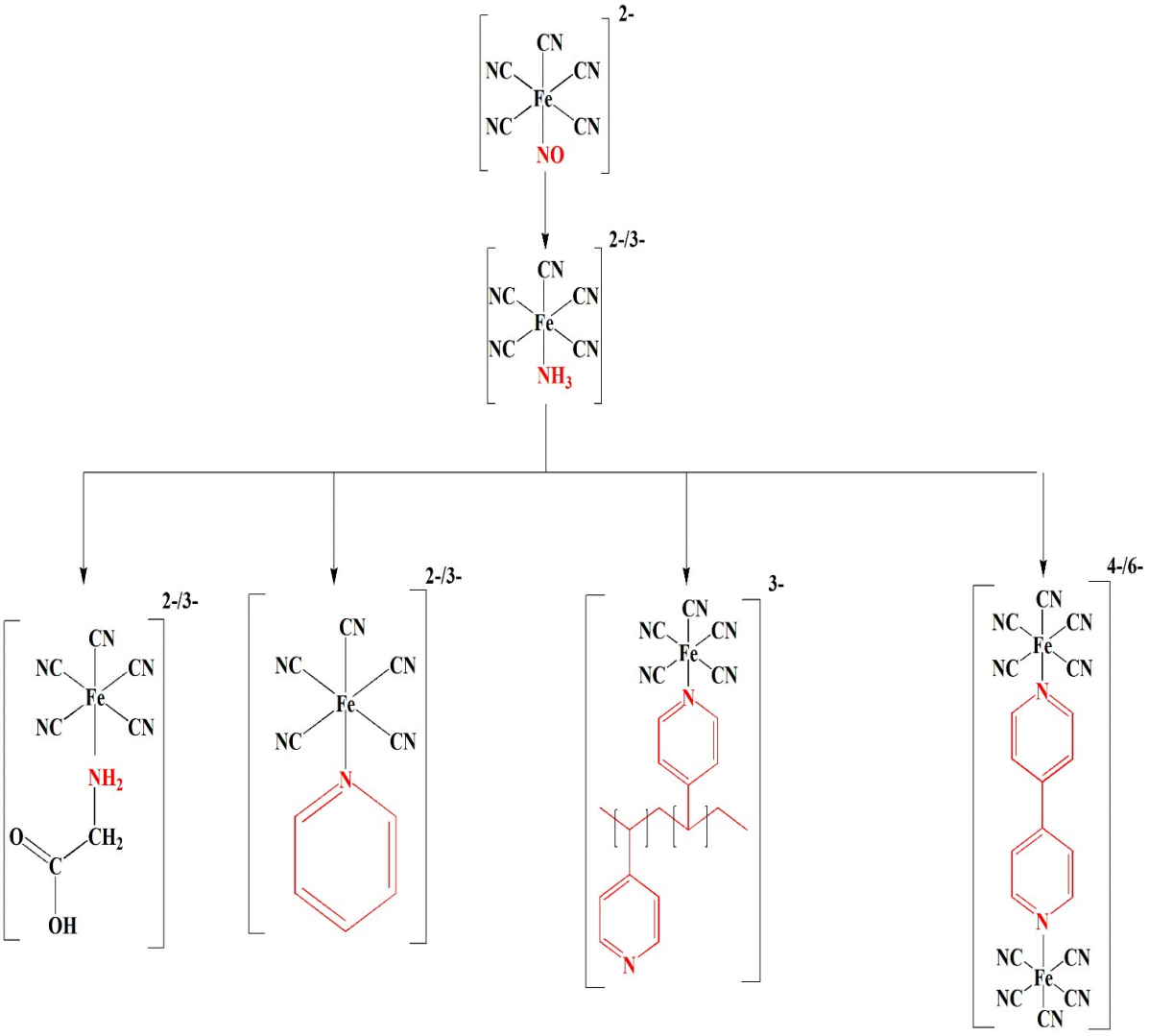

Figure 1. 6. The structure of pentacyanoferrate complexes with different N-bound ligands

Wang et al. has significant studies on the synthesis of Prussian blue analogues with using pentacyanoferrate as a precursor.[42] They showed a novel method for the synthesis of organometallic polymer nanoshells of PB with using Miniemulsion Periphery Polymerization (MEPP). This approach is essentially the first example for the preparation of miniemulsion droplets with using organometallic surfactants and coordination polymerization at pentacyanoferrate periphery of the droplets. The periphery is prepared with organometallic surfactant of poly (ethylene glycol)-b-poly (propylene glycol)-b-poly (ethylene glycol) terminated

with pentacyano (4-(dimethylamino) pyridine) ferrate) as stabilizer with toluene and hexadecane. After addition Fe^{3+} the PB nanoshells with encapsulated oil droplets and block copolymer surfactants were obtained. The MEPP method allows to tune and control size of the PB particles, and brings thermal stability to the particles as well.[43] In the next study of same group, the effect of confining the polymerization on PB nanoshells was investigated while changing the concentrations of both surfactants and they obtained amorphous PB nanocubes.[42] In the following study they prepared polypyrolle/PB core shell nanoparticles and investigated their photoluminescent properties.[44] In the following study by Wang et al. monodispersed soluble PB nanospheres were synthesized by using pentacyanoferrate- coordinated block copolymers of pentacyanoferrate coordinated poly(4-vinylpyridine)-b-poly(dimethylacrylamide). The schematic representation of the synthesis route of PB nanoshells with this method is showed in Figure 1.7. In this study it is stated that three important parameters were reported to have an effect on the structure of monodispersed soluble PB nanospheres; the concentration of water, the amount of $FeCl_3$, and the concentration of the polymer.[45]

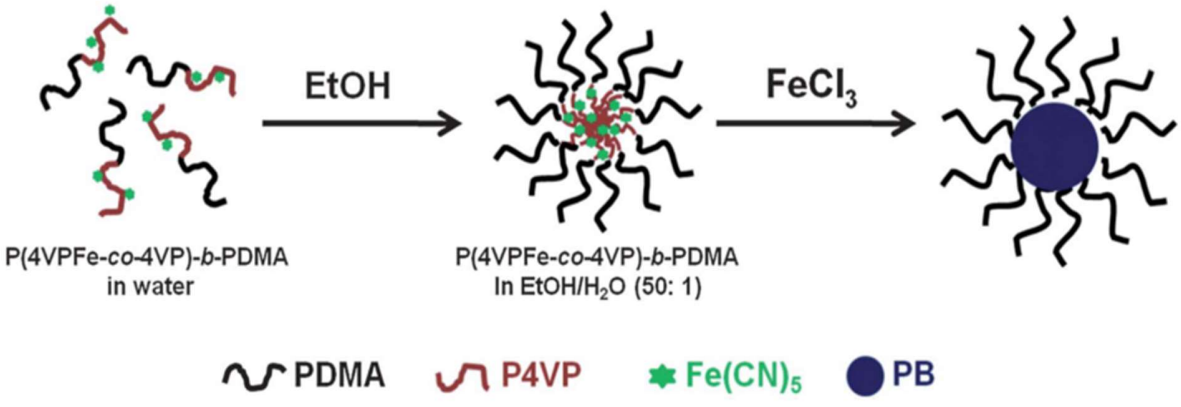

Figure 1. 7. The schematic representation of the synthesis route of monodispersed PB nanoshells[44]

Wang et al. stated that the nature of the ligand in $[Fe(CN)_5L]^{3-}$ structure also has effect on the morphology and structure of the product. In this study, they used CN^-, NH_3, pyrazine, pyridine, and 4-(dimethylamino)-pyridine (DMAP) as a ligand for the synthesis of PB. It is affirmed that N-bound ligands tend to modify the morphology of PB crystalline to amorphous nature in case they bind pentacyanoferrate reactants.[46] Consequently, amorphous metal cyanoferrates coordination networks are expected to have more active metal sites than those available in crystalline hexacyanometalate based coordination networks.

This phenomenon was also observed by our group with the use of a novel pentacyanoferrate-bound polymer (Poly-4-vinyl pyridine (P4VP) as a surfactant and capping ligand (Figure 1.8). With this PB coordination compound coordinated with metallopolymer resulted an amorphous nature of PB with a dramatic reduction in the crystallinities of PBAs compared to MHCMs, and thus, the active metal sites of pentacyanoferrate bound polymer raised 7-fold.[47]

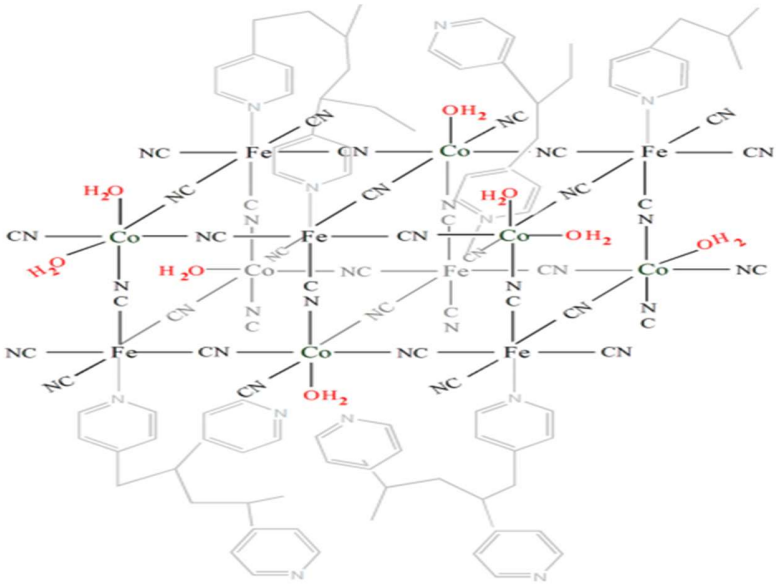

Figure 1. 8. Proposed structure for the cobalt pentacyanoferrate incorporating PVP PB used as electrocatalyst[46]

1-Heptyl 4-(4 pyridyl)pyridinium bromide ($C_{17}H_{23}BrN_2$) is one of the other N-bound ligand that has been used in several applications such as electrochromism and drug delivery.[48], [49]

1.2. CATALYTIC APPLICATIONS

Exponential increase in global energy demand and adverse climatic changes triggered by extensive usage of carbon-based fossil fuels stress the importance of clean and sustainable alternative energy sources.[50]–[52] Hydrogen, with a high energy density, appears to be a promising energy carrier without any harmful by-products.[53], [54] Since solar energy that utilizes the production of H_2 from water has been one of the most promising candidates among sustainable sources of energy, much effort has recently been devoted to investigate efficient methods to split water.[55]–[60]

Half- cell reduction reactions and the potentials for splitting of water are shown in Figure 1.9.

$4H^+ + 4e^- \rightleftharpoons 2H_2$	$E_{cathodic} = 0\ V - 0.059\ V \times (pH)$ vs. NHE
$O_2 + 4H^+ + 4e^- \rightleftharpoons 2H_2O$	$E_{anodic} = 1.23\ V - 0.059\ V \times (pH)$ vs. NHE
$2H_2O \rightarrow 2H_2 + O_2$	$E_{reaction} = -1.23\ V$

Figure 1. 9. Half- cell reactions and the reduction potentials of electrolysis of water

1.2.1. Water Oxidation Catalysis

Since water splitting process is mostly limited by the high overpotential of oxygen evolution reaction (OER), many studies have been performed to introduce novel catalysts that operate at low overpotentials.[61] Many inorganic systems including metal oxides,[62]–[65] perovskites,[66]–

[68] amorphous materials,[69] noble metal based materials,[70], [71] and metal organic frameworks (MOFs)[72], [73] have been investigated as WOCs. Of these, cobalt oxides stand out due to their high catalytic activities.[74], [75] Despite their high catalytic activities, cobalt oxides have mainly two disadvantages;[76], [77]

i) low stability and high tendency to decompose in acidic medium,

ii) difficulty in correlation of the catalytic activities with structure due to their amorphous nature.

Non-oxide materials have also drawn attention as WOCs due to their favorable characteristics such as ease of preparation, stability at a wide range of pH, and robustness during catalytic processes.[78] Patzke et al. reported a carbodiimide-based material that could be used as a WOC, which is stable in acidic and neutral media.[79] A similar class of materials, metal dicyanamides, has also shown to be promising candidates for water oxidation electrocatalysts.[80] Cobalt hexacyanoferrates, members of Prussian blue analogue (PBA) family, are also exceptional candidates for electrocatalytic water oxidation due to their high catalytic activities, robustness, and stability at neutral pH.[81] A further study by Galán-Mascarós et al. showed that PBAs can also be used for light driven water oxidation process in the presence of $[Ru(bpy)_3]^{2+}$ as a chromophore.[82] Despite their high turnover frequencies (TOFs), one of the main drawbacks of cyanide-based systems is their low concentration of electroactive cobalt sites.[81] Their low concentration is attributed to their high crystallinities and relatively larger distances between Co(II) sites (~10 Å) compared to oxide-based systems (~3 Å).[81] This problem has recently been overcome by our group with the use of a novel pentacyanoferrate-bound polymer as a precursor for Co-Fe PBAs, which resulted in a dramatic decrease in the crystallinities of PBAs, and thus, a significant increase in the surface concentration.[47]

Galán-Mascarós et al. approached the same problem by using a new synthetic method for the preparation of thin films of PBAs, which involves chemical etching of cobalt oxides with a hexacyanoferrate solution to form an in-situ PBA film. This novel method led to an impressive improvement on the stability of the electrode and electrocatalytic performance in a wide range of pH. It exhibits a much lower overpotential (510 mV) to obtain a current density of 1 mA cm^{-2}.[83]

Fukuzumi et al. also focused on PBAs for WOC and as cathode for H_2O_2 as fuel applications. In their studies, it is stated that when the number of C-bound metal is less than N-bound ligand, the N-bound ligand should bind to other ligands such as water to complete the octahedral coordination geometry. When this metal is bound to no less than one water molecule, it can then become an active site for water oxidation.[84] In addition, Fukuzumi et al. investigated the photocatalytic water oxidation performances of a series of Co- Pt PBAs in the presence of well-defined $Ru(bpy)_3^{2+/}S_2O_8^{2-}$ couple. The systematic study performed with $[Co(CN)_6]^{3-}$ and $[Pt(CN)_6]^{4-}$ groups in different stoichiometric ratios clearly showed that number of active sites is highly dependent on the defect sizes.[84], [85] Fukuzumi and coworkers also studied the effect of counter cation to the catalytic activity and quantum efficiency displayed by Co-Co PBAs in photocatalytic water oxidation process showing that a quantum efficiency of 200% can be achieved with Co-Co PBAs incorporating calcium ions as counter cations.[86] Previous studies mentioned above clearly show that slight modifications in the structure of PBAs could lead to a significant increase in their catalytic activities.

1.2.2. Water Reduction Catalysis

Production of hydrogen from water has emerged to be a significant challenge due to lack of efficient and cost-friendly water reduction catalysts.[87]–[91] H_2 production with electrochemical and photochemical water reduction has attained considerable attention over past few decades.[92],

[93] Although platinum and iridium based materials were reported to show efficient catalytic activity in reducing water at relatively low overpotentials, being precious metals and low abundance limit their application in bulk H_2 production.[94]–[96] Hence, the essential focus in this field has currently been given to the development of water reduction catalysts incorporating abundantly-available first row transition metal ions.[97]–[100] Much emphasis has been given to cobalt containing compounds as catalysts for hydrogen evolution reaction (HER) over the past decade for their versatile redox chemistry, ease in preparation, and robustness.[101]–[105] The investigation of a molecular pentapyridyl cobalt complex as a HER catalyst in water buffered at pH 7 exhibits an onset overpotential of 660 mV at Faradaic efficiency close to 100% with carbon-free by-products.[106] Artero et al. reported the investigation of cobalt-based catalytic material (H_2-Cocat) for electrocatalytic reduction of water at pH 7, exhibiting catalytic onset overpotential of 50 mV with 100% Faradaic efficiency (Figure 1.10).[107]

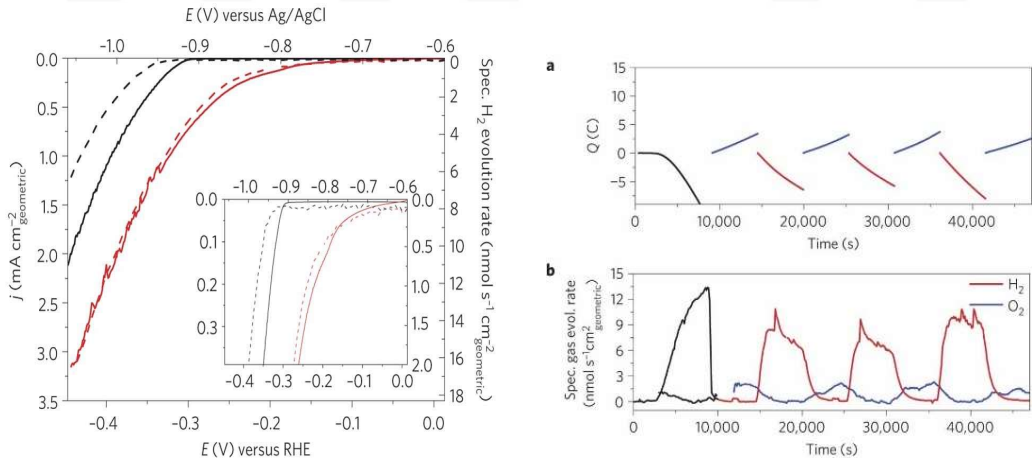

Figure 1. 10. A Janus cobalt-based electrocatalytic material for hydrogen evolution [106]

A similar study was reported involving the study of electrodeposited cobalt-sulfide catalyst for electrochemical and photochemical H_2 generation from water by Chang et al. The study reports a low catalytic onset overpotential of only 43 mV and near 100% Faradaic efficiency in phosphate

buffer at pH 7.[108] Moreover, Castellano et al. performed a comprehensive investigation of visible-light photo-generation of H_2 from water using cobalt(II) polypyridyl complexes as catalysts, $[Ru(bpy)_3]^{2+}$ as a photosensitizer (PS), and ascorbic acid/ascorbate as an electron source, achieving a turnover number (TON) of 4200 (H_2/Co) and a turnover frequency (TOF) of 3200 (H_2/Co per h) under simulated sunlight at pH 4.[109]

Prussian blue analogues have recently been investigated to address critical steps of hydrogen economy including H_2 storage and water oxidation.[110], [111] The relatively high stability of this family of coordination compounds over a wide range of pH and easy synthesis together with their porous nature and the availability of electroactive metal sites make them promising candidates for various applications ranging from selective gas adsorption to catalysis. Several studies focusing on the water-oxidation performance of PBAs clearly show that cobalt sites on the surface could be used for water oxidation process and that cyanide based coordination compounds can retain their three-dimensional structure even under harsh catalytic conditions. [85]

A Prussian blue analogue, $K_4Fe_4[Fe(CN)_6]_3$, has also been investigated as a water reduction catalyst in 1997 with a low catalytic activity,[112] and hence no in-detailed studies have been carried-out further on other PBAs.

1.3. OBJECTIVE OF THE THESIS

Previous studies mentioned above clearly show that slight modifications in the morphology and the composition of PBAs could lead to a significant increase in their catalytic activities. (Figure 1.11)

Although previous studies took advantage of rich and well-established cyanide chemistry no systematic study has been performed to investigate the effect of hexacyanometal unit to the electronic properties and catalytic performance of electroactive cobalt sites. In this thesis,

electrocatalytic measurements on a series of cobalt hexacyanometalates (CHCMs) incorporating different $M(CN)_6$ units (M = Co^{III}, Cr^{III}, and $Fe^{II/III}$) together with characterization studies were performed to investigate the effect of the type and oxidation state of the metal in $M(CN)_6$ unit to the catalytic activity of PBAs.

Second, the effect of the change in the morphology by using an N-donor ligand (HPPB) to synthesize pentacyanoferrate coordinated PB on the water oxidation ability was investigated. Synthesis, characterization, and electrochemical experiments were performed to observe the improvements on catalytic activity for PB.

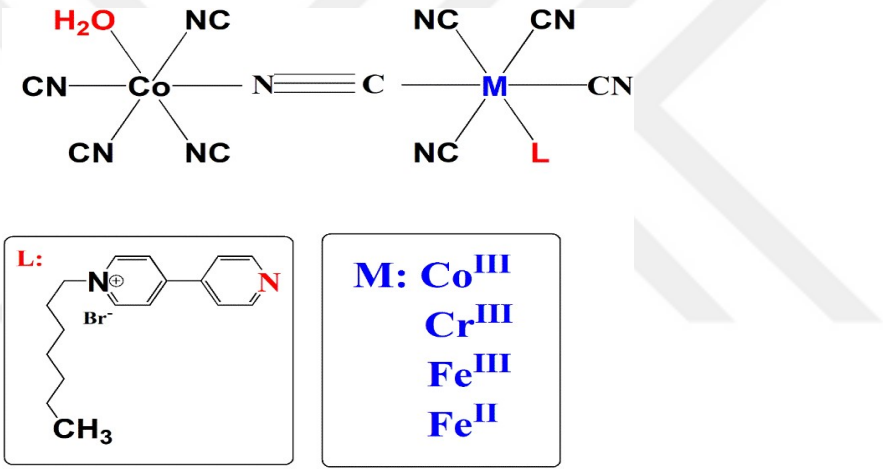

Figure 1. 11. Schematic representation of changing groups in PB structure

Third, given the promising catalytic activities of several cobalt-based systems and the robustness of Prussian blue analogues in harsh catalytic processes including water oxidation, a Co-Co Prussian blue analogue was investigated as a hydrogen evolution electrocatalyst for the first time. Taking into consideration the efficiency of cobalt-based water reduction catalysts, and no apparent investigations reporting the application of PBA derivatives in water reduction, the thesis aims to re-evaluate the application of a Prussian blue analogue, cobalt hexacyanocobaltate, as a HER catalyst.

CHAPTER 2

EXPERIMENTAL AND INSTRUMENTATION

2.1. EXPERIMENTAL

2.1.1. Synthesis of Cobalt Hexacyanometalates as Water Oxidation Catalysts

2.1.1.1 Chemicals and Solutions

Potassium hexacyanocobaltate $K_3[Co(CN)_6]$ (Sigma-Aldrich, >97.0%), cobalt chloride hexahydrate $CoCl_2.\ 6H_2O$ (Sigma-Aldrich, 98.0%), Potassium hexacyanochromate $K_3[Cr(CN)_6]$ (Aldrich, 99.99%), Potassium hexacyanoferrate $K_3[Fe(CN)_6]$ (Sigma-Aldrich, >97.0%), potassium hexacyanoferrate trihydrate, $K_3[Fe(CN)_6].3H_2O$ (Sigma-Aldrich, 98.5-102%). All the solutions were prepared with Millipore Milli-Q deioniz47ed water with a resistivity of 18.2 mΩ.cm.

2.1.1.2. Synthesis of the Bulk Catalysts

$K_aCo_b[M(CN)_6]\cdot xH_2O$ ($M = Fe^{II}$, Fe^{III}, Co^{III}, and Cr^{III}) abbreviated throughout as [Co^{II}-Fe^{II}], [Co^{II}-Fe^{III}], [Co^{II}-Co^{III}], and [Co^{II}-Cr^{III}]. In the case of [Co^{II}-Co^{III}] an aqueous solution of $CoCl_2.6H_2O$ (0.15 M, 20 mL) was added dropwise to an aqueous solution of $K_3[Co(CN)_6]$ (0.10 M, 20 mL) at room temperature.[47] The mixture was kept under stirring for 1 hour and then allowed to wait overnight for precipitation. The solution was filtered by vacuum suction and washed with copious amounts of water to obtain the pink powder. The powder was dried further in desiccator. The same procedure was applied for [Co^{II}-Fe^{II}] (dark blue), [Co^{II}-Fe^{III}] (dark brown), and [Co^{II}-Cr^{III}] (pale yellow).

2.1.1.3. Preparation PBA modified FTO Electrodes

FTO electrodes were procured from Sigma-Aldrich (with ~80% transmittance, 2 mm with a

surface resistance of 7 Ω. sq^{-1}, 1x2 cm). Electrodes were washed by sonication for 10 minutes in basic soapy solution, deionized water and isopropanol respectively. Then they were annealed at 400 °C for 30 minutes. Catalyst modified electrodes were prepared by drop casting method. A mixture of 5 mg of PBA catalyst, 500 µL DMF, 500 µL water and 100 µL Nafion solution were mixed and sonicated for 30 minutes. After making a stable suspension, 50 µL of it was taken and dropped onto by covering 1 cm^2 of the FTO electrode. Electrodes were then dried at room temperature for 10 minutes followed by 80 °C for 10 minutes in an oven. Then they were left in desiccator until further use for electrochemical experiments and characterization.

2.1.2. Synthesis of Cobalt HPPB Coordinated Pentacyano Ferrate Prussian Blue Analogue as Water Oxidation Catalyst

2.1.2.1. Synthesis of $Na_3[Fe^{II}(CN)_5NH_3].3H_2O$

This chemical will be abbreviated as [$Fe(CN_5)$-NH_3] throughout the chapters. It was synthesized according to previously reported methods.[113] 15 g of $Na_2[Fe^{III}(CN)_5NO].2H_2O$ was dissolved in 60 ml of water. 3 g of NaOH was added to solution at relatively low temperature (10°C) under constant stirring. 25% NH_4OH solution was added until observing saturation after cold methanol was added. Finally, bright yellow precipitation was obtained and aged overnight at 0° C. The product was recrystallized with using NH_4OH and CH_3OH solution. The recrystallization part repeated two times. It was putted in desiccator for further usage.

2.1.2.2. Synthesis of 1-Heptyl 4-(4 pyridyl) Pyridinium Bromide (HPPB) Coordinated Pentacyanoferrate $[Fe(CN)_5NH_3]^{3-}$

0.18 mmol (603 mg) of 1-Heptyl 4-(4 pyridyl) Pyridinium Bromide ($C_{17}H_{23}BrN_2$) was dissolved in 60 ml methanol. This compound will be abbreviated as HPPB throughout manuscript. 0.18

mmol (588 mg) of $[Fe(CN)_5NH_3]^{3-}$ was dissolved in approximately 180 ml methanol since it is partially dissolved in methanol. $[Fe(CN)_5NH_3]^{3-}$ solution was added into HPPB solution dropwisely. The color of the solution turned immediately from transparent into dark blue. The solution was mixed for two days. This product will be abbreviated throughout as $[Fe(CN)_5$-HPPB$]^{2-}$.

2.1.2.3. Synthesis of Cobalt 1-Heptyl 4-(4 pyridyl) Pyridinium Bromide Coordinated Pentacyanoferrate (Co[Fe(CN)$_5$- HPPB])

The compound will be abbreviated as Co[Fe(CN)$_5$-HPPB] throughout the thesis. The powder product was prepared by drop by drop method. 0.18 mmol (225 mg) of $Co(NO_3)_2.6H_2O$ was dissolved in water then added drop by drop into $[Fe(CN)_5$-HPPB$]^{2-}$ solution. The color of the solution changed from dark blue to dark purple. After 2 hours of constant mixing the solution of Co[Fe(CN)$_5$- HPPB] were collected by centrifugation at 6000 rpm for 15 minutes. The powder was purified with ethanol and water and this process repeated 3 times. The product was put in desiccator for further use.

2.1.2.4. Co[Fe(CN)$_5$- HPPB] Modified FTO Electrodes

FTOs were prepared by two steps with in situ method. Firstly, FTOs were spin coated with 0.01 M 50 μl of $[Fe(CN)_5$- HPPB$]^{2-}$ solution at 1000 rpm for 30 seconds and blue translucent layer was observed. Secondly, the FTO was dipped into 0.02 M $Co(NO_3)_2.6H_2O$ for 15 minutes. Dark purple color was observed. This procedure was repeated for 3 times. The electrodes were kept at desiccator and these electrodes were rinsed with deionized water before using.

2.1.3. Synthesis of Prussian Blue Analogues as Hydrogen Evolution Catalysts

2.1.3.1. Synthesis of Catalysts

All the solutions were prepared with Millipore Milli-Q deionized water with a resistivity of 18.2 mΩ.cm. 0.2 M 25 ml solutions of $Co(NO_3)_2.6H_2O$ and $K_3Co(CN)_6$ were prepared separately at room temperature. Co(II) solution was added dropwisely to $[Co(CN)_6]^{3-}$ solution. The reaction mixture was left under stirring for 1 hour and then aged overnight. The precipitate was filtrated under suction and stored in a desiccator. The resulting powder was pink in color. Same procedure was applied to Zn-Co PBA. The starting materials were the solutions of 0.2 M $Zn(NO_3)_2 \cdot 6H_2O$ and $K_3Co(CN)_6$. The color of powder Zn-Co PB is white.

2.1.3.2 Catalyst modified FTO electrodes

A two-step in-situ method was used to prepare the electrodes, which includes spin coating the hexacyanocobaltate precursor onto the FTO surface followed by dipping it in a cobalt, or zinc solution. Solutions of 0.2 M $Co(NO_3)_2 \cdot 6H_2O$ and 0.2 M $K_3[Co(CN)_6]$ were prepared with Millipore water. $K_3[Co(CN)_6]$ solution was spin-coated onto FTO electrodes at 1500 rpm for 3 min, after that, the electrodes were immersed in a solution of $Co(NO_3)_2.6H_2O$ for 5 min. This process was repeated three times. The electrodes were kept in a vacuum desiccator until further use. The electrodes were rinsed with deionized water prior to use. Similar coatings were made onto FTO electrodes (at 1500 rpm for 3 min) using solutions of 0.2 M Zn $(NO_3)_2 \cdot 6H_2O$, 0.2 M $K_3[Co(CN)_6]$, and 0.2 M $Co(NO_3)_2 \cdot 6H_2O$.

2.2. INSTRUMENTATION

2.2.1. Fourier Transform Infrared Spectroscopy (FTIR)

Fourier transform infrared spectra (FTIR) were recorded by Bruker Alpha Platinum-ATR

Spectrometer model. The spectra were recorded in transmission mode by 64 scans in wavenumber range of 400- 4000 cm^{-1}.

2.2.2. Powder X-Ray Diffraction (PXRD)

XRD patterns were measured by using a Pananalytical X'PertPro Multipurpose X-Ray Diffractometer (MPD) with CuK_α X- Ray Radiation (λ= 1.5418 Å). The diffraction patterns were recorded in the 2θ diffraction angle with a range of 10-70°, step size of 0.05.

2.2.3. Grazing Incidence X-Ray Diffraction (GI-XRD)

GI-XRD patterns were recorded by using a Panalytical X'Pert3 MRD Material Research Diffractometer (MRD) with CuK_α X-ray radiation (λ=1.5418^o) at an incident (w) angle of 0.58^o.

2.2.4. Scanning Electron Microscopy (SEM) and Energy Disperse X-Ray Analysis (EDAX)

FEI-Quanta 200 FEG ESEM was used for imaging and EDAX analysis, at 5 kV beam voltage for imaging and 30 kV for EDAX.

2.2.5 X-Ray Photoelectron Spectroscopy

XPS analysis was performed using Thermo Scientific K-Alpha X-Ray Photoelectron Spectrometer system with a AlK_α microfocused monochromator source operating at 400 mm spot size and $h\gamma$= 14.866 eV accompanied by a flood gun for charge neutralization, 200 eV for survey scan and 30 eV for individual scans.

2.2.6. Electrochemical Measurements

Gamry Instruments Interface 1000 Potentiostat/Galvanostat was used for performing electrochemical measurements. A conventional three electrode cell was used with Ag/AgCl (3.5 M KCl) as reference electrode, FTO as the working electrode, and Pt wire as counter electrode.

YSI 5100 dissolved oxygen sensing electrode instrument equipped with a dissolved oxygen field probe was used to determine the oxygen evolution. Mettler Toledo S220 SevenCompact™ pH/Ion pH meter was used to determine the pHs of buffer solutions. KPi buffer solution was prepared by using KH_2PO_4 and K_2HPO_4 and pH of the solution was adjusted by adding H_3PO_4 or KOH. Bulk water electrolysis was performed with a two compartments cell with separation of a glass frit. The electrolysis and steady state chronoamperometry experiments were performed in KPi buffer solution containing 1 M KNO_3 as supporting electrolyte. All of the electrochemical experiments were performed at room temperature and under inert conditions (N_2 atmosphere). Prior to the studies, the electrodes were dipped into the buffer solution and the solution was purged with N_2 gas for 15 min to remove dissolved O_2. All potentials were measured versus Ag/AgCl reference electrode and were reported versus the normal hydrogen electrode (NHE) using the equation of E(NHE) = E(Ag/AgCl) + 0.205 V

2.2.7. Data Analysis

OriginPro 8.5 was used in order to plot and analyze the results.

CHAPTER 3

RESULTS AND DISCUSSION FOR METAL HEXACYANOMETALATES (MHCMs) as WATER OXIDATION CATALYSTS

3.1. CHARACTERIZATIONS OF METAL HEXACYANOMETALATES

A series of metal hexacyanometales with molecular formulas $K_xCo_y[M(CN)_6]_2$ M: Co^{III}, Cr^{III}, Fe^{III}, Fe^{II} have been studied as water oxidation catalysts. Characterization studies of the bulk catalysts have been performed by X-ray Diffraction, Fourier Transform Infrared Spectroscopy, and Electron Dispersive X-ray spectroscopy techniques.

3.1.1. Powder X-Ray Diffraction Studies

All samples are isostructural with Prussian blue crystal structure adopting face centered cubic structure (fcc) with Fm3m space group as confirmed by powder XRD studies (JCPDS Card No: 73-0687). The characteristic 2theta (2θ) peaks for Prussian blue structure have been observed for all of the materials (Figure 3.1.) and lattice parameter was determined to be around 10 Å for each derivative (Table 3.1).

Table 3. 1. Calculated lattice parameters and 2 theta (2θ) values of [200] plane of MHCM derivatives

	2theta (2θ)	**Lattice Parameter (Å)**
[Co^{II}- Co^{III}]	17.221	10.11
[Co^{II}- Cr^{III}]	16.959	10.30
[Co^{II}- Fe^{III}]	17.190	10.16
[Co^{II}- Fe^{II}]	17.379	10.02

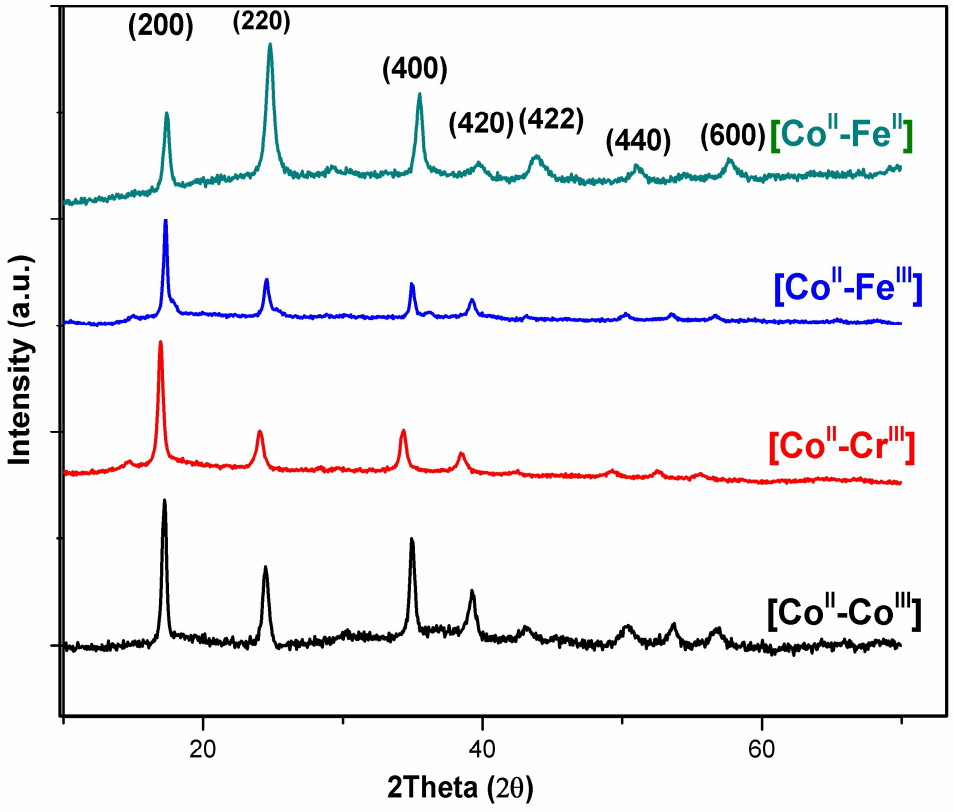

Figure 3. 1. Powder XRD patterns of PBAs

3.1.2. Infrared Studies

Infrared studies show that PBAs exhibit the following characteristic bands that are observed for Prussian blue type systems;

a) a sharp band at around 1610 cm^{-1} and a broad one at 3200–3500 cm^{-1}, which represent H-OH bending and OH stretch, respectively,

b) a sharp peak at around 490–590 cm^{-1} due to M-CN-M' bending stretch, and

c) a sharp stretch at around 2120–2180 cm^{-1} that is attributed to CN stretch (Table 3.2).

Table 3. 2. FTIR analysis of PB derivatives

	ν(CN) **cm^{-1}**	**δ(H_2O)** **cm^{-1}**	**ν(OH)** **cm^{-1}**	**ν (M-CN-M')** **cm^{-1}**
[Co^{II}- Co^{III}]	2176	1609	3200-3500	491
[Co^{II}- Cr^{III}]	2173	1611	3200-3500	491
[Co^{II}- Fe^{III}]	2120	1621	3200-3500	430
[Co^{II}- Fe^{II}]	2069	1607	3200-3500	454

PBAs exhibit higher CN stretching frequencies compared to their hexacyanometal precursors, which confirm the binding of nitrogen atoms of cyanide to Co(II) sites [6], [7] (Figure 3.2).

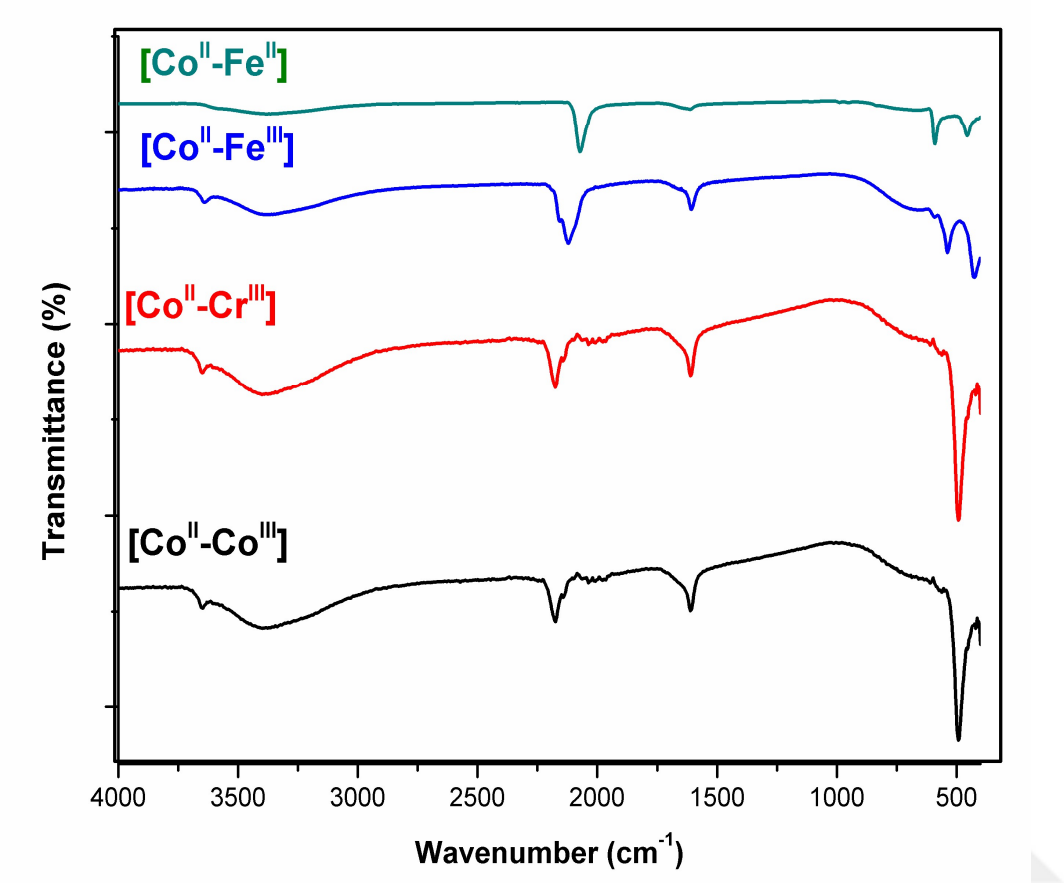

Figure 3. 2. FTIR Spectra of PB derivatives

3.1.3. Energy Dispersed X- Ray Analysis of Metal Hexacyanometalates

The atomic ratio of metals in each compound was extracted by EDX analysis (Table 3.3). The following molecular formulae were obtained based on stoichiometric ratio of metals: $K_{0.76}Co_{2.62}[Co(CN)_6]_2$, $K_{0.82}Co_{2.59}[Cr^{III}(CN)_6]_2$, $K_{0.62}Co_{2.69}[Fe^{III}(CN)_6]_2$, and $K_{0.7}Co_{1.65}[Fe^{II}(CN)_6]_2$ for [Co^{II}-Co^{III}], [Co^{II}-Cr^{III}], [Co^{II}-Fe^{III}], and [Co^{II}-Fe^{II}], respectively.

Table 3. 3. Atomic ratios of Co:M:K for PB derivatives.

	Co:M:K atomic ratio			**$K_aCo_b[M(CN)_6]$**
Compound (Co-M)	Co	M	K	
[Co^{II}- Co^{III}]	8.26		1.36	$K_{0.76}Co_{2.62}[Co(CN)_6]_2$
[Co^{II}- Cr^{III}]	4.03	3.20	1.26	$K_{0.82}Co_{2.59}[Cr(CN)_6]_2$
[Co^{II}- Fe^{III}]	6.24	4.41	1.45	$K_{0.62}Co_{2.69}[Fe^{III}(CN)_6]_2$
[Co^{II}- Fe^{II}]	2.7	2	1.4	$K_{0.7}Co_{1.35}[Fe^{III}(CN)_6]$

Each compound has similar potassium content in the 0.6-0.8 range, which results in an average of ~4.5 CN groups per Co(II) sites. The remaining coordination sphere of Co(II) sites are occupied by water molecules, which play active role in water oxidation (Figure 3.3).

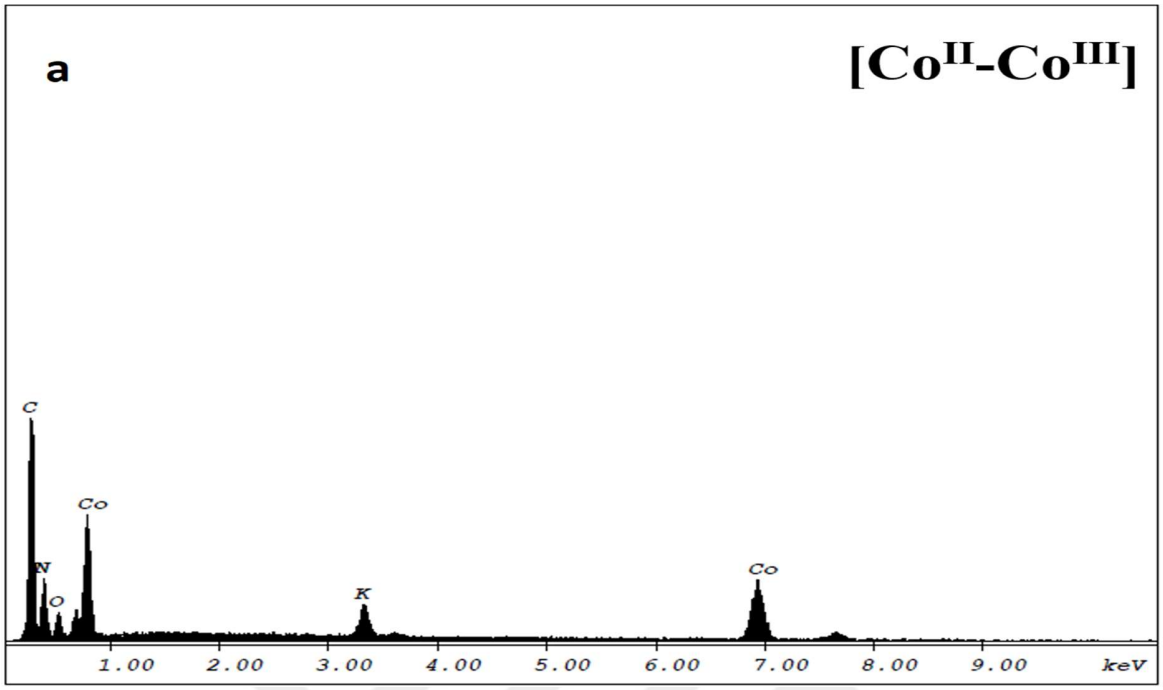
a
[Co^II-Co^III]
C
Co
N
O
K
Co
1.00
2.00
3.00
4.00
5.00
6.00
7.00
8.00
9.00
keV

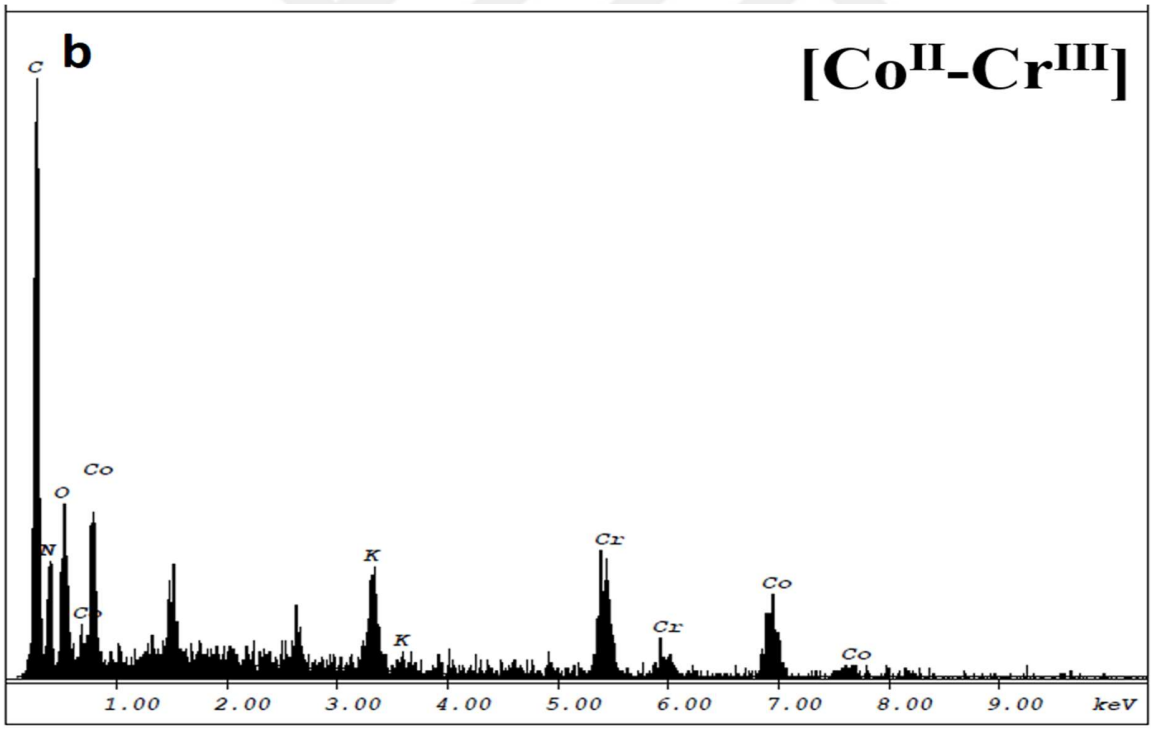
b
[Co^II-Cr^III]
C
Co
O
N
Co
K
K
Cr
Cr
Co
Co
1.00
2.00
3.00
4.00
5.00
6.00
7.00
8.00
9.00
keV

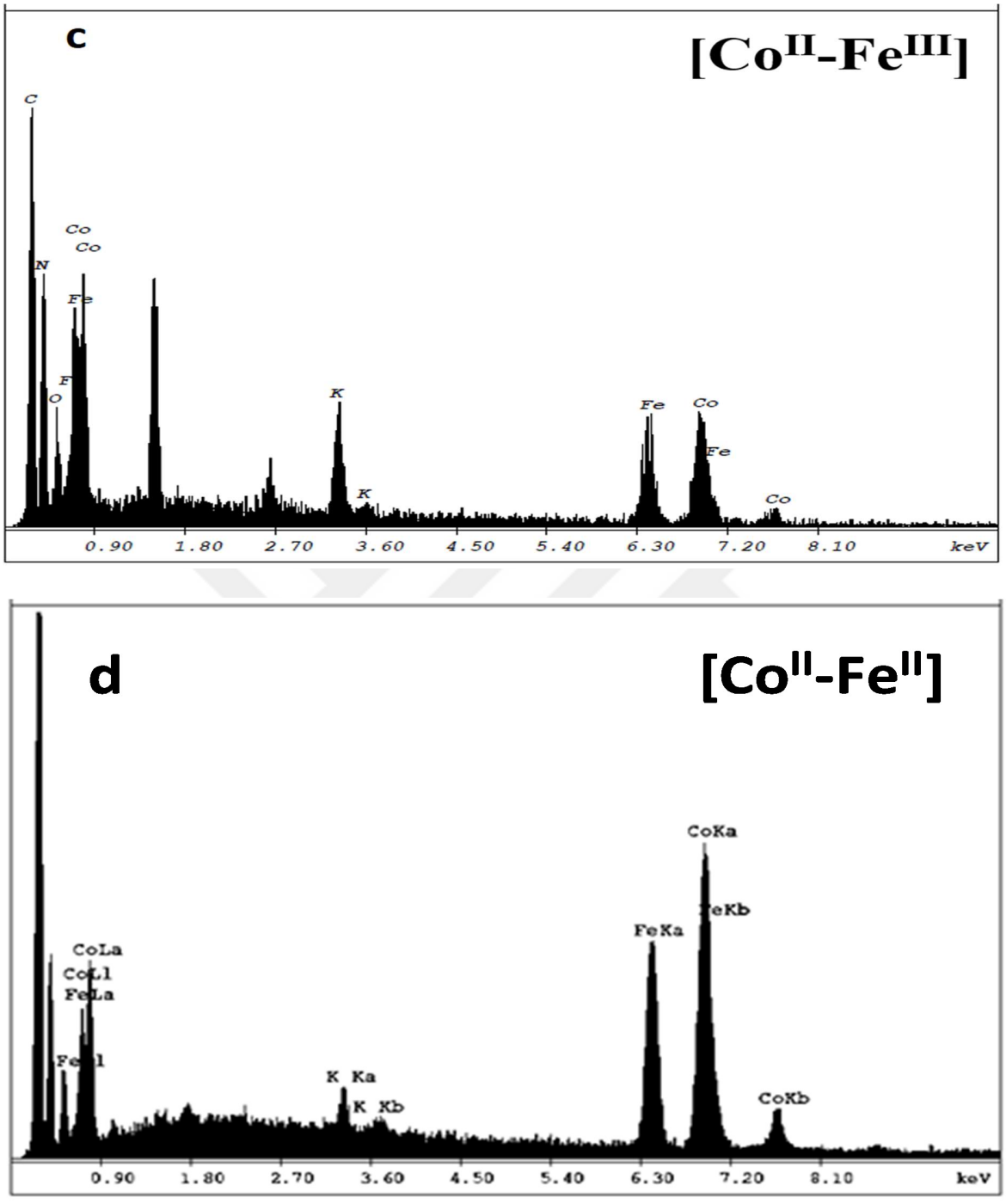

Figure 3. 3. EDX analysis of PB derivatives of a) [Co^{II}-Co^{III}], b) [Co^{II}-Cr^{III}], c) [Co^{II}-Fe^{III}], and d) [Co^{II}-Fe^{II}].

3.2. ELECTROCHEMICAL WATER OXIDATION STUDIES OF METAL HEXACYANOMETALATES

3.2.1. Cyclic Voltammetry Studies

All the electrochemical experiments were conducted with a Prussian blue analogue (PBA) modified fluorine-doped tin oxide (FTO) electrode. Cyclic Voltammograms (CVs) of $Co[M(CN)_6]$ (M: Co^{III}, Cr^{III}, and $Fe^{II/III}$) were taken in 50 mM phosphate buffer with 1 M KNO_3 as the electrolyte at pH 7 in a 0.2–1.7 V vs. NHE potential range. The sweep rate of all the voltammograms is 50 mv sec^{-1} (Figure 3.4). [Co^{II}-Co^{III}] exhibits a quasi-reversible redox couple with an oxidation peak at 1.210 V and a reduction one at 1.031 V vs. NHE that can be assigned to $Co^{2+/}Co^{3+}$ redox couple. A similar redox couple was observed also for other PBAs. Another peak, at a relatively higher potential, is observed at around 1.615 V vs. NHE for [Co^{II}-Co^{III}], which can be assigned to Co^{3+}/Co^{4+} redox process.[114]

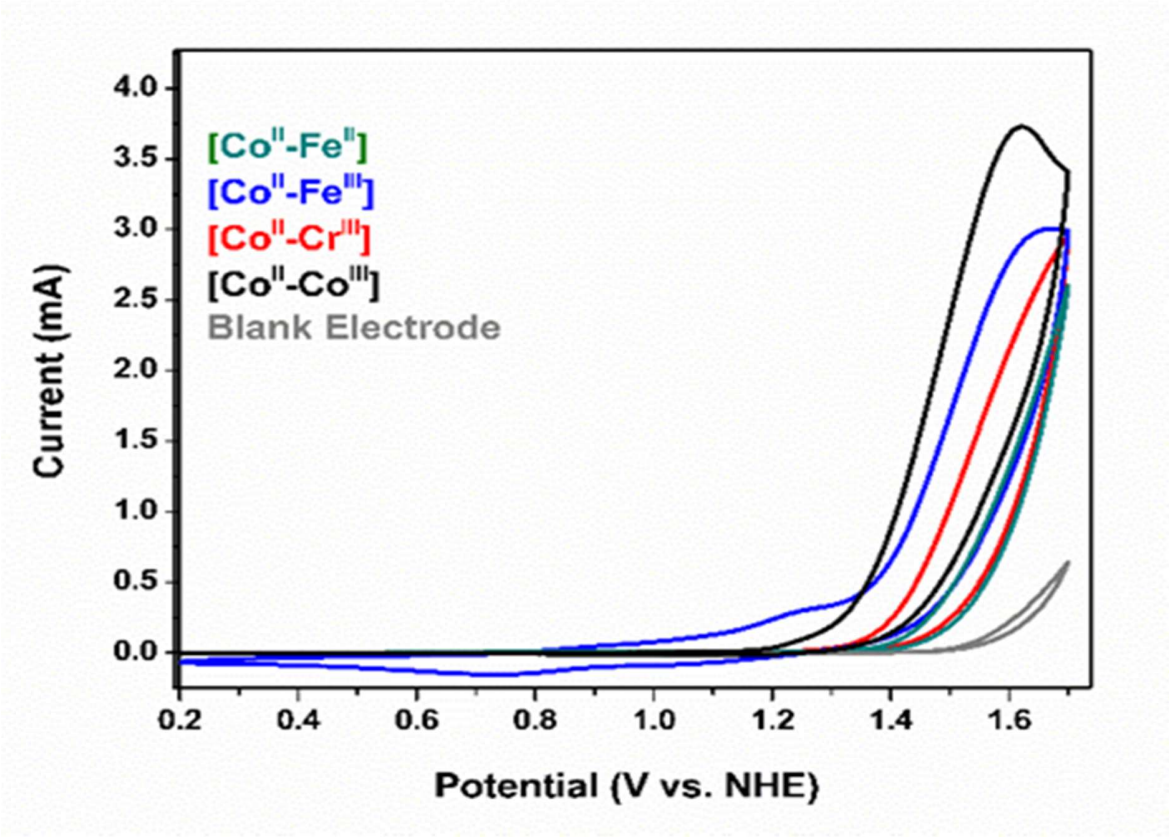

Figure 3. 4. Cyclic Voltammograms of PB derivatives ([Co^{II}-Co^{III}] black, [Co^{II}-Cr^{III}] red, [Co^{II}-Fe^{III}] blue, and [Co^{II}-Fe^{II}] green lines). The gray line indicates the electrochemical response of blank electrode.

Surface coverage of the electroactive Co^{2+} species on FTO electrode i.e., surface concentration, was determined by performing CVs at different scan rates (25–225 mV.sec^{-1} range) recorded in 50 mM KPi buffer 1 M KNO3 at pH 7 in the 0.8–1.6 V vs. NHE range. The surface concentration of electroactive cobalt sites is calculated by using the slope of the linear fit of current vs. scan rate graph, according to equation 3.1 below,

$$\boldsymbol{Slope} = \frac{n^2F^2A\Gamma}{4RT} \qquad \text{(Equation 3.1)}$$

In this equation n is equal to 1 since it is a one electron redox process. Faraday's constant (96485 $C.mol^{-1}$) is represented as F. A is area, Γ is the surface coverage in the unit of $mol.cm^{-2}$. R stands for ideal gas constant, and T is temperature.

Surface concentration of derivatives were obtained in the 2–5 nmol cm^{-2} range, which is in good agreement with the previously reported studies[47], [81] (Figure 3.5).

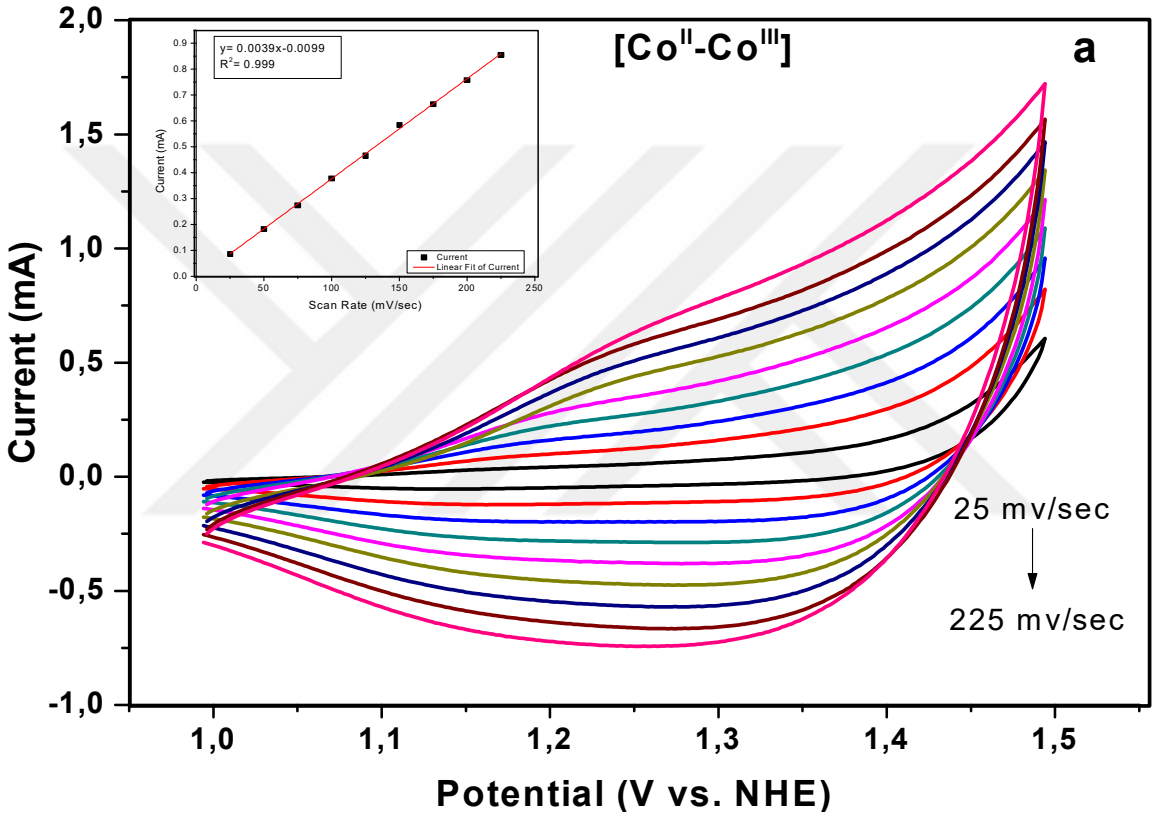

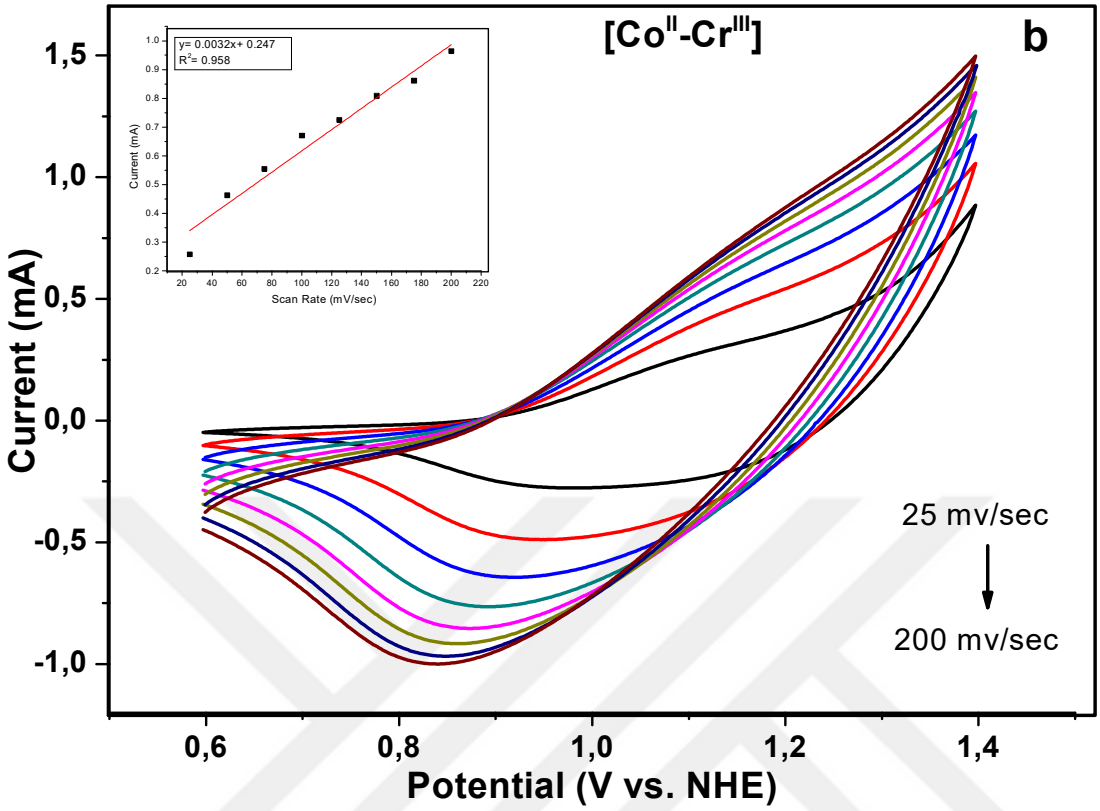
[Co^{II}-Cr^{III}]
b
y= 0.0032x+ 0.247
R^2= 0.958
Current (mA)
Scan Rate (mV/sec)
25 mv/sec
200 mv/sec
Current (mA)
Potential (V vs. NHE)

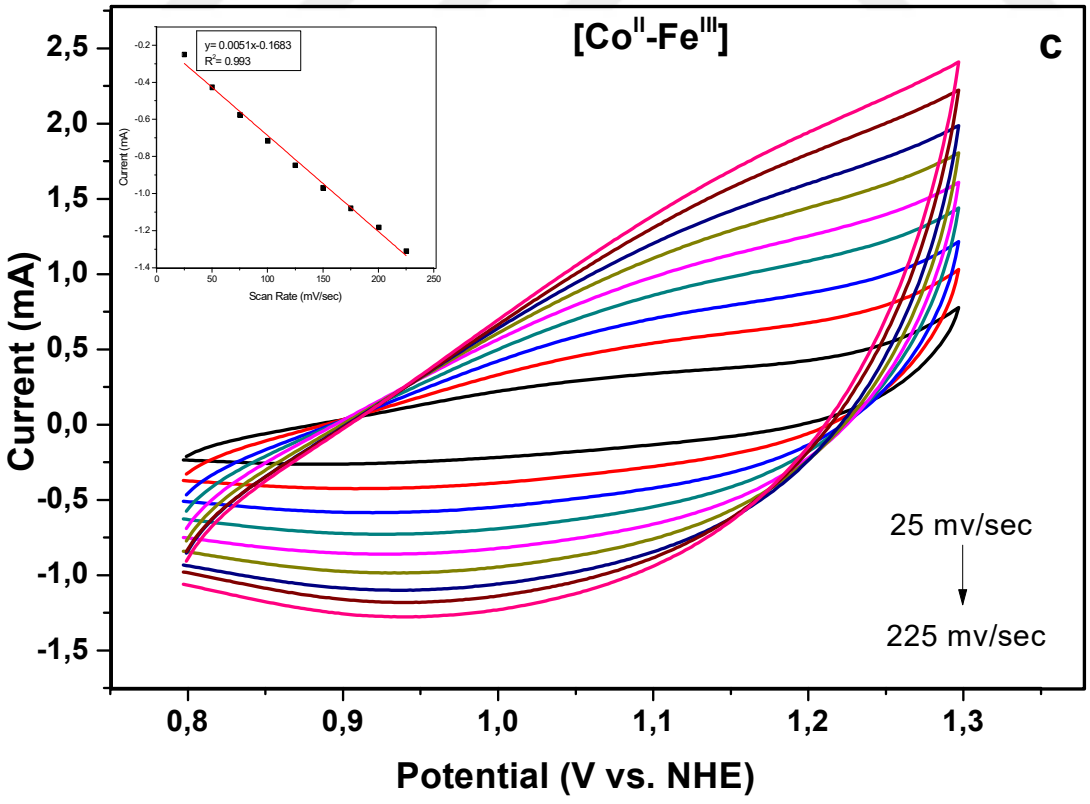
[Co^{II}-Fe^{III}]
c
y= 0.0051x-0.1683
R^2= 0.993
Current (mA)
Scan Rate (mV/sec)
25 mv/sec
225 mv/sec
Current (mA)
Potential (V vs. NHE)

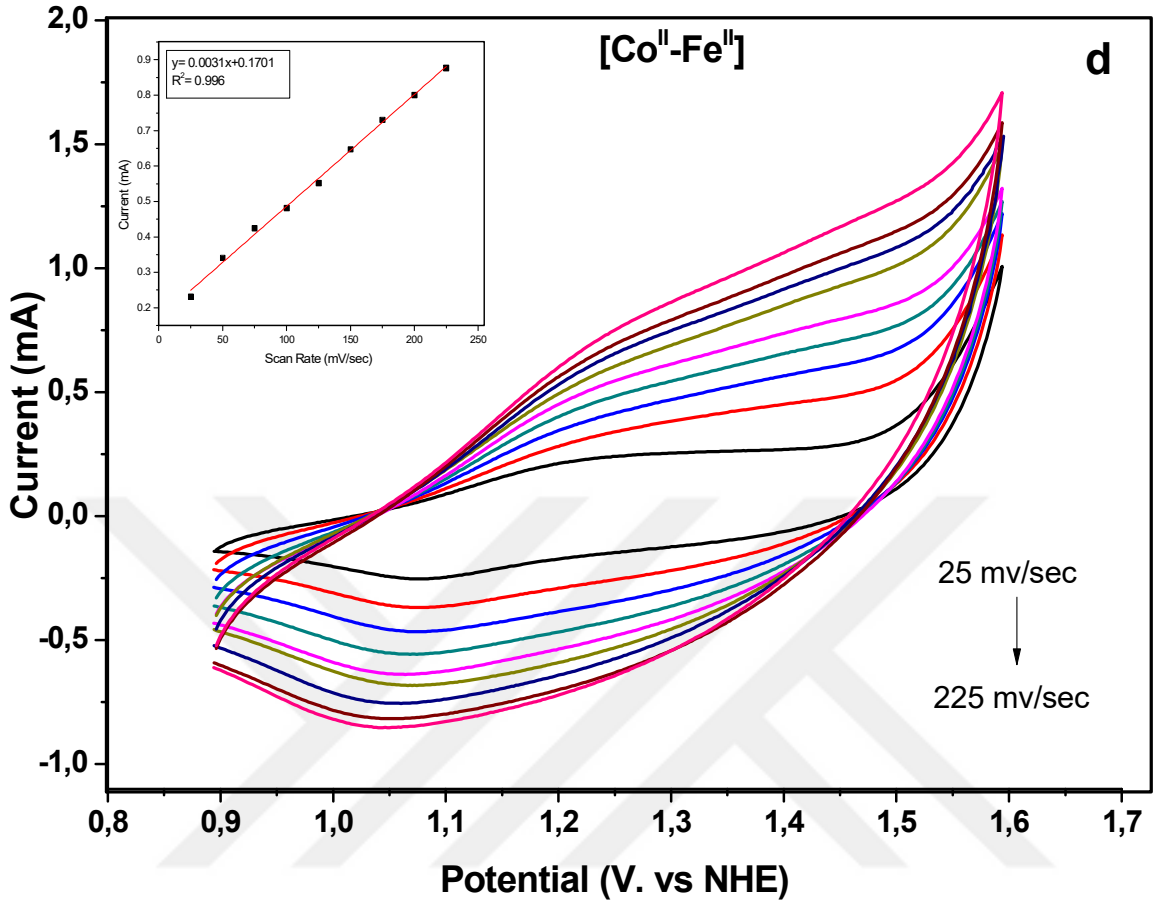

Figure 3. 5. Cyclic Voltammograms of PB derivatives of a) [Co^{II}-Co^{III}], b) [Co^{II}-Cr^{III}], c) [Co^{II}-Fe^{III}], and d) [Co^{II}-Fe^{II}] performed at different sweep rates. Insets show the linear relationship between peak current of Co^{2+}/Co^{3+} redox couple and sweep rates.

3.2.2. Tafel Slope and Turnover Frequency Analyses

Tafel plots of each catalyst was obtained by performing chronoamperometry measurements at different applied potentials recorded in a 50 mM KPi buffer at Ph 7.0 to further investigate their electrocatalytic performances. A linear trend was achieved between the logarithm of the steady state current densities and in an overpotential range of 283–483 mV with Tafel slopes in 90–130 mV dec^{-1} range (Figure 3.6).

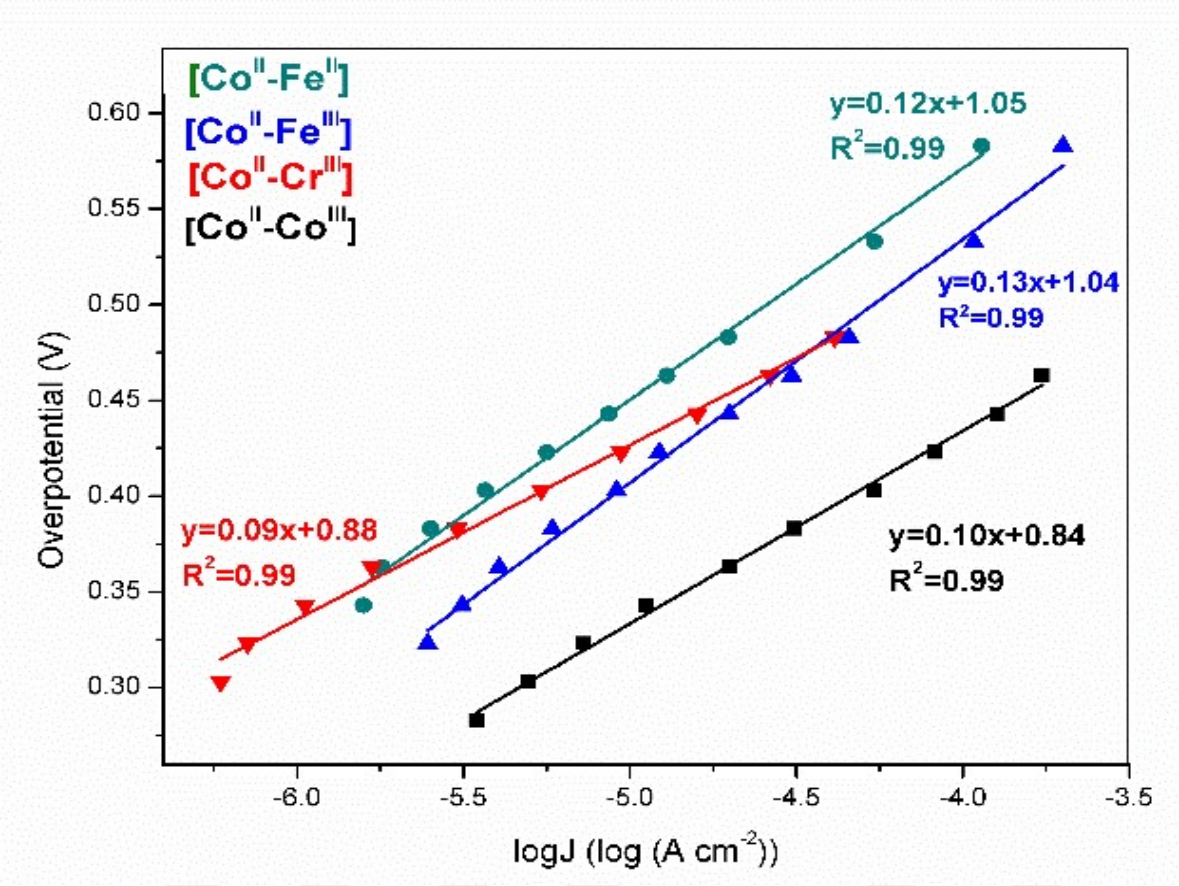

Figure 3. 6. Tafel plots for PB derivatives from 1.1 to 1.4 V vs NHE

Similarity in the Tafel slopes indicates similar OER mechanisms. According to chronoamperometric measurements onset overpotentials of 283, 303, 323, and 343 mVs are obtained, respectively, for [Co^{II}-Co^{III}], [Co^{II}-Cr^{III}], [Co^{II}-Fe^{III}], and [Co^{II}-Fe^{II}], which are in line with cyclic voltammetry studies (Figure 3.7).

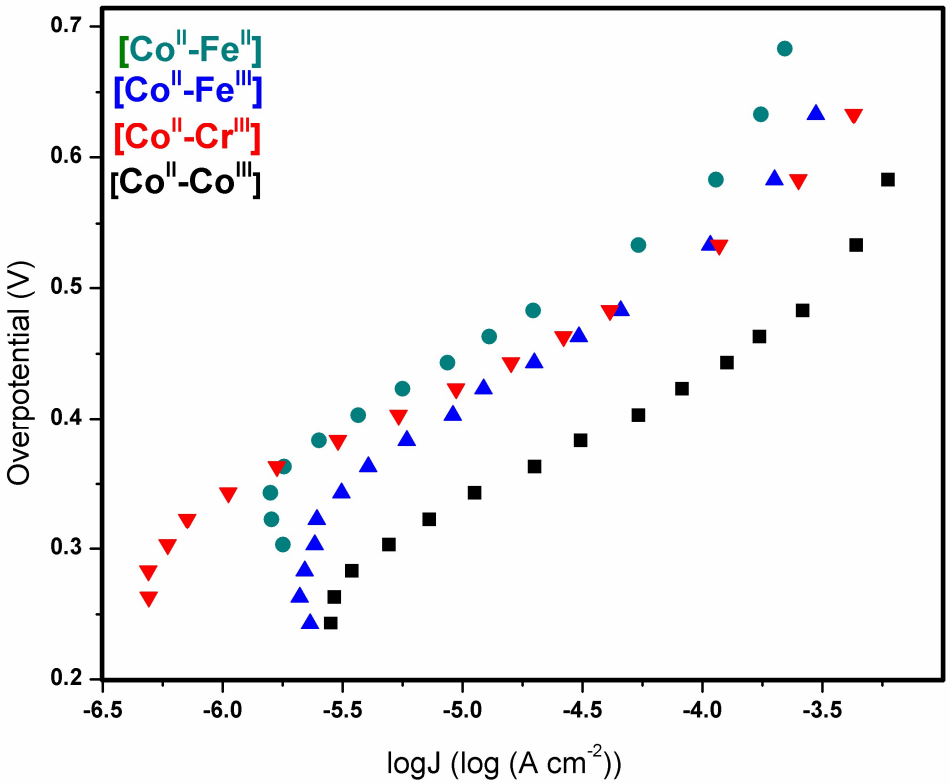

Figure 3. 7. Steady state Tafel analysis of PB derivatives from 1.0 V to 1.5 V vs NHE

Surface concentration was used to assess turnover frequencies (TOFs) of PBAs. TOFs at an overpotential of 400 mV were obtained as 5.0×10^{-2} s^{-1}, 3.0×10^{-3} s^{-1}, 4.4×10^{-3} s^{-1}, and 5.0×10^{-3} s^{-1} for [Co^{II}-Co^{III}], [Co^{II}-Fe^{II}], [Co^{II}-Fe^{III}], and [Co^{II}-Cr^{III}] (Figure 3.8.) according to Equation 3.2 where Q is the charge, t is time, Γ is surface coverage, and 4 is the number of the electrons required for the oxidation of 1 mole of water molecule.

$$\boldsymbol{TOF} = \frac{Q}{4t\Gamma} \qquad \text{(Equation 3.2)}$$

A comparison of TOFs, thus, shows that Co(II) sites available in [Co^{II}-Co^{III}] exhibit the highest the catalytic activity.

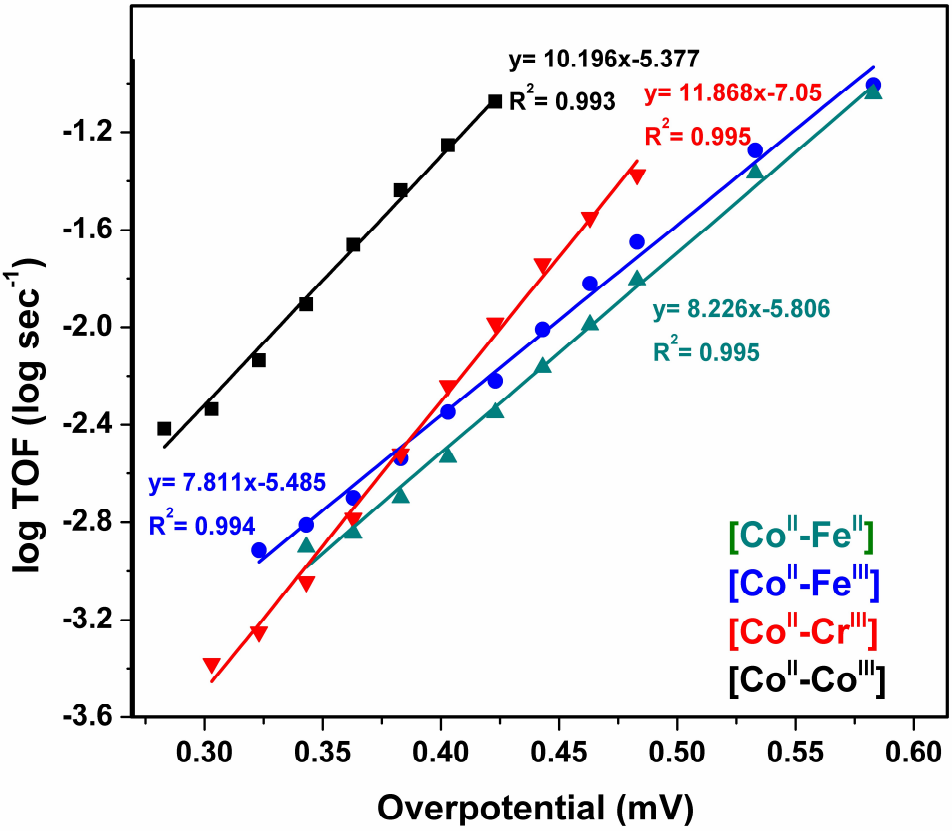

Figure 3. 8. Dependence of turnover frequencies of PB derivatives in 1.1 to 1.4 V vs. NHE range

3.2.3. Chronopotentiometry Measurements

Chronopotentiometry (CP) has been performed to monitor the overpotential required to obtain a current density of 1 mA cm^{-2} during a 2h experiment in a 50 mM KPi buffer at Ph 7.0. The overpotential for [Co^{II}-Co^{III}], decreases slightly at first and then maintains a constant overpotential while it increases gradually until stabilization for other PBAs. The observed overpotentials for 1 mA cm^{-2} are slightly higher than the ones extracted from Tafel slopes due to the formation of O_2 bubbles on the electrode surface during the measurement. CP studies show

that [Co^{II}-Co^{III}] exhibits the lowest overpotential and η_{1mA} is determined to be 531, 578, 661, and 692 for [Co^{II}-Co^{III}], [Co^{II}-Cr^{III}], [Co^{II}-Fe^{III}], and [Co^{II}-Fe^{II}], respectively (Figure 3.9).

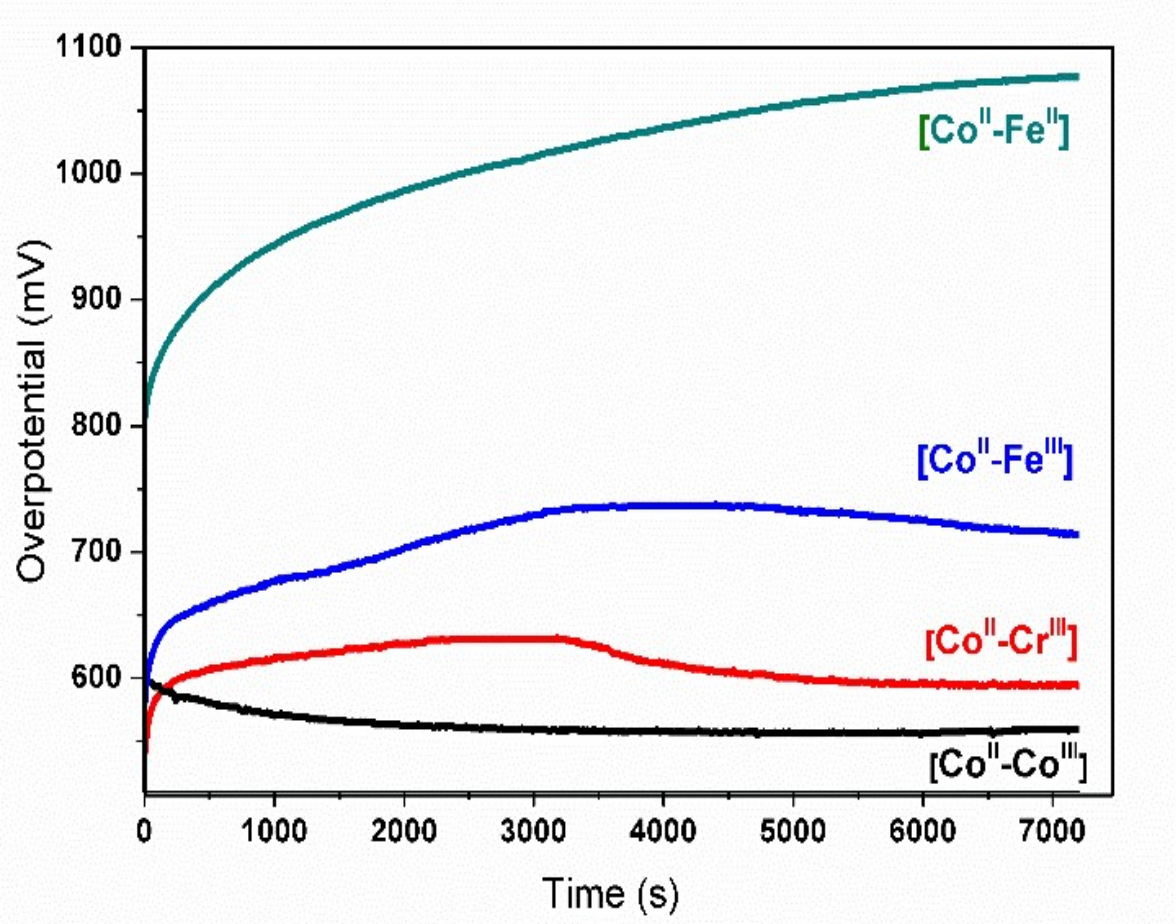

Figure 3. 9. Chronopotentiometry measurement of PB derivatives at 1 mA cm^{-2}

3.2.4. Long Term Stability Measurements

Long term chronoamperometric studies at an applied potential of 1.4 V vs NHE were performed in 50 mM KPi buffer 1 M KNO3 at pH 7 to investigate the stability of the PBA modified electrodes. The current density for each catalyst decreases until it reaches a constant value as previously reported by our group and Galán-Mascarós et al.[47], [81] The same trend can be obtained for four repeating cycles and the close similarity of cyclic voltammetric profiles obtained

after each cycle indicate that catalysts retain their structure even during long term catalytic processes. (Figure 3.10).

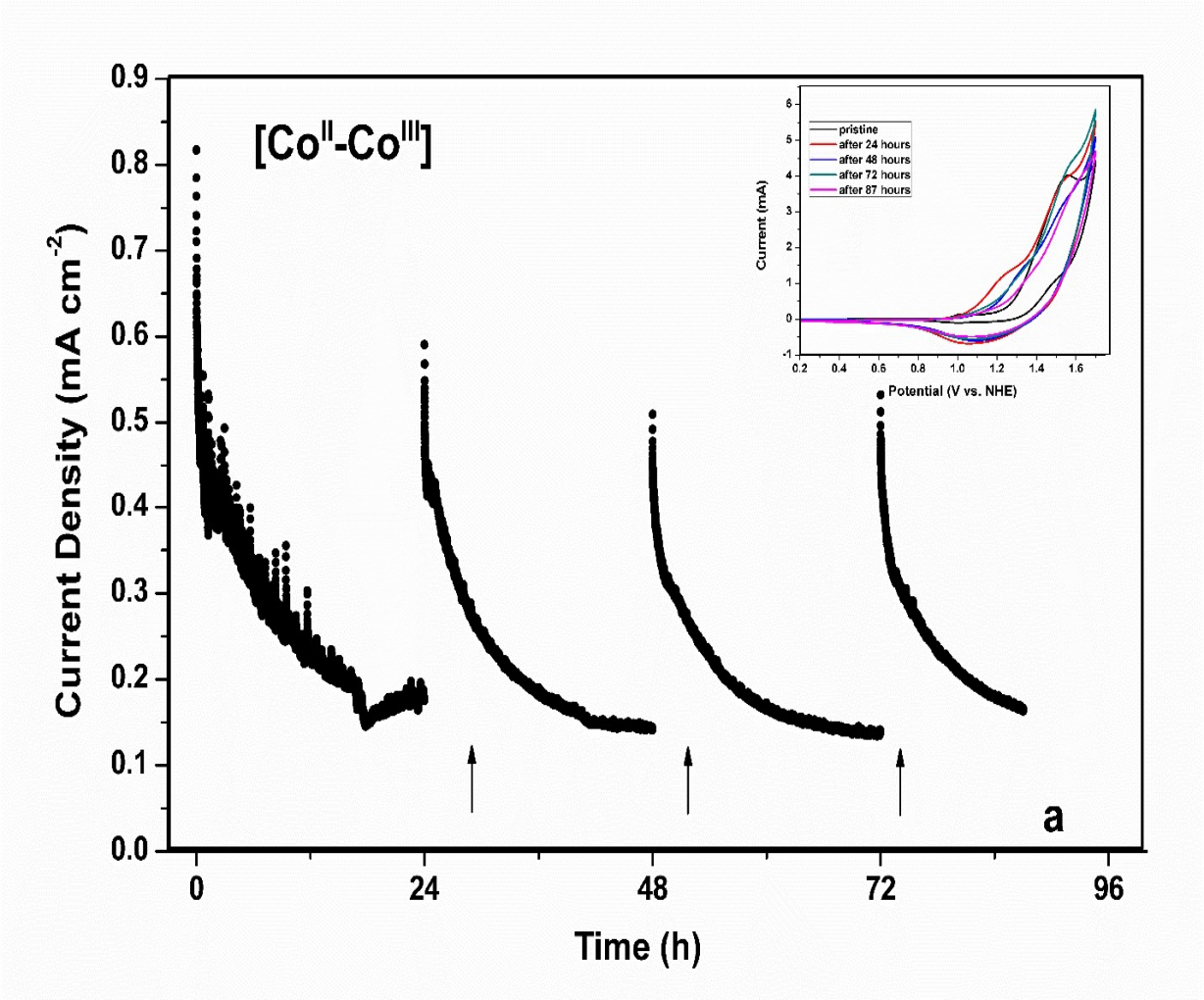

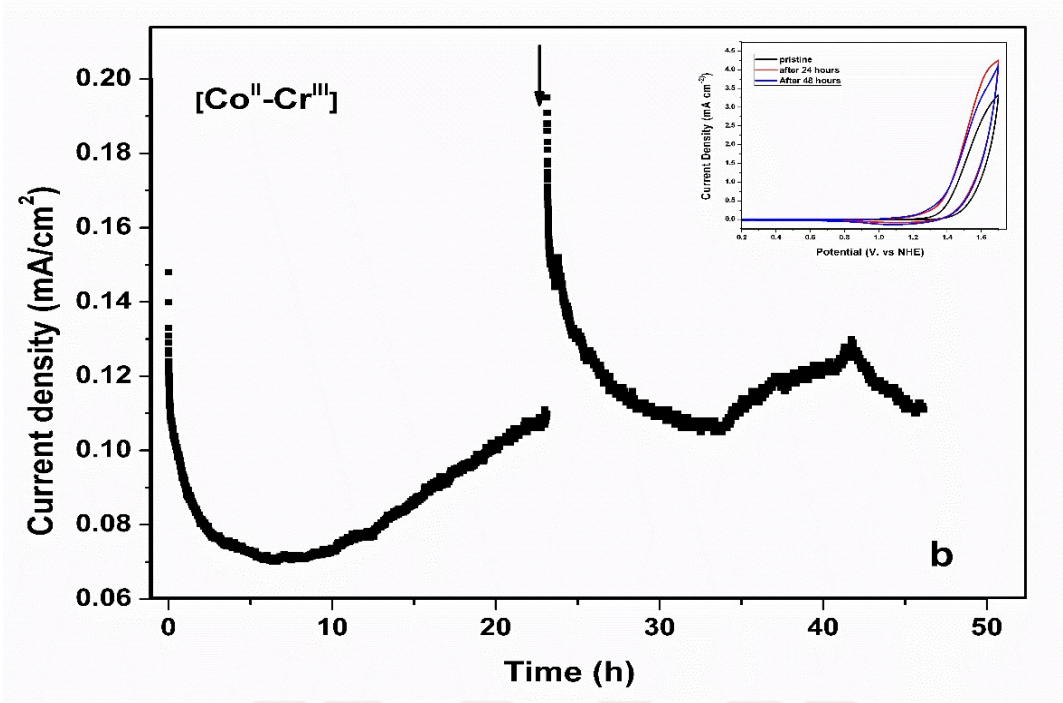

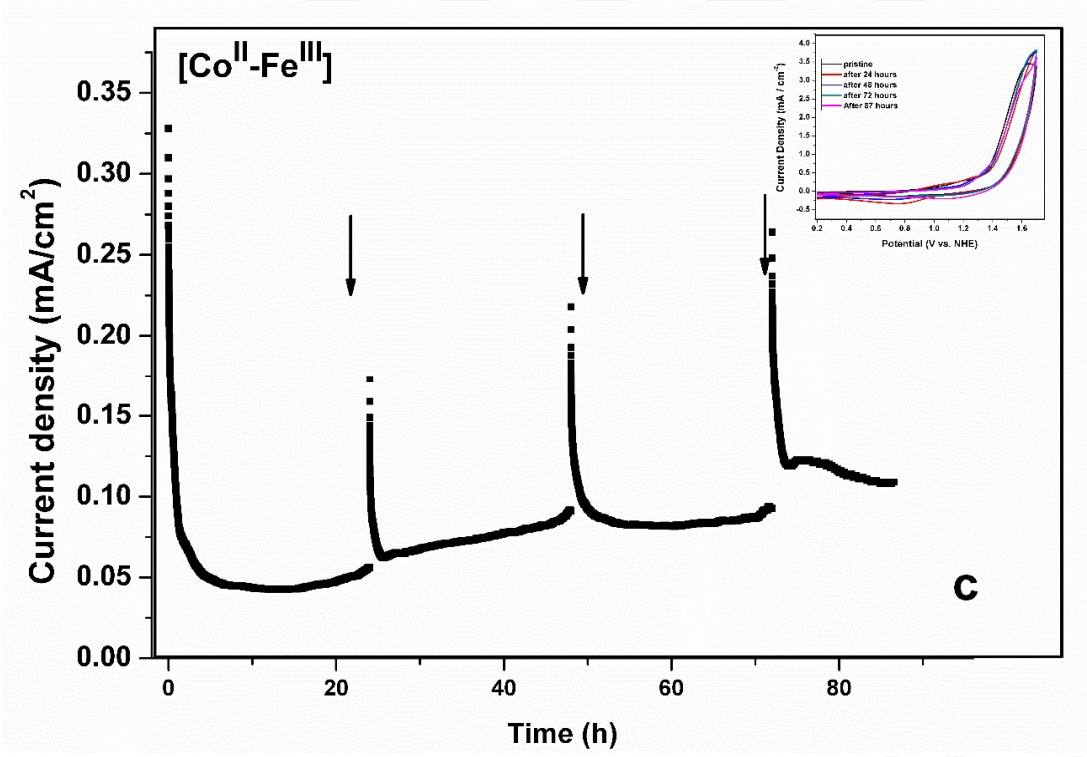

Figure 3. 10. Long term electrolysis studies of PB derivatives of a) [Co^{II}-Co^{III}], b) [Co^{II}-Cr^{III}], and c) [Co^{II}-Fe^{III}] Insets show cyclic voltammograms which are performed after ever 24-hour intervals. Long-term study for [Co^{II}-Fe^{II}] was presented in our previous study.[47]

3.2.5. Faradaic Efficiency Measurement of [Co^{II}-Co^{III}] Prussian Blue Analogue

An electrolysis study equipped with an O_2 probe has been performed with [Co^{II}-Co^{III}] to investigate the origin of current density and Faradaic efficiency. Bulk electrolysis was performed at 1.4 V vs. NHE. The perfect match between the theoretical yield obtained from chronocoulometry measurement and the experimental one obtained from O_2 probe indicates that the only origin of current density is catalytic water oxidation to O_2 evolution process and there are no competing redox reactions (Figure 3.11)

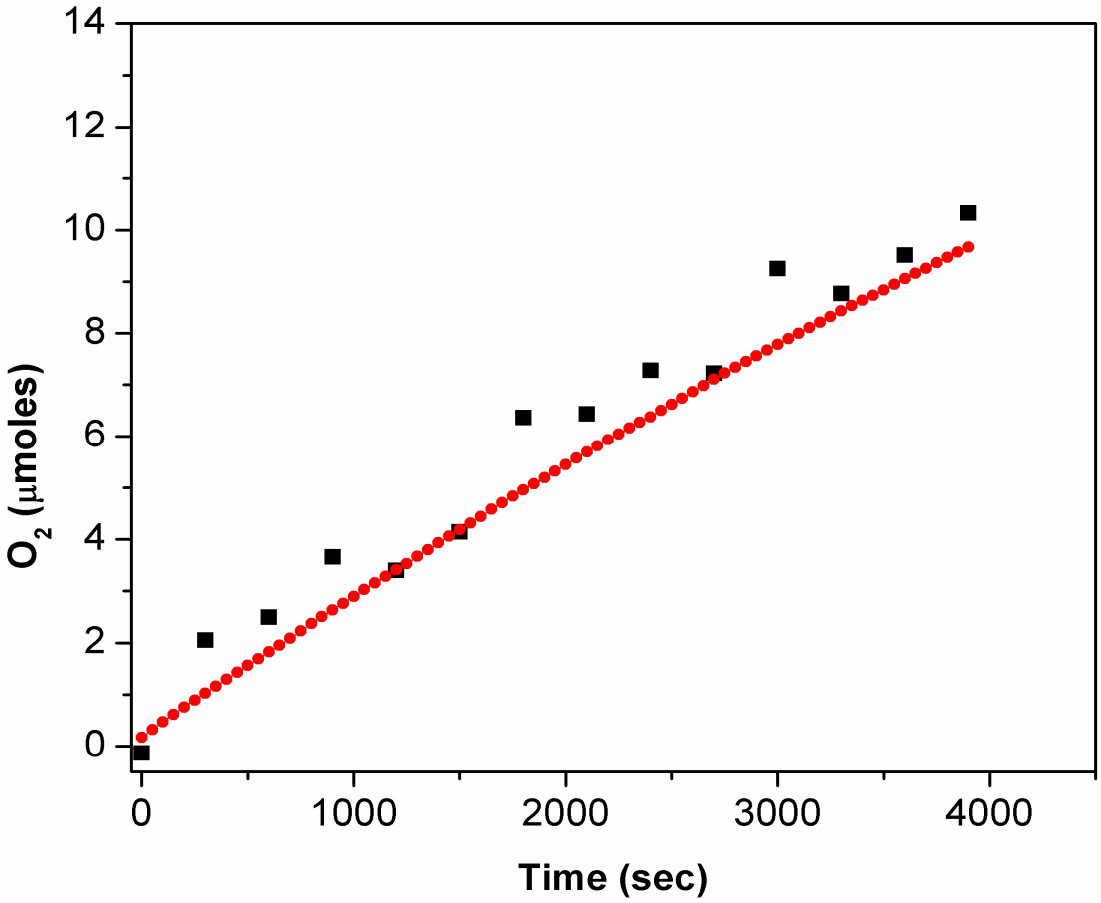

Figure 3. 11. Faradaic Efficiency of [Co^{II}-Co^{III}] measured by dissolved oxygen system. The red line shows the theoretical amount of evolved O_2 during electrolysis and black line shows the experimental amount of O_2.

3.2.6. Summary of The Electrochemical Measurements

The results of the electrochemical experiments of CV, Tafel slopes, surface concentration, CP and their detailed results associated with cyanide stretches of [Co^{II}-Co^{III}], [Co^{II}-Cr^{III}], [Co^{II}-Fe^{III}], and [Co^{II}-Fe^{II}] are listed in Table 3.4.

According to the data, [Co^{II}-Fe^{II}] has the lowest $Co^{2+/3+}$ redox potential, CN^- stretch, surface concentration, and TOF values on the other hand, highest η_{onset} and η_{1mA} values. [Co^{II}-Co^{III}] has highest $\nu(CN^-)$ and TOF values; lowest η_{onset} and η_{1mA}. Tafel slopes vary between 96 and 127, [Co^{II}-Cr^{III}] shows lowest, [Co^{II}-Fe^{III}] has highest Tafel slopes.

Table 3. 4. Summary of electrochemical properties for PBAs.

Compound	$Co^{2+/3+}$ (mV)	ν (CN) (cm^{-1})	TOF (η = 400 mV)	Surface Concentration ($nmol\ cm^{-2}$)	$\eta_{1\ mA}$ from Tafel Plot (mV)	Tafel Slope ($mV\ dec^{-1}$)	$\eta_{1\ mA}$ from CP (mV)	η_{onset} (CV)
[Co^{II}-Co^{III}]	1.010	2176	5.0×10^{-2}	4.11	531	99	565	283
[Co^{II}-Cr^{III}]	1.084	2173	5.0×10^{-3}	3.90	578	96	598	303
[Co^{II}-Fe^{III}]	1.084	2120	4.4×10^{-3}	5.48	661	127	717	323
[Co^{II}-Fe^{II}]	0.995	2072	3.0×10^{-3}	2.00	692	121	1079	343

3.3. CHARACTERIZATION STUDIES ON THE MHCM MODIFIED ELECTRODES

A series of metal hexacyanometales with abbreviations of [Co^{II}-Co^{III}], [Co^{II}-Cr^{III}], [Co^{II}-Fe^{III}], and [Co^{II}-Fe^{II}] have been studied as water oxidation catalysts. Characterizations of the catalysts on electrodes have been performed by Grazing Incidence X- Ray Diffraction, Fourier Transform Infrared Spectroscopy, and X-ray Photoelectron Spectroscopy techniques.

3.3.1. Grazing Incidence (GI) X-Ray Diffraction Studies

XRD analysis in grazing incidence mode was also performed on the catalysts deposited on FTO before (pristine) and after (post-catalytic) the electrocatalytic studies to investigate the structural stability of catalyst during electrocatalysis. No additional peaks were observed in the XRD pattern of post-catalytic samples and the peaks corresponding to Prussian blue type structure remain confirming the stability of catalysts (Figure 3.12).

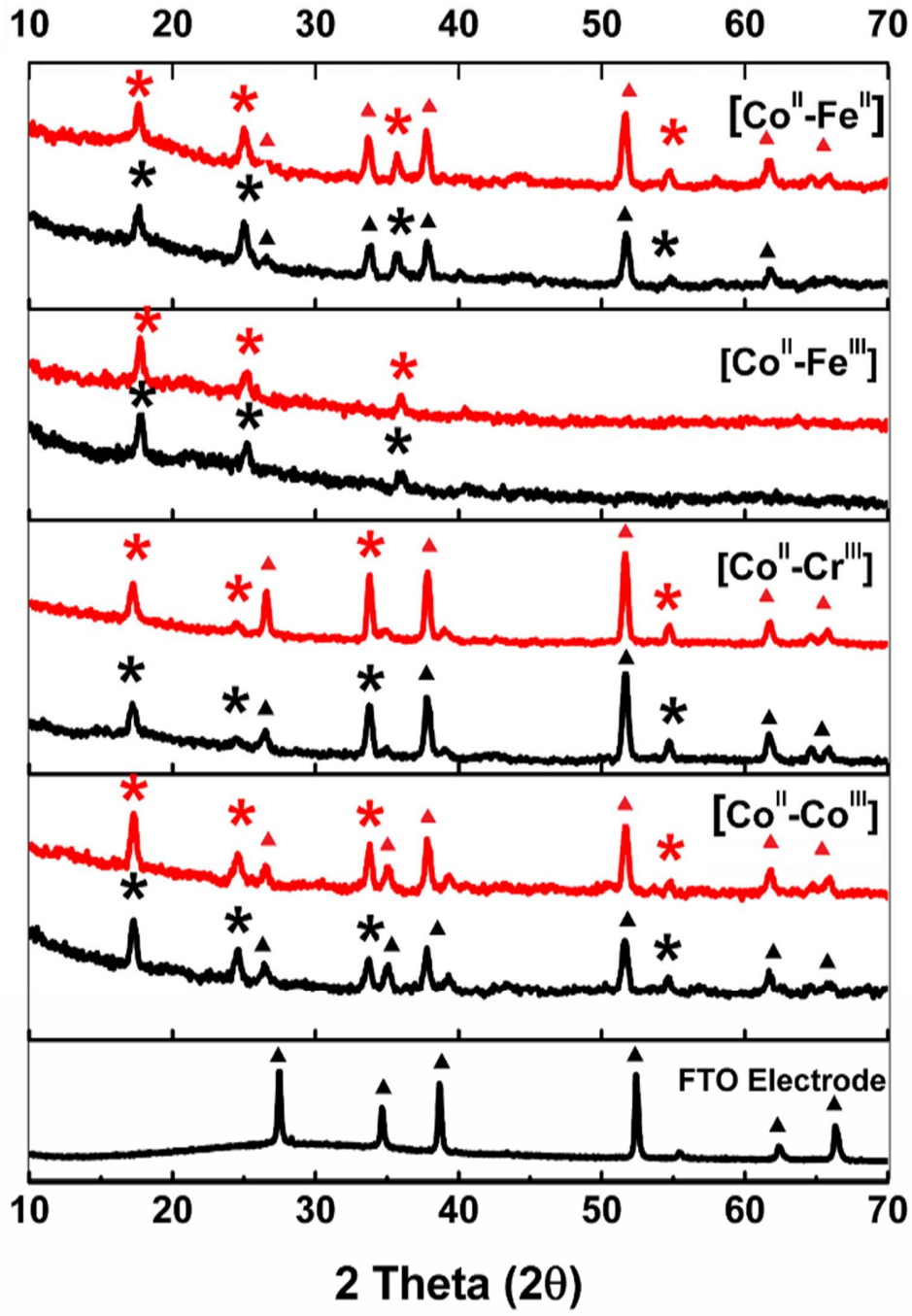

Figure 3. 12. GI- XRD patterns of PB derivatives for pristine (black lines) and post catalytic (red lines). The peaks that are belong to FTO electrode are marked with triangle (▲) and the peaks belong to Prussian blue are marked with asterisk (*).

3.3.2. Infrared Studies

The Infrared analysis was also performed on the post-catalytic samples. The close similarity between the infrared spectra of cyanide stretches of pristine and post catalytic samples indicates that each catalyst retains structural integrity throughout the electrolysis (Figure 3.13).

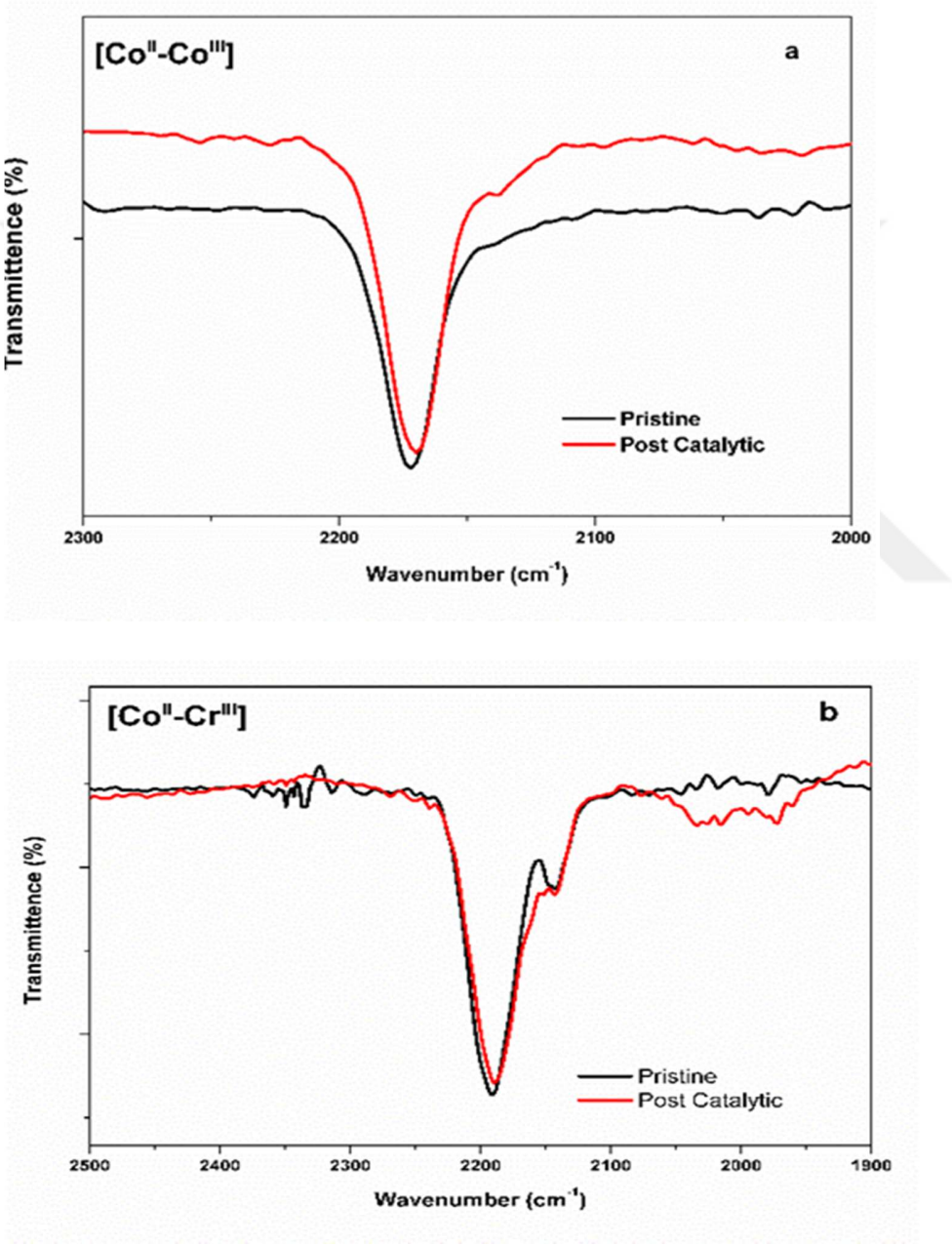

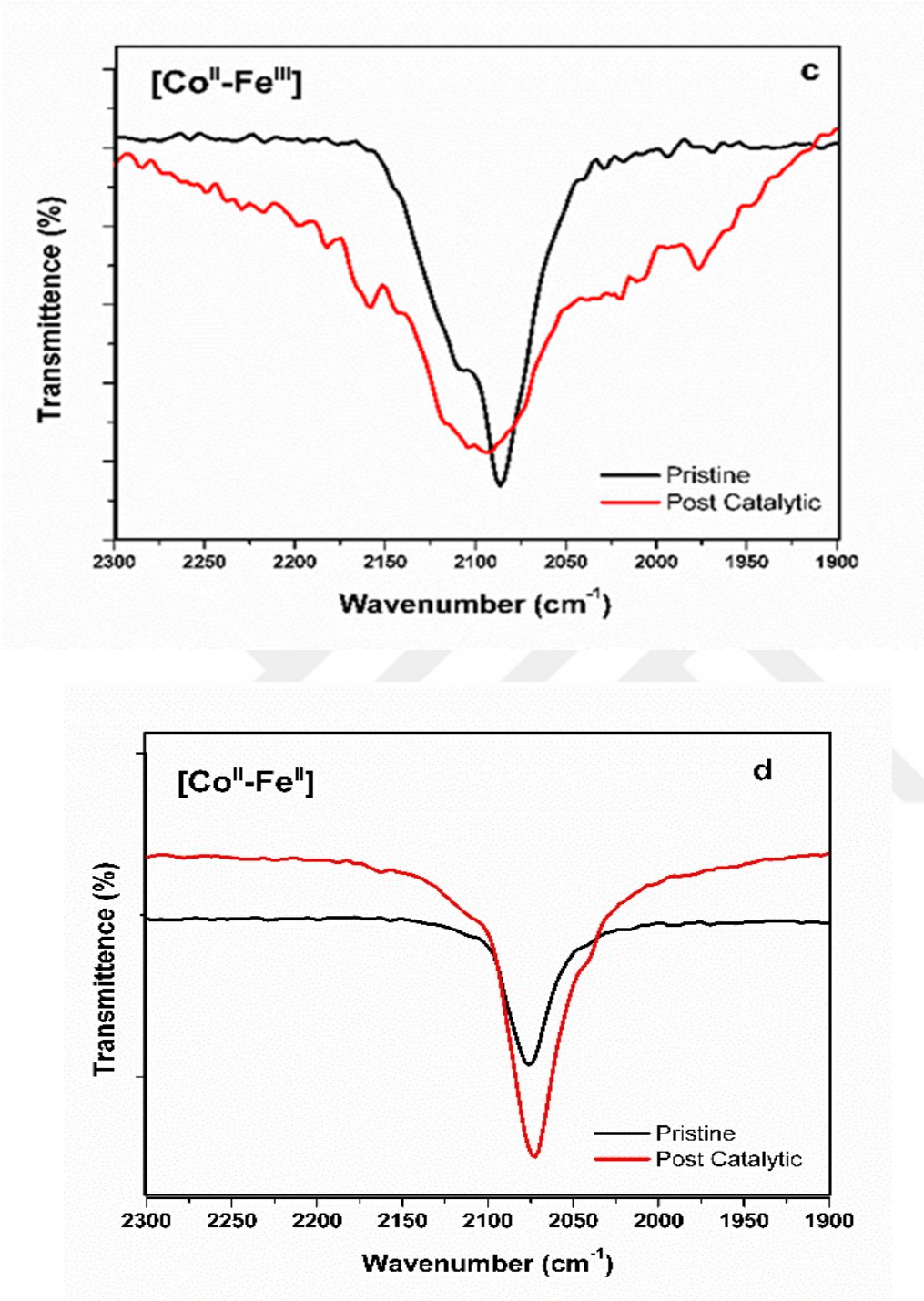

Figure 3. 13. The comparison of Cyanide stretches of pristine (black lines) and post catalytic (red lines) of PB derivatives of a) [Co^{II}-Co^{III}], b) [Co^{II}-Cr^{III}], c) [Co^{II}-Fe^{III}], and d) [Co^{II}-Fe^{II}].

3.3.3. X- Ray Photoelectron Spectroscopy Studies

XPS studies also confirm the remarkable stability of PB electrocatalysts. In order to investigate the oxidation state of electroactive Co^{II} sites in pristine and post catalytic electrodes Co2p signal was examined in the binding energy region between 810-775 eV. In previous studies the binding energy $Co2p_{3/2}$ and $Co2p_{1/2}$ signals of Co^{II} salts have been reported as 782.28 and 798.38 eVs, respectively. For the pristine samples, $Co2p_{3/2}$ and $Co2p_{1/2}$ signals were observed in the same range. The similarity between the binding energies of Co2p signals obtained for pristine PBAs and previously reported Co^{II} salts suggests that the oxidation state of electroactive Co atoms is +2. (Figure 3.14). No significant changes in the $Co2p_{3/2}$ and $Co2p_{1/2}$ signals were observed in the post catalytic samples indicating the stability of the Co^{II} sites.

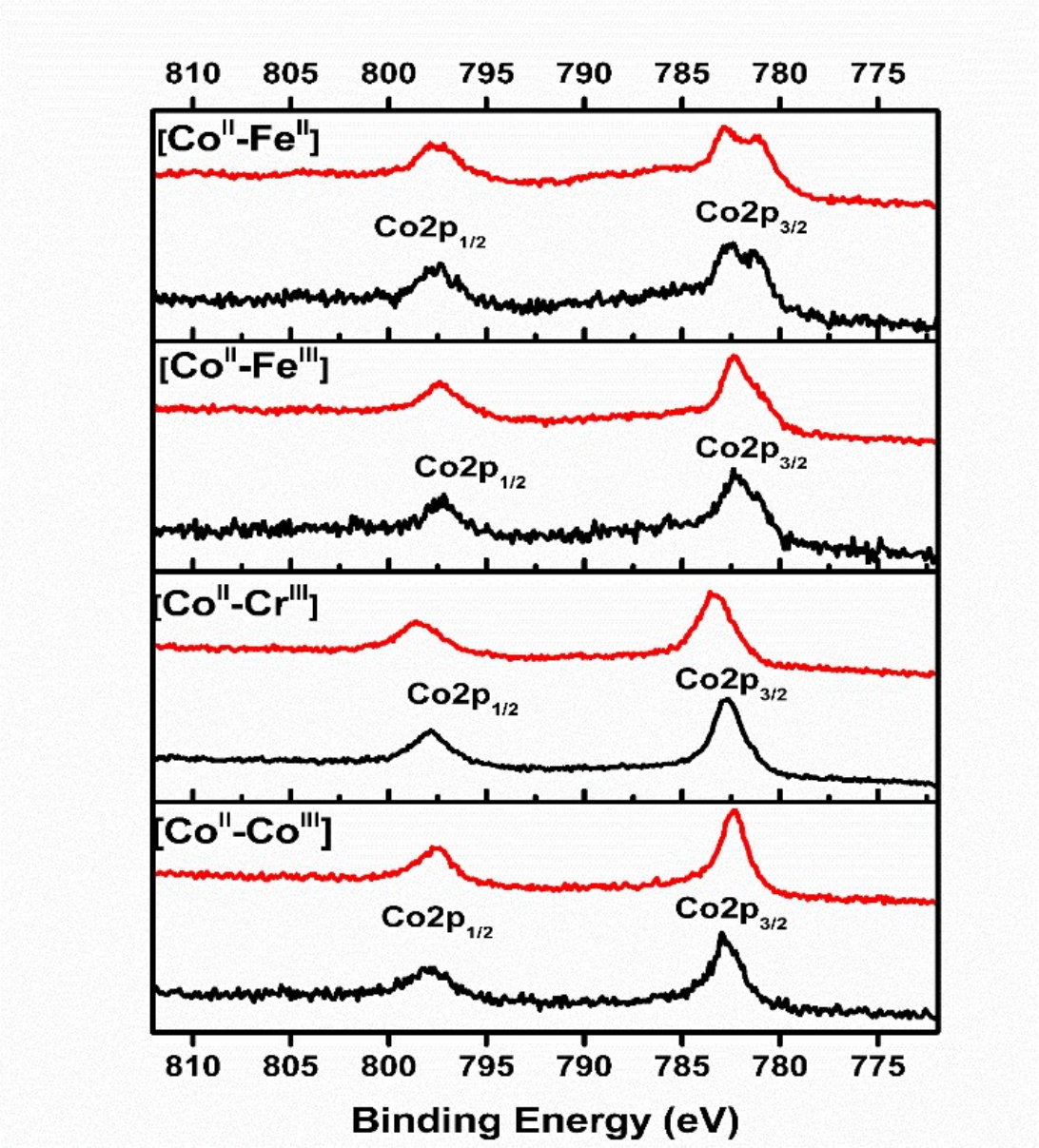

Figure 3. 14. XPS of Co2p region for pristine (black lines) and post catalytic (red lines) of PB derivatives

In addition to Co2p, O1s signals were also examined for both pristine and post catalytic samples (Figure 3.15). The O1s signal whose binding energy is higher than 530 eV indicates the absence of any cobalt oxide species before and after electrochemical experiments.

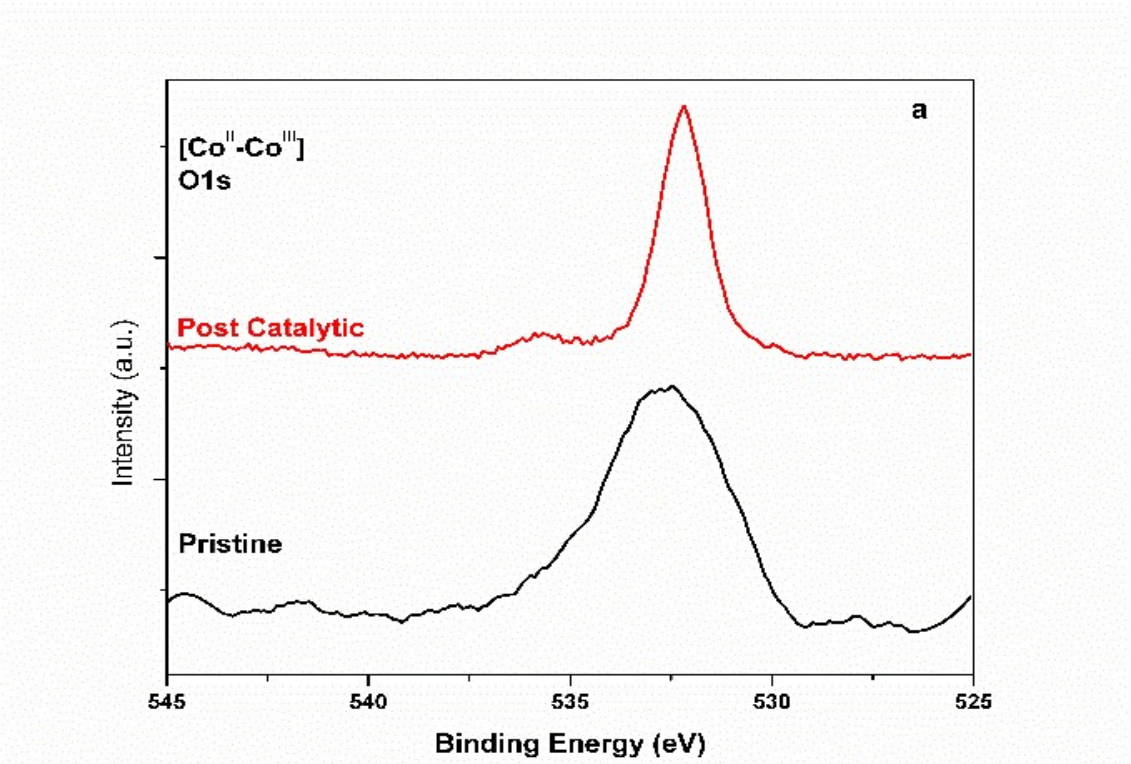
a
[Co^{II}-Co^{III}]
O1s
Post Catalytic
Pristine
Intensity (a.u.)
545
540
535
530
525
Binding Energy (eV)

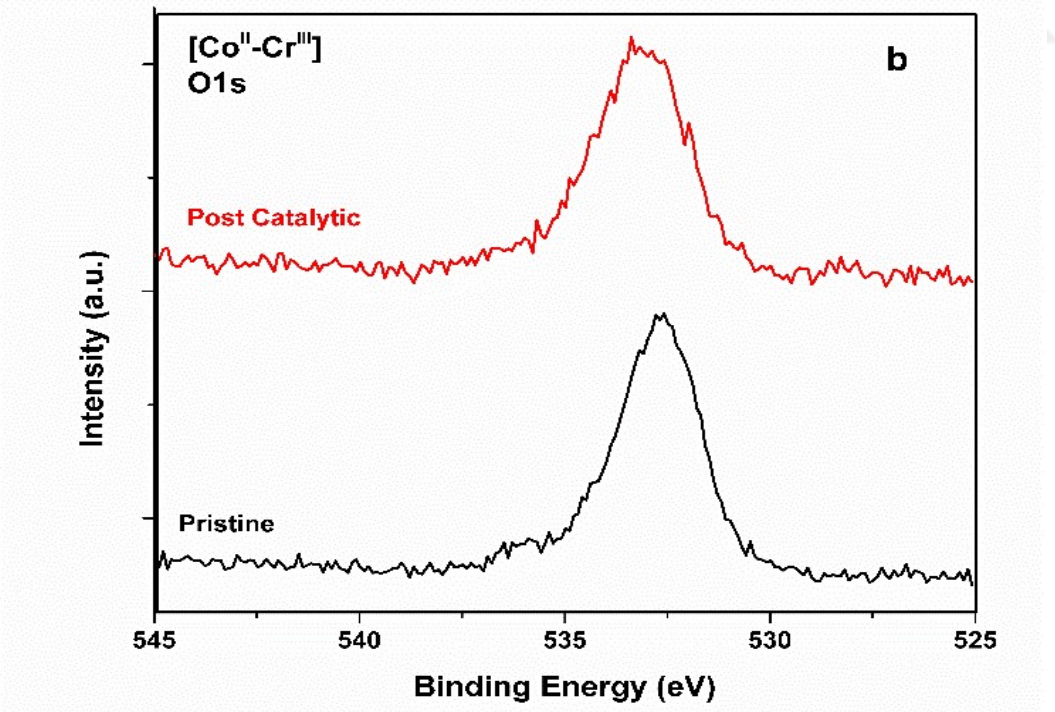
b
[Co^{II}-Cr^{III}]
O1s
Post Catalytic
Pristine
Intensity (a.u.)
545
540
535
530
525
Binding Energy (eV)

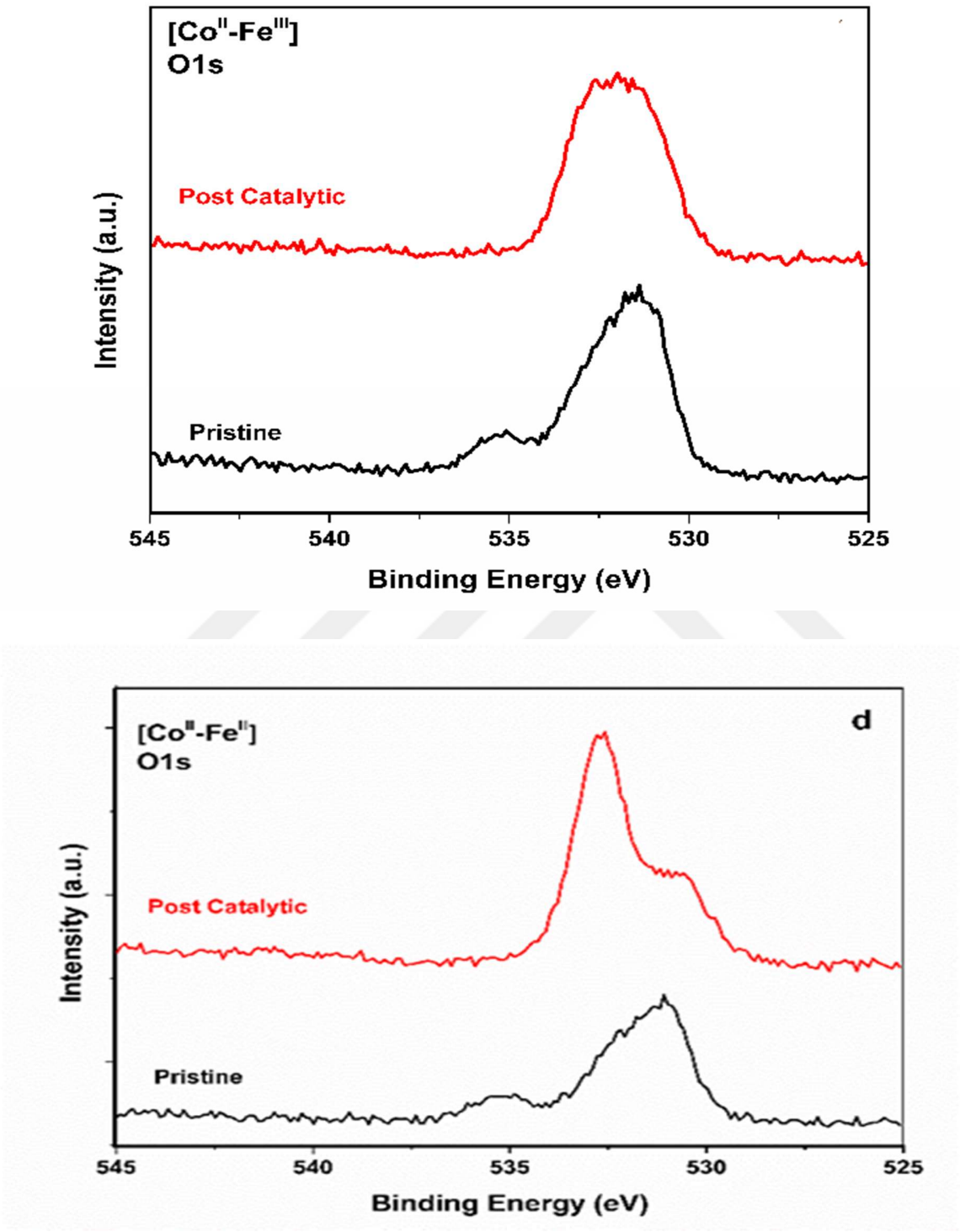

Figure 3. 15. XPS of O1s region for pristine (black lines) and post catalytic (red lines) of PB derivatives of a) [Co^{II}-Co^{III}], b) [Co^{II}-Cr^{III}], c) [Co^{II}-Fe^{III}], and d) [Co^{II}-Fe^{II}].

The observed values are displayed in Table 3.5. A mild noticeable broadening in the O1s signal in the post catalytic samples, indicating a partial and reversible oxidation of electroactive Co^{II} sites.

Table 3. 5. **Binding energies and full width half maxima of XPS peaks for modified electrodes.**

	Pristine						**Post Catalytic**					
	$Co2p_{3/2}$		**$Co2p_{1/2}$**		**O1s**		**$Co2p_{3/2}$**		**$Co2p_{1/2}$**		**O1s**	
	BE (eV)	**FWHM**	**BE (eV)**	**FWHM**	**BE (eV)**	**FWHM**	**BE (eV)**	**FWHM**	**BE (eV)**	**FWHM**	**BE (eV)**	**FWHM**
[Co^{II}-Co^{III}]	782.98	3.43	797.78	2	532.58	4.09	782.28	3.14	797.28	2.2	532.48	2.69
[Co^{II}-Cr^{III}]	782.68	3.34	797.68	2.6	532.68	3.26	783.58	3.38	798.48	2.4	533.38	3.45
[Co^{II}-Fe^{III}]	782.38	4.46	797.18	3	531.78	3.5	782.28	2.58	797.38	3.3	532.48	3.5
[Co^{II}-Fe^{II}]	782.58	4.43	797.38	2	531.28	2.86	782.88	4.78	797.68	2.2	532.58	3.48

3.4. MECHANISTIC STUDIES OF METAL HEXACYANOMETALATES

The CN stretch could be considered as the fingerprint for cyanide-based coordination compounds. The comparison of the shift in the cyanide stretch can be used not only to confirm the M-CN-M' type coordination bonding but also to evaluate the oxidation states, and thus, electron densities of metal ions. Considering that the cyanide stretch shifts to higher frequencies as the oxidation state of the metal increases a direct correlation can be established with the shift of the cyanide stretch and the electron deficiency of Co^{II} centers. The comparison of cyanide stretches implies that the electron densities of Co^{II} sites in Prussian blue analogues can be ordered as: $[Co^{II}\text{-}Co^{III}] \sim [Co^{II}\text{-}Cr^{III}] < [Co^{II}\text{-}Fe^{III}] < [Co^{II}\text{-}Fe^{II}]$ (Figure 3.16).

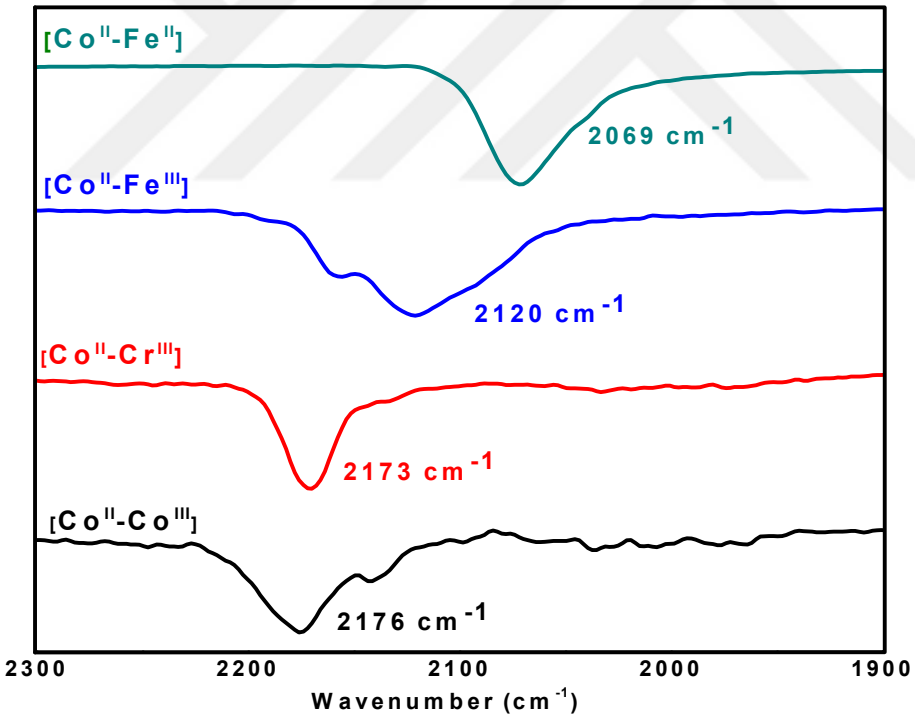

Figure 3. 16. FTIR spectra of PB derivatives that shows cyanide stretches

This result is also in good agreement with the binding energies of Co2p electrons obtained by XPS studies. The ordering of Co $2p_{3/2}$ peak is as $[Co^{II}\text{-}Co^{III}]$> $[Co^{II}\text{-}Cr^{III}]$> $[Co^{II}\text{-}Fe^{III}]$> $[Co^{II}\text{-}Fe^{II}]$, which points out that Co^{II} sites in $[Co^{II}\text{-}Co^{III}]$ analogue have the lowest electron densities among all. The evaluation of electron densities can give insight about the rate determining step (r.d.s.) in water oxidation catalysis. Two steps haven generally been reported to compete with each other as the r.d.s. in water oxidation process;

i) Co^{III}/Co^{IV} oxidation step and

ii) the nucleophilic attack of water to the electrophilic oxygen atom of Co^{IV}=O species that results in O–O bond formation. The increase in the electron density of Co^{II} site facilitates the former step while it decreases the electrophilic nature of oxo-intermediate and, thus, impedes the latter. The aforementioned discussion on the comparison of electron densities of Co^{II} sites in PBAs and their electrocatalytic performances clearly show that $[Co^{II}\text{-}Co^{III}]$ stands forward as the most efficient catalysts among PBAs while it has Co^{II} sites with the lowest electron density. This correlation points out that the nucleophilic attack of water to Co^{IV}=O intermediate is the r.d.s. of water oxidation process for PBAs. Herein, it should be noted that although there are other parameters such as surface concentration and surface morphology that affects the catalytic activity of heterogeneous systems. Estimation of surface concentration via electrochemical studies show that there are no considerable changes in the bulk properties of electrodes.

A further analysis of the mechanism was made based on the Pourbaix diagram (Figure 3.17), which was obtained by performing CVs for $[Co^{II}\text{-}Co^{III}]$ at different pHs (Figure 3.18). The diagram shows that Co^{2+}/Co^{3+} redox process is pH dependent in the pH 4–10 range with a slope of 64 mV $\log[H^+]^{-1}$, which refers to a $1H^+–1e^-$ process.

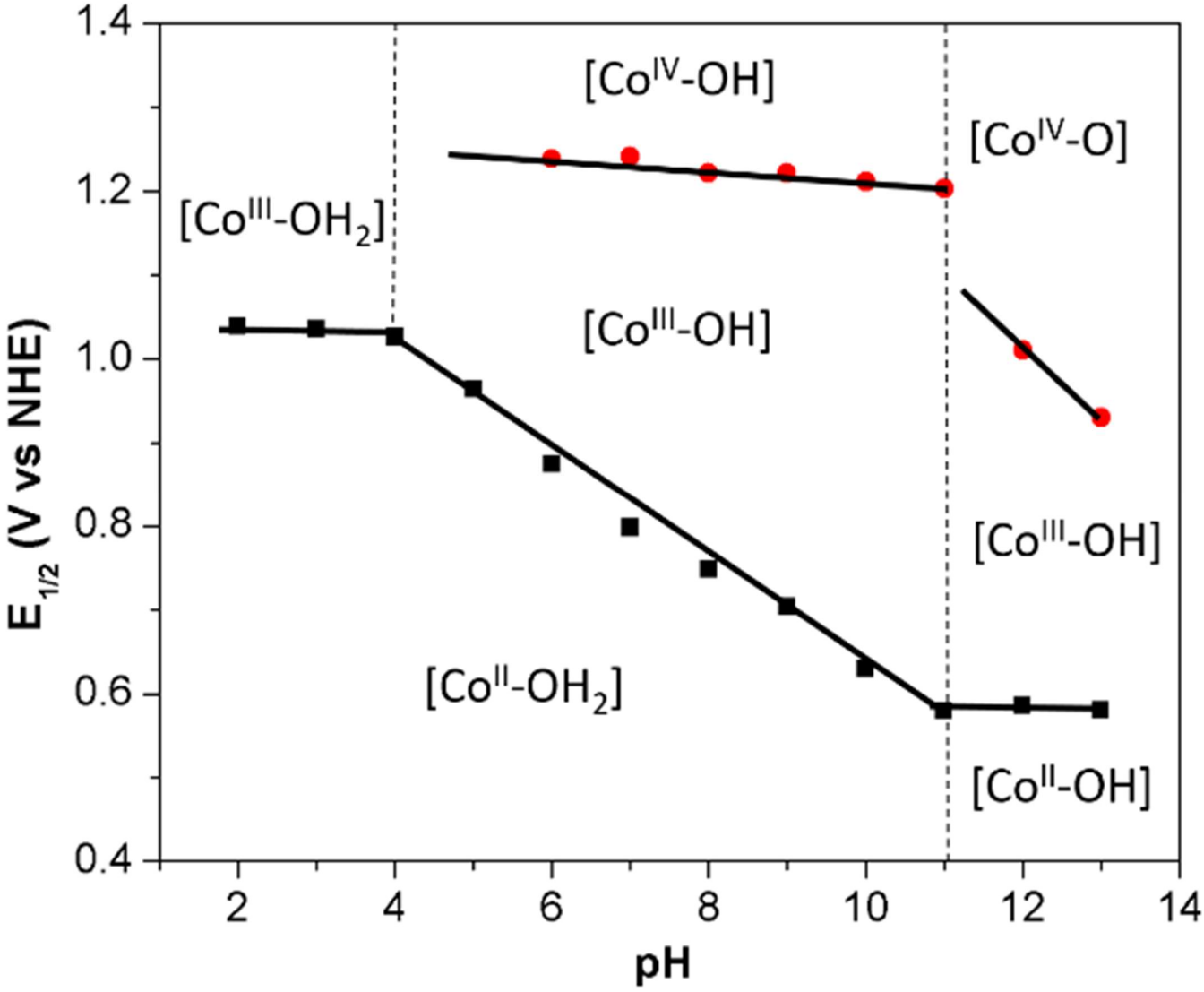

Figure 3. 17. Pourbaix Diagram of [Co^{II}-Co^{III}] in KPi buffer at pHs from 2 to 13. Cyclic Voltammograms that are recorded at these pHs are shown in Figure (3.18)

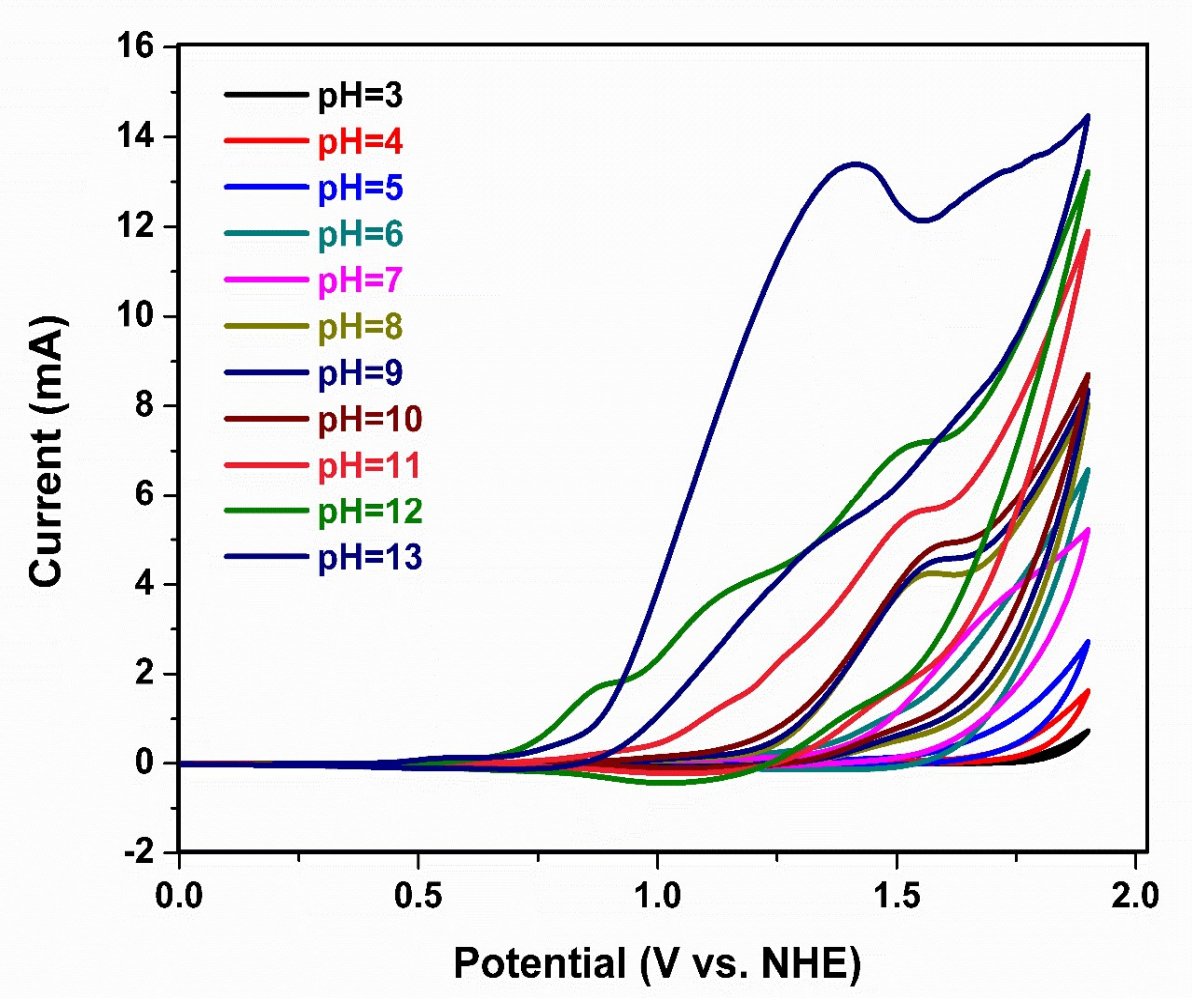

Figure 3. 18. Cyclic Voltammograms of [Co^{II}-Co^{III}] in KPi buffer solution at pHs between 3 and 13.

Interestingly, the half-potential for the Co^{3+}/Co^{4+} is preserved regardless of pH (<11), which indicates that a hydroxyl group is coordinated to the catalytically active Co^{IV} intermediate at neutral conditions. [N_5Co^{IV}-OH] intermediate could undergo deprotonation in subsequent steps to form [N_5Co^{IV}=O] complex, followed by the nucleophilic attack of water to form a [N_5Co^{IV}-OO] complex, which is one of the essential steps for O-O bond formation. A slightly different mechanism than the commonly-accepted mechanism for oxides was, thus, proposed for PBAs. Proposed mechanism for PBAs for WOC is shown in Figure 3.19.

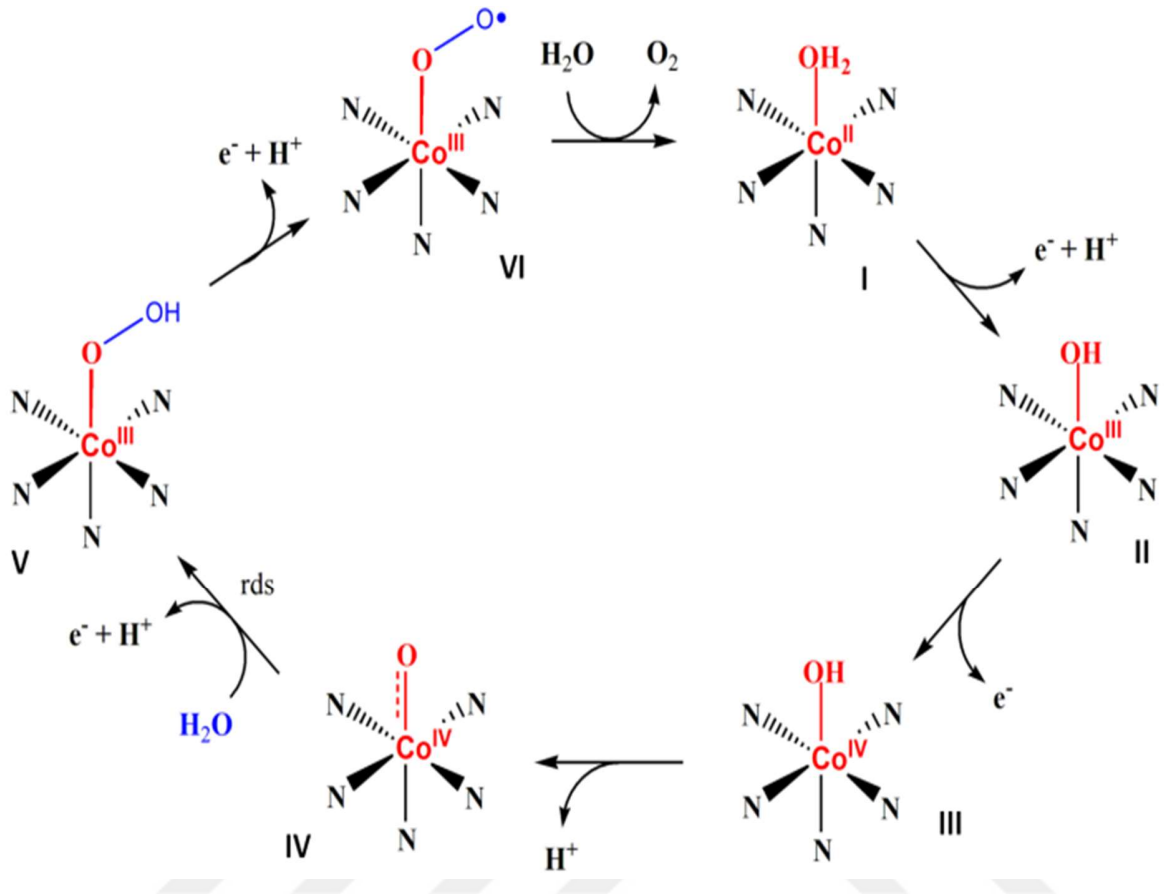

Figure 3. 19. Proposed mechanism for water oxidation process for PBAs.

CHAPTER 4

RESULTS AND DISCUSSION FOR METAL PENTACYANOMETALATES (MPCMs) as WATER OXIDATION CATALYST

4.1. INTRODUCTION

In this chapter, the effect of morphology of Prussian blue on electrocatalytic water oxidation is investigated. NH_3 ligand in sodium pentacyano ammino ferrrate (II) compound is substituted with a N-donor ligand which is 1-heptyl 4-(4 pyridyl) pyridinium bromide (HPPB) (Figure 4.1).

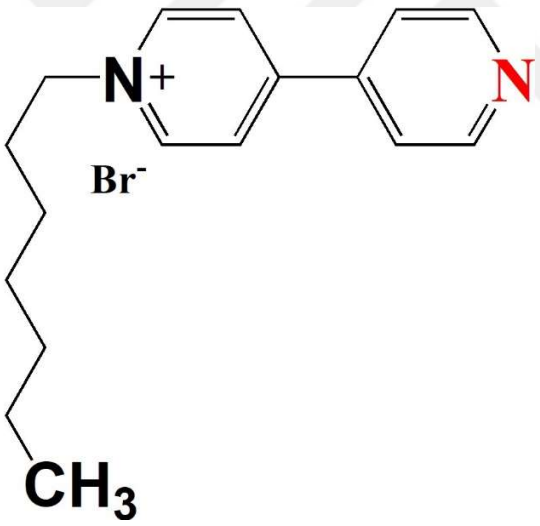

Figure 4. 1. Schematic representation of HPPB Ligand

1-heptyl 4-(4 pyridyl) pyridinium bromide is one of the ligands that can bind to pentacyanoferrate complex to synthesize amorphous PB analogues. When cobalt(II) ion is added to a solution containing $[Fe(CN)_5HPPB]^{2-}$ complex, long carbon chain of HPPB ligand contributes to create steric stabilization and to limit the growth of Prussian blue 3D network.

Reactions of synthesizing amorphous cobalt HPPB coordinated pentacyanoferrate are shown in Figure 4.2.

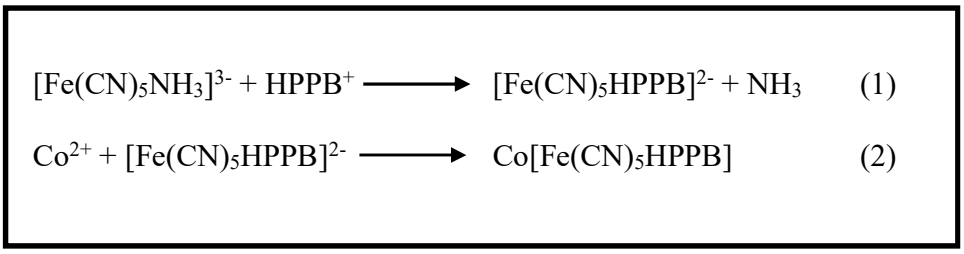

Figure 4. 2. Synthesis of Co[$Fe(CN)_5$-HPPB]

4.2. CHARACTERIZATION STUDIES

In this chapter, the characterizations of 1-heptyl 4-(4 pyridyl) pyridinium bromide (HPPB) coordinated cobalt pentacyanoferrate which is used as water oxidation catalyst are shown. Powder XRD, FTIR, EDX, and electrochemistry studies were performed to characterize the compounds of interest.

4.2.1. Powder X-Ray Diffraction Studies

Although metal hexacyanometalates exhibit diffraction patterns with sharp peaks that belongs to Fm3m space group (JCPDS Card No: 73-0687), broader peaks are observed for Co[$Fe(CN)_5$-HPPB], which are good indicators of amorphous nature of Co[$Fe(CN)_5$-HPPB].

The powder XRD analysis of both HPPB coordinated pentacyano ferrate [$Fe(CN)_5$-HPPB]$^{2-}$ and HPPB coordinated cobalt pentacyano ferrate Co[$Fe(CN)_5$-HPPB]. are shown in Figure 4.3.

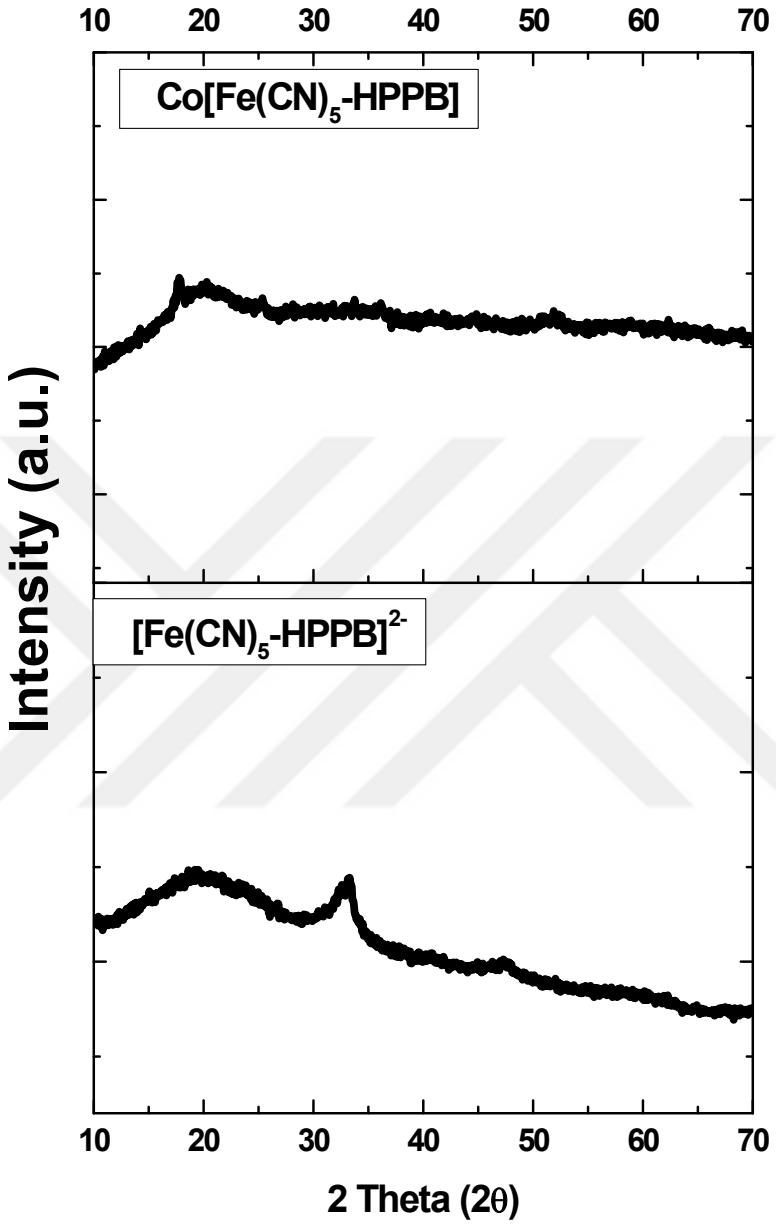

Figure 4. 3. X-Ray diffraction patterns of $[Fe(CN)_5\text{-HPPB}]^{2-}$ and $Co[Fe(CN)_5\text{-HPPB}]$

4.2.2. Infrared Studies

Infrared studies were performed to investigate the structure of the product. Infrared technique is a useful tool especially for the analysis of cyano complexes since CN bond exhibits a strong and sharp peak in the 2200-2000 cm^{-1} range, which is highly dependent on the type of cyanide bonding. Since HPPB and CN^{-1} ligands have similar π accepting ability, the π- back donation of iron to CN ligand's antibonding orbitals becomes less effective for $[Fe(CN)_5\text{-HPPB}]^{2-}$ complex. Consequently, pentacyanoferrate complex has higher $\upsilon(CN^{-1})$. The cyanide stretch of $[Fe(CN)_5\text{-HPPB}]^{2-}$ was observed at 2049 cm^{-1} with 16 cm^{-1} increment in CN^{-1} stretch which is a good indication of the formation of HPPB coordinated pentacyanoferrate compound. The CN stretch frequency further increased after addition of Co^{2+} ions to the $[Fe(CN)_5\text{-HPPB}]^{2-}$ to obtain Prussian blue. In addition, the bands in the region between 400-550 cm^{-1} are attributed to Co-CN-Fe bending mode at $Co[Fe(CN)_5\text{-HPPB}]$.

The cyanide stretches for each complex shows the linear bridging of Fe-CN-Co binding mode Infrared Spectra of HPPB, $[Fe(CN)_5NH_3]^{3-}$, $[Fe(CN)_5\text{-HPPB}]^{2-}$, and $Co[Fe(CN)_5\text{-HPPB}]$ are shown in Figure 4.4.

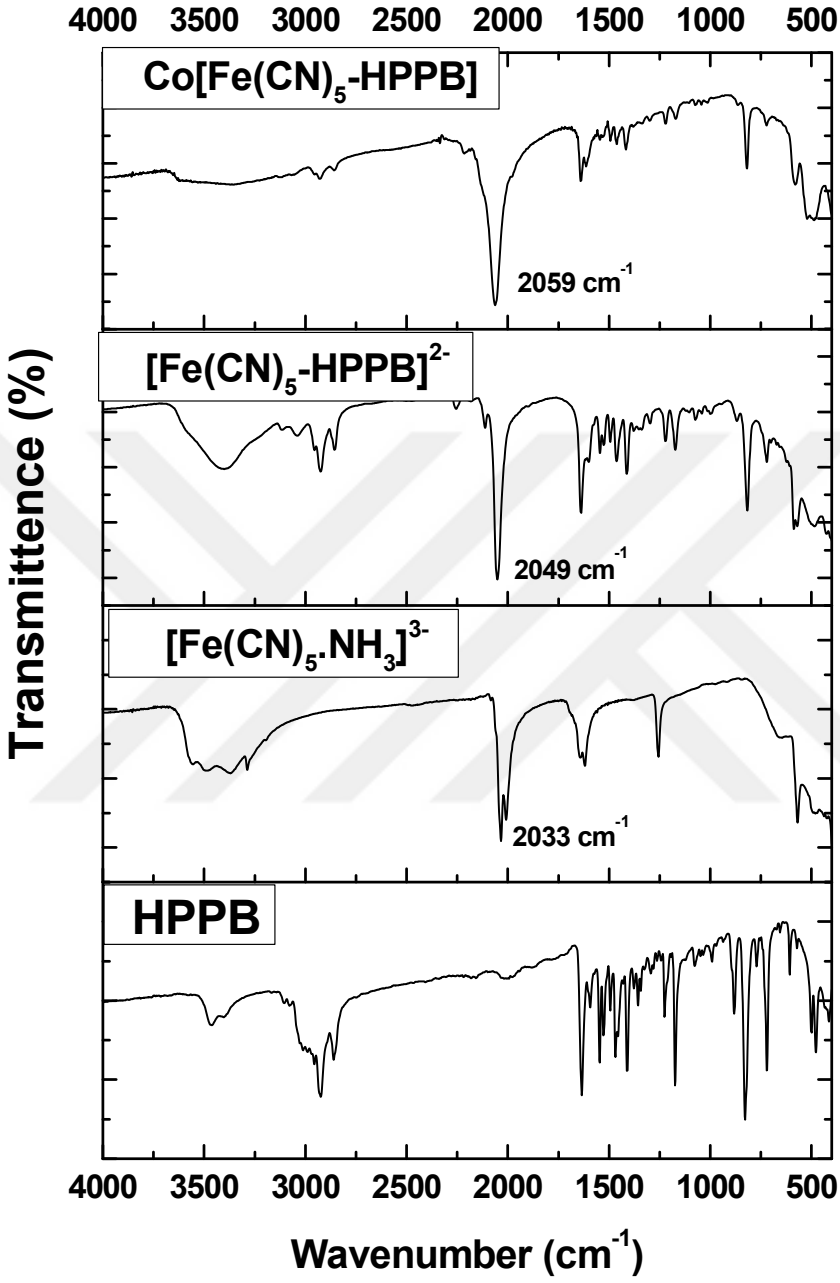

Figure 4. 4. Infrared Spectra of HPPB, $[Fe(CN)_5NH_3]^{3-}$, $[Fe(CN)_5\text{-}HPPB]^{2-}$, and $Co[Fe(CN)_5\text{-}HPPB]$

4.2.3. Energy Dispersed X- Ray Analysis

According to EDX analysis, Co[Fe(CN)$_5$-HPPB] compound has the atomic ratio of Co to Fe is equal to approximately 1.5 with traces of Na and Br ions (Table 4.1). According to EDX analysis (Figure 4.5) the empirical formula of the Co[Fe(CN)$_5$-HPPB] compound has been determined as $Co_{1.5}$[Fe(CN)$_5$HPPB]. xH_2O.

Table 4. 1. Atomic Percent Ratios of the Elements in Co[Fe(CN)$_5$-HPPB]

	C	N	O	Na	Fe	Co	Br
%	58	11.70	2.86	0.35	10.76	15.81	0.52

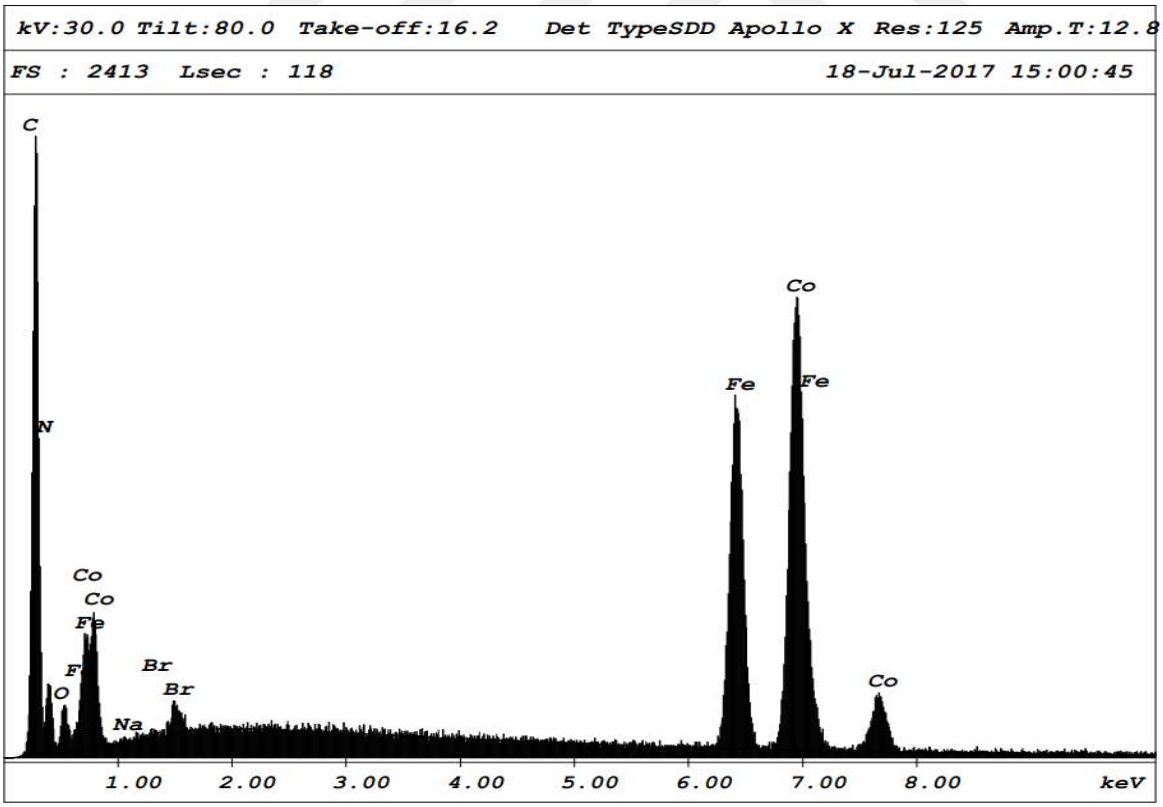

Figure 4. 5. EDX spectrum of Co[Fe(CN)$_5$-HPPB]

4.3. ELECTROCHEMICAL WATER OXIDATION STUDIES

4.3.1. Cyclic Voltammetry Measurements

Cyclic voltammogram of Co [$Fe(CN)_5$-HPPB] deposited onto FTO electrode was recorded in the 0.2 - 1.7 V range with respect to NHE reference electrode. A quasi-reversible redox couple was observed with the oxidation peak at 0.76 V and a reduction peak at 0.53 V vs NHE. Half wave potential ($E_{1/2}$) is 0.63 V. This one electron process can be attributed to Co^{II} /Co^{III} redox couple. An irreversible peak, appeared above 1.1 V, corresponds to Co^{III} /Co^{IV} catalytic water oxidation process. The cyclic voltammogram of Co [$Fe(CN)_5$-HPPB] compared with blank electrode is shown in Figure 4.6.

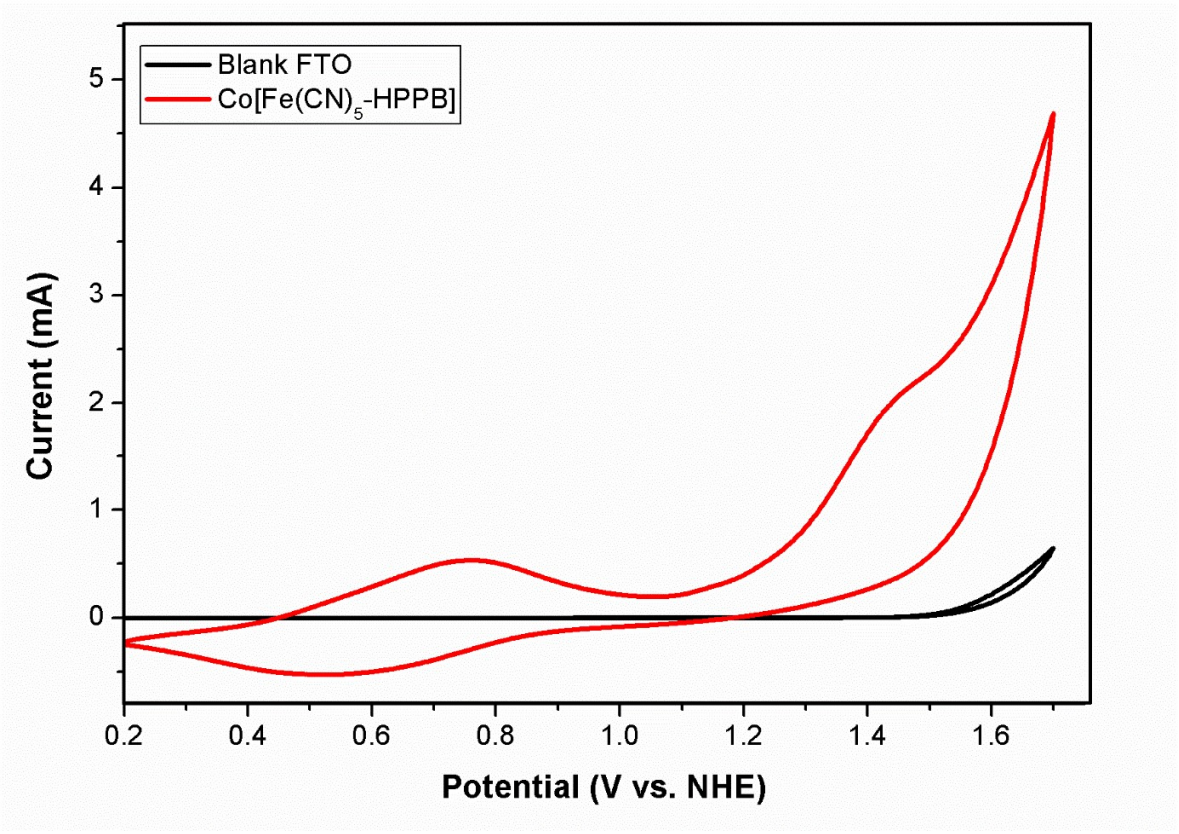

Figure 4. 6. Cyclic Voltammogram of Co[$Fe(CN)_5$-HPPB] (red) and Blank FTO electrode (black)

The Co^{II}/Co^{III} redox pair was evaluated to determine the surface concentration of electroactive cobalt sites on the electrode. For this reason, the cyclic voltammograms in the 0.4-1.05 V potential range was recorded with different scan rates between 2-20 mV/sec and performed in 50 mM KPi buffer 1 M KNO_3 at pH 7 (Figure 4.7). The reduction peak current (mA) versus scan rate *v* (mV/sec) was plotted. By using the slope of the linear trend line according to equation 3.1, the electroactive Co^{II} concentration of Co[Fe(CN)$_5$-HPPB] on the electrode surface was calculated as 12.5 nmol.cm^{-2}. When this value is compared with CHCMs in chapter 3, the surface coverage is increased at least 2- fold.

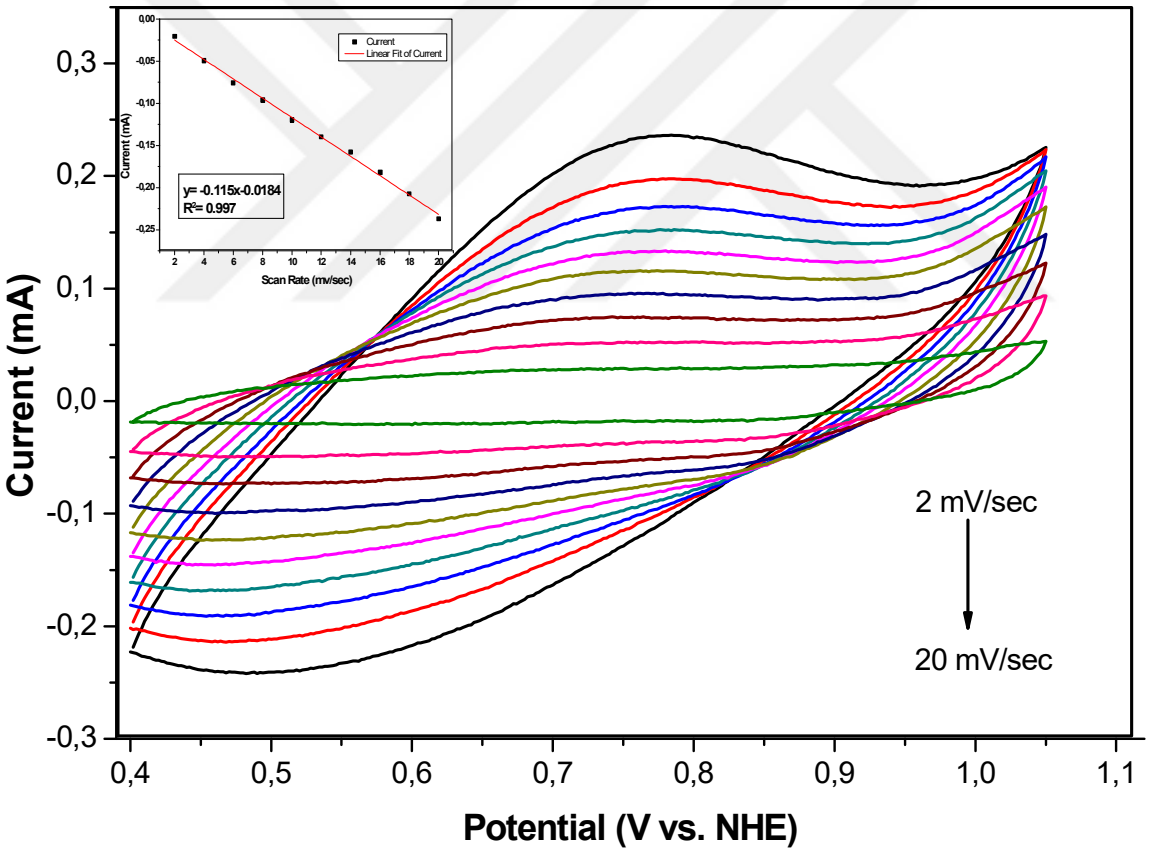

Figure 4. 7. Cyclic Voltammograms of Co[Fe(CN)$_5$-HPPB recorded at different sweep rates. Insets show the linear relationship between peak current of $Co^{2+/3+}$ redox couple and sweep rates.

4.3.2. Tafel Slope and Turnover Frequency Analyses

Steady state chronoamperometry measurement was performed at different applied potential along 600 s of equilibrium time. The measurements were recorded in 50 mM Kpi buffer at pH 7.The steady state current density results were collected for each overpotential to evaluate the catalytic activity of Co[Fe(CN)$_5$-HPPB]. The Tafel Plot is shown in Figure 4.8.

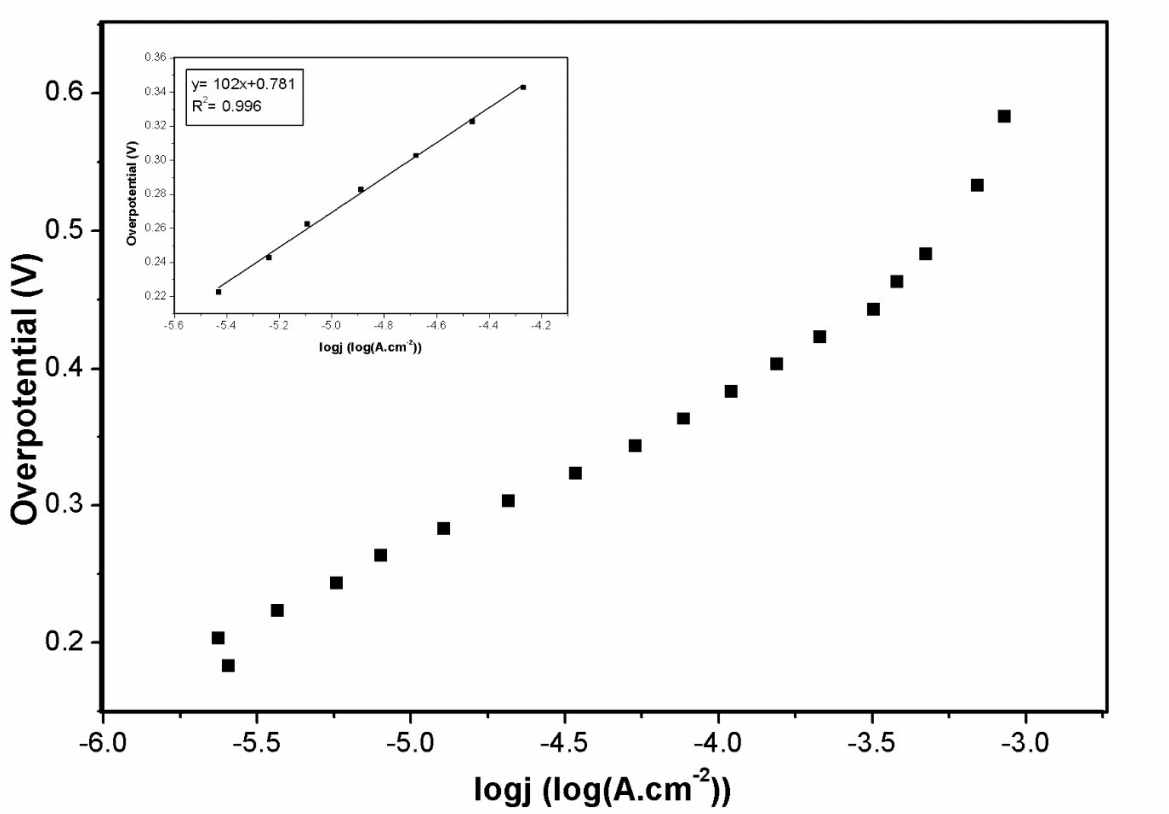

Figure 4. 8. Tafel plot for Co[Fe(CN)$_5$-HPPB] from 1 V to 1.4 V vs NHE. Inset shows the linearity between overpotential and current density from 1.22 V to 1.34 V.

The linearity obtained in intermediate potentials (220-360 mV) with a Tafel slope of 102 mV dec^{-1} for Co[Fe(CN)$_5$-HPPB]. Tafel slope is obtained for Co[Fe(CN)$_5$-HPPB] compared to PBAs in

chapter 3, the current density values show a noteworthy progress. 1 mA/cm^2 of catalytic current density for was achieved at η = 421 mV.

The observed deviation from linearity can be attributed to the oxygen bubbles that are formed on the FTO electrode limits the mass transport.

By using the electro active surface coverage value, the minimum turnover frequency (TOF) value was calculated as 0.0414 s^{-1} at an overpotential of 400 mV according to equation 3.2.

MHCMs studied in Chapter 3, TOFs at an overpotential of 400 mV were obtained as 5.0×10^{-2} s^{-1}, 3.0×10^{-3} s^{-1}, 4.4×10^{-3} s^{-1}, and 5.0×10^{-3} s^{-1} for [Co^{II}-Co^{III}], [Co^{II}-Fe^{II}], [Co^{II}-Fe^{III}], and [Co^{II}-Cr^{III}] respectively. When the TOF of Co[$Fe(CN)_5$-HPPB] compared with these MHCMs, it can be seen that, Co[$Fe(CN)_5$HPPB] has higher TOF value than [Co^{II}-Fe^{II}], [Co^{II}-Fe^{III}], and [Co^{II}-Cr^{III}] PBAs, however lower than [Co^{II}-Co^{III}]. A comparison of TOFs shows that Co(II) sites available in [Co^{II}-Co^{III}] exhibit the higher the catalytic activity than Co(II) sites in Co[$Fe(CN)_5$HPPB].

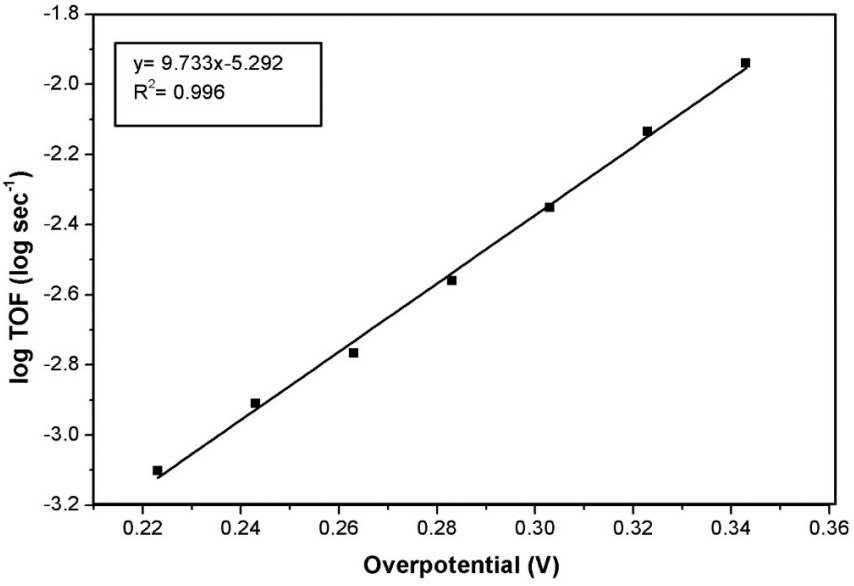

Figure 4. 9. Dependence of turnover frequency of Co[$Fe(CN)_5$-HPPB] derivatives in 1.0 V to 1.4 V vs. NHE range.

CHAPTER 5

RESULTS AND DISCUSSION FOR METAL HEXACYANOMETALATES (MHCMs) as WATER REDUCTION CATALYSTS

5.1. CHARACTERIZATIONS OF METAL HEXACYANOMETALATES

Two metal hexacyanometalates with molecular formulas $K_xM_y[Co(CN)_6]_2$ M: Co^{II},Zn^{II} (will be abbreviated as Co-Co and Zn-Co throughout the chapter) have been studied as water reduction catalysts. Characterizations of the bulk catalysts have been performed by X- Ray Diffraction, Fourier Transform Infrared Spectroscopy, and Electron Dispersive X-ray spectroscopy techniques.

5.1.1. Powder X-Ray Diffraction Studies

The powder XRD patterns (Figure 5.1) of Co-Co & Zn-Co PBA crystallites correspond well with the previously reported PBAs. All the peaks indexed by comparing to the reported PBAs confirm face-centered cubic unit cell assuming a Fm3m space group (JCPDS Card No: 73-0687).[46], [80]

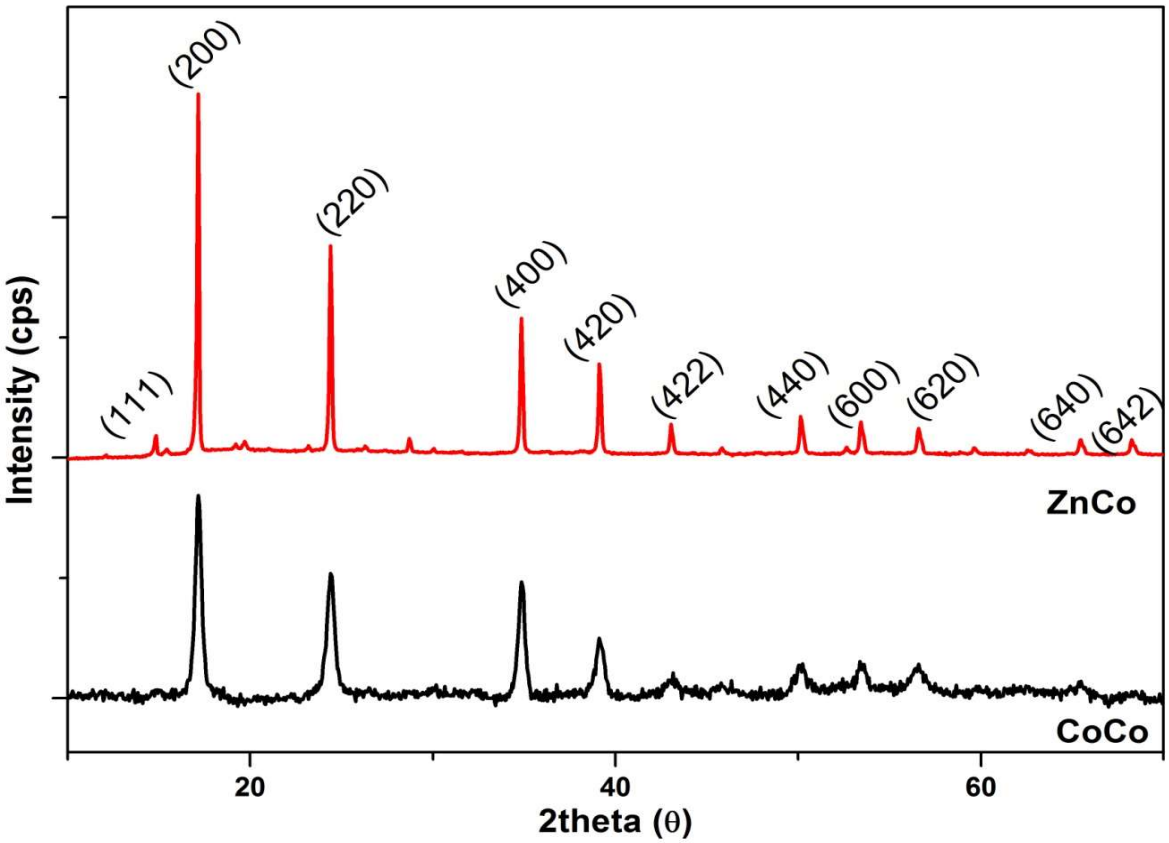

Figure 5. 1. X-ray diffraction patterns of bulk Co-Co and Zn-Co PBA

5.1.2. Infrared Studies

Infrared studies performed on the as synthesized Co-Co PBA reveal strong bands at 2169, 444, and 1607 cm^{-1} corresponding to the vibrational stretches ν(CN), ν(Co^{II}-CN-Co^{III}), and bending stretch δ(H-O-H), respectively. Similarly, ATR spectrum of Zn-Co PBA reveals strong bands at 2171, 440, and 1609 cm^{-1} corresponding to the vibrational stretches ν (CN), ν (Zn^{II}-CN-Co^{III}), and bending stretch δ(H-O-H), respectively. FTIR spectra of Co-Co and Zn-Co species are shown in Figure 5.2.

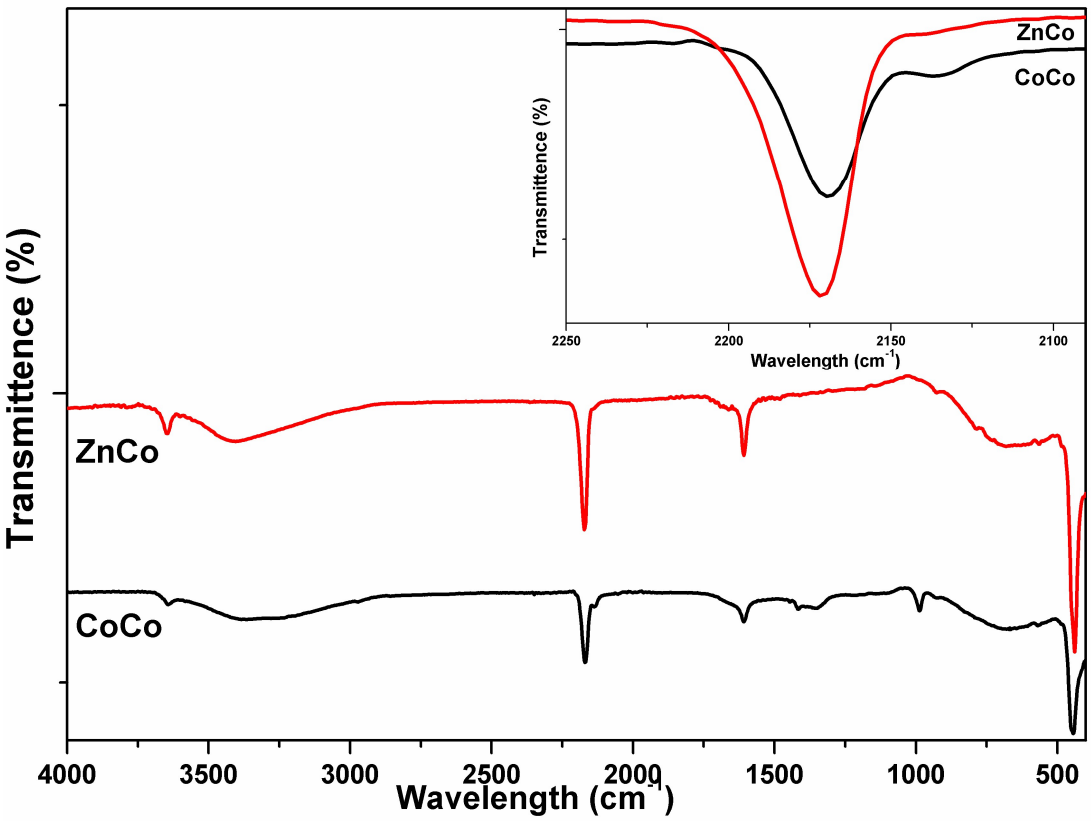

Figure 5. 2. FTIR spectra of bulk Co-Co and Zn-Co PBA.

5.1.3. Scanning Electron Microscopy and Energy Disperse X- Ray Analysis

SEM and EDX analyses were performed to probe the compositions and morphologies of samples. Powder samples have uniform particle sizes in the μm range SEM images of Co-Co and Zn-Co PBAs are shown in Figure 5.3.

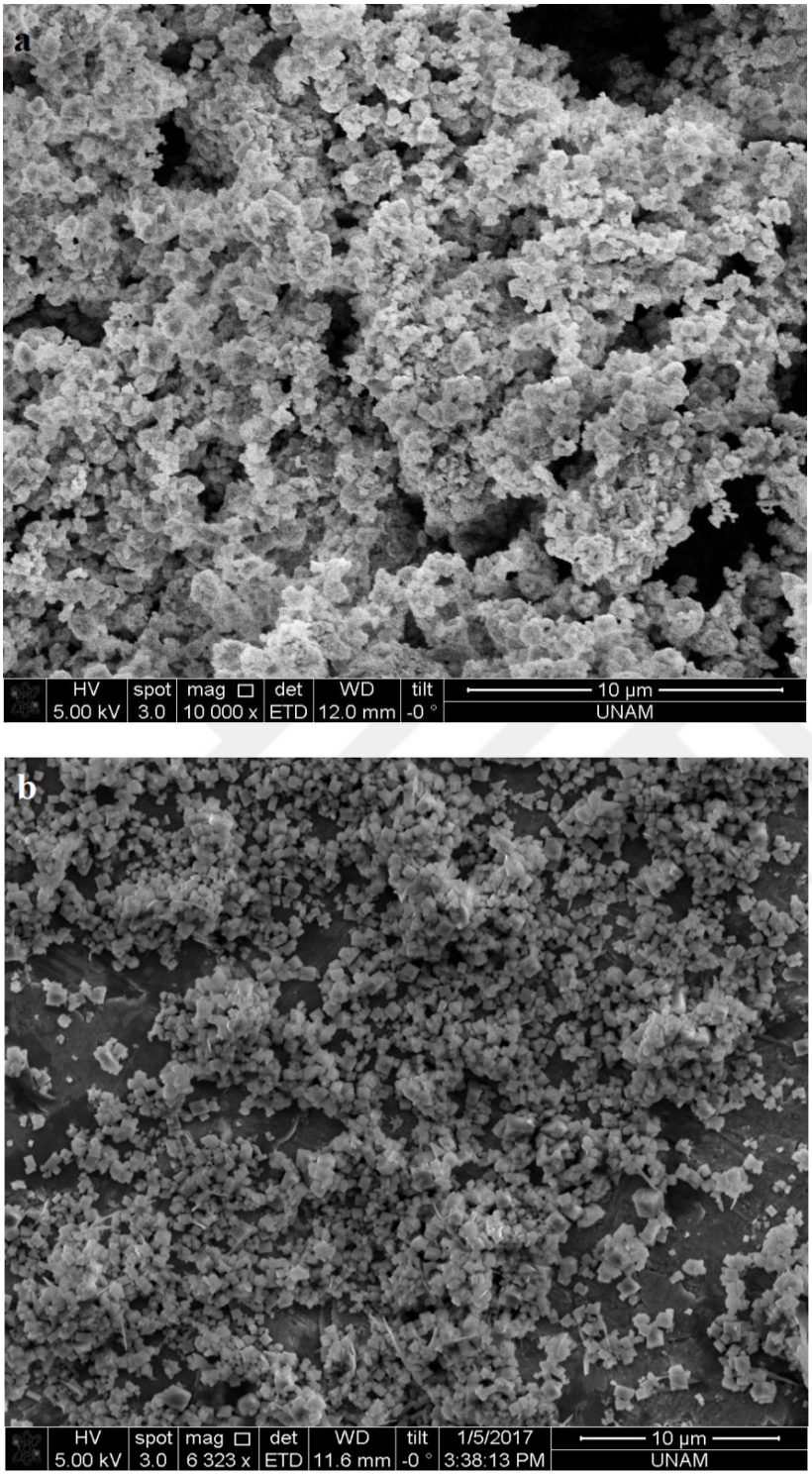

Figure 5. 3. SEM images of a) Co-Co PBA and b) Zn-Co PBA bulk samples showed uniform particles

Molecular formulae of PBAs were determined as $K_{0.76}Co_{2.62}[Co(CN)_6]_2$ and $K_{0.72}Zn_{2.64}[Co(CN)_6]_2$ for Co-Co and Zn-Co derivatives, respectively, based on EDX analysis. EDX spectra of Co-Co and Zn-Co PBAs are shown in Figure 5.4.

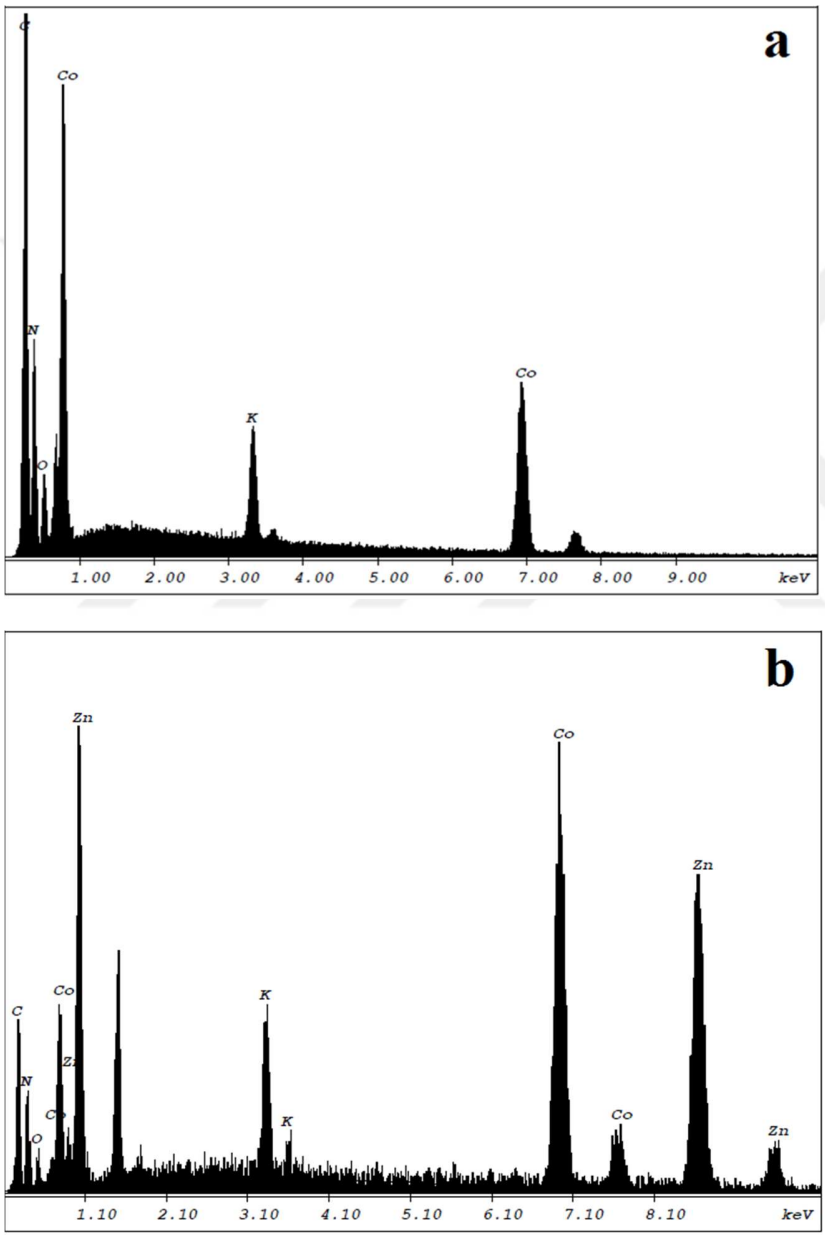

Figure 5. 4. EDX spectra of a) Co-Co PBA and b) Zn-Co PBA.

5.2. ELECTROCHEMICAL WATER OXIDATION STUDIES OF METAL HEXACYANOMETALATES

5.2.1. Linear Sweep Voltammetry Studies

Linear sweep voltammetry (LSV) curves were recorded in a 50 mM KPi buffer solution with 1 M KNO_3 as electrolyte at pH 7.0 with a sweep rate of 5 mV. s^{-1}. LSVs of Zn-Co PBA, [$CoCo(CN)_6$@FTO], as shown in Fig. 2, exhibits a significant HER activity with an onset overpotential of 257 mV(E^o= -413 mV and E_{onset}= 875 mV vs. Ag/AgCl) , which is extracted from the beginning of linear regime in the Tafel plot. LSV of [$ZnCo(CN)_6$@FTO] and that of bare electrode are identical indicating that the origin of HER activity in [$CoCo(CN)_6$@FTO] is only due to Co^{II} sites surrounded with nitrogen atoms (CoN_6) of nitrile group and that Co^{III} centers in hexacyanocobaltate units do not participate in catalytic water reduction process.

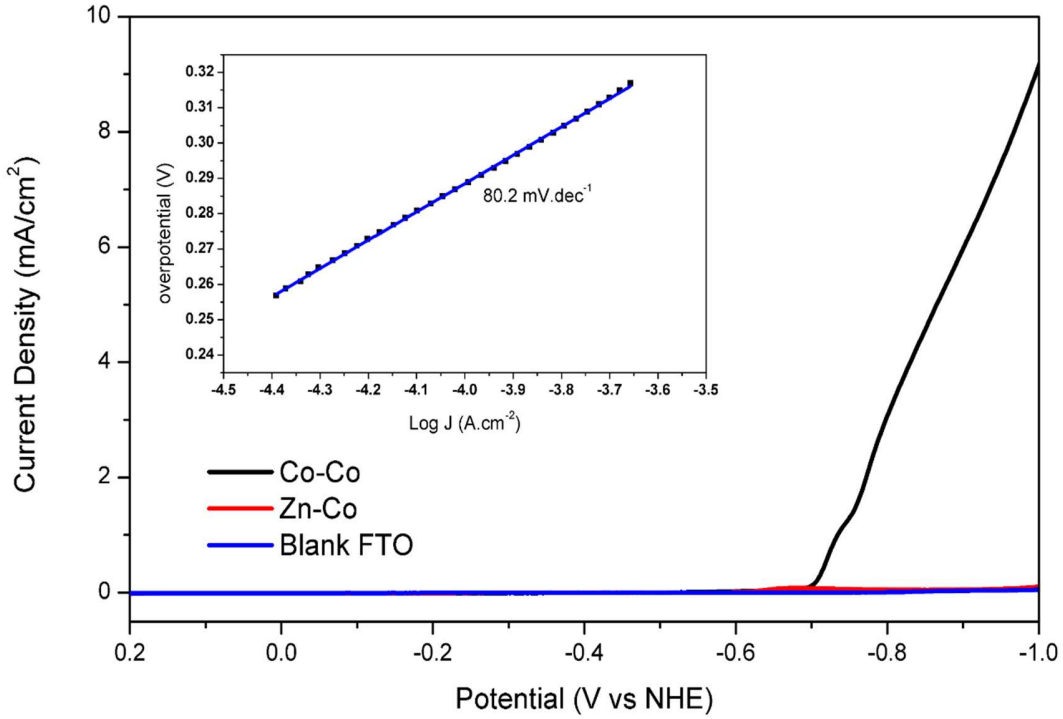

Figure 5. 5. LSV curves of [$CoCo(CN)_6$@FTO], [$ZnCo(CN)_6$@FTO], and blank FTO electrodes

Inset: Tafel plot for [$CoCo(CN)_6$@FTO] derived from the LSV curve (black line) and linear fitting curve (blue dotted).

Tafel plot of the catalyst, which was obtained from the LSV curve of [$CoCo(CN)_6$@FTO] at a scan rate of 5 $mV.sec^{-1}$, was used to extract two important electrochemical parameters;

i) Tafel slope (b) and

ii) exchange current density (i_0).

Tafel slope, as shown in Fig. 5.5 Inset, was used for the specification of the overpotential required to raise the current density by one order of magnitude[116] and the prediction of mechanism for catalytic process. Tafel slope determined as 80.2 $mV.dec^{-1}$, was similar to the reported values for cobalt-sulfide film (Co−S/FTO) (93 $mV.dec^{-1}$),[117] and Co–P/CC NWs array (93 $mV.dec^{-1}$)[118]. This value was also found to be slightly higher than the ones reported for FeP/CC (70 $mV.dec^{-1}$),[119] $Ni_{0.33}Co_{0.67}S_2$ (67.8 $mV.dec^{-1}$),[120] Co–P/Ti (58 $mV.dec^{-1}$),[121] and Co-30Ni–B (51 $mV.dec^{-1}$)[116] at neutral conditions. From the Tafel plot a 2 step mechanism for HER was predicted to be initiated by proton discharge step (Volmer step, 120 $mV.dec^{-1}$) followed by electrochemical desorption (Heyrovsky step, 40 $mV.dec^{-1}$) or chemical desorption (Tafel step, 30 $mV.dec^{-1}$). A value of 80.2 $mV.dec^{-1}$ for [$CoCo(CN)_6$@FTO] suggests Volmer-Heyrovsky reaction mechanism as expected for heterogeneous catalysts.[116], [122], [123].

Exchange current density (j_0) could also be determined at an overpotential of 0 V from Tafel analysis. The exchange current density for [$CoCo(CN)_6$@FTO] in pH 7 was calculated to be 2.55×10^{-8} $A.cm^{-2}$, which was similar with 2×10^{-8} $A.cm^{-2}_{geom}$ for electropolymerized Co(II)

dibenzotetraaza(14) annulene system (CoTAA),[124] 5.9×10^{-8} A.cm^{-2} for $CoSe_2$ films,[125] and 8.2×10^{-8} A.cm^{-2} for MoO_3-MoS_2/FTO electrode.[126]

5.2.2. Chronopotentiometry Studies

Since the stability of the catalyst is essential particularly for practical applications, chronopotentiometry measurement was performed for [$CoCo(CN)_6$@FTO] at a constant current density of 1 mA.cm^{-2} for two hours. The performance of [$CoCo(CN)_6$@FTO] for hydrogen evolution showed very good durability for two hours with an overpotential of 295 mV. No significant increase of the overpotential under this condition was observed, suggesting the stability of the catalyst throughout the experiment as shown in Figure 5.6. Furthermore, the similarity of LSV curve of the pristine catalyst and that of the catalyst after 2h of chronopotentiometry experiment supports the aforementioned claim on the superior stability of the modified electrode, as shown in Figure 5.6 inset.

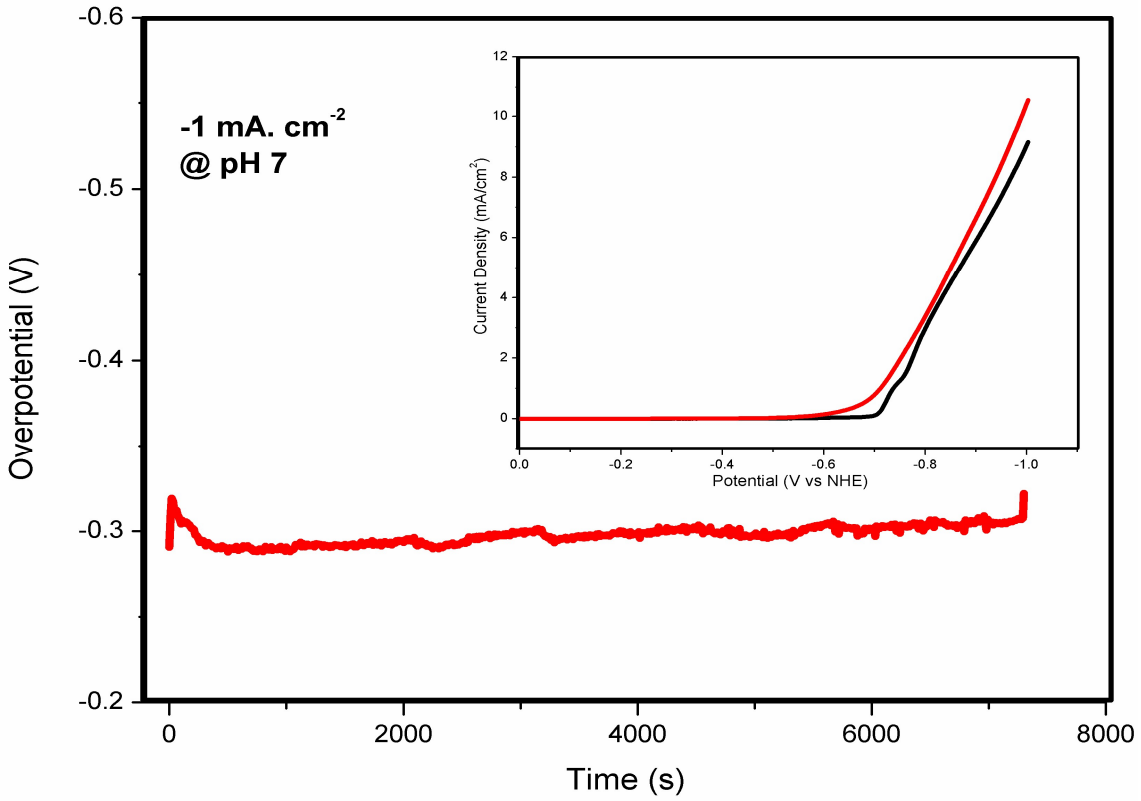

Figure 5. 6. Chronopotentiometry curve obtained for [CoCo(CN)$_6$@FTO] at 1 mA.cm^{-2}. Inset shows the LSV comparison between the pristine (black) and post-catalytic (red) electrodes with a scan rate 5 mV. s^{-1}

5.2.3. Long Term Stability Measurements

Chronoamperometric analysis was performed at -0.8 V (vs NHE) using [CoCo(CN)$_6$@FTO] for three days in 50 mM KPi solution with 1 M KNO_3 (pH 7.0), with intervals of 24 h Figure 5.7 shows the chronoamperometric study of Co-Co PB on FTO electrode. Black arrows in Figure 5.7 indicate the termination of electrolysis. Upon further continuation of the electrolysis, current density decreases until it reaches stabilization at around 0.6 mA.cm^{-2} after 24 h. The same current density observed at the end of each electrolysis steps implies stable performance of [CoCo(CN)$_6$@FTO] during electrolysis and no degradation of the FTO electrode

surface.

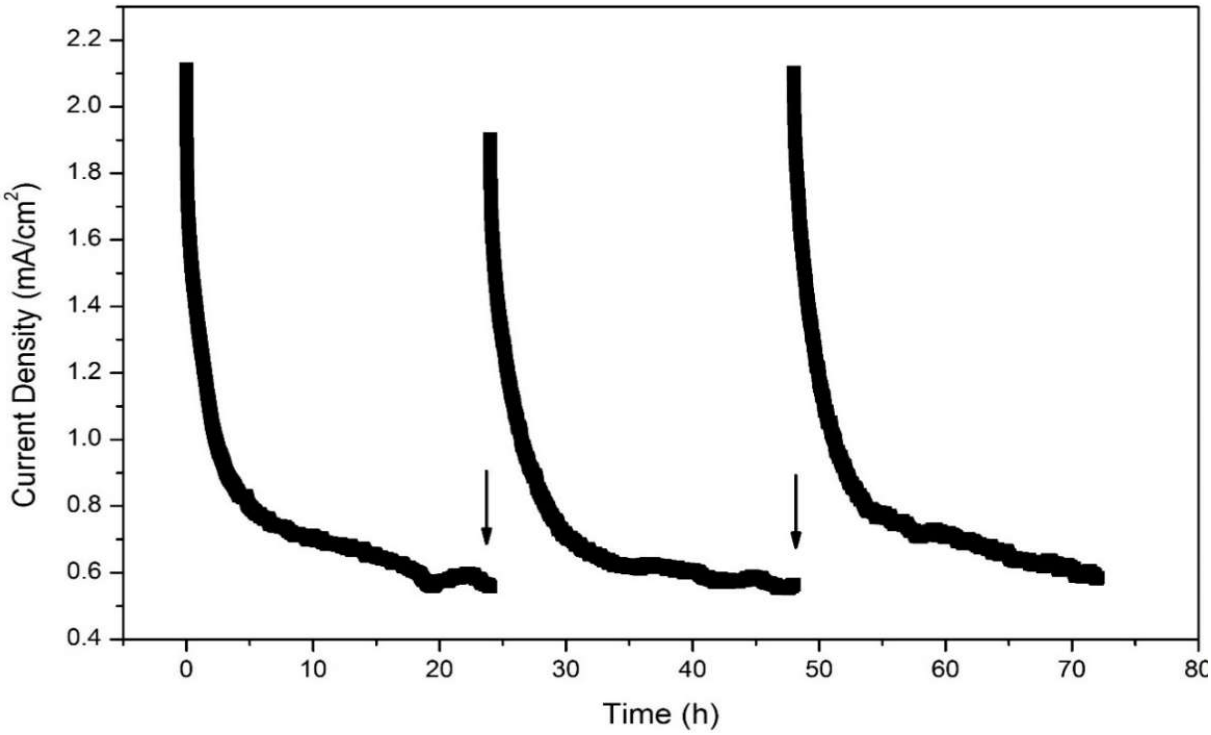

Figure 5. 7. Current profile of long-term electrolysis performed for 3 days at −0.8 V (vs.NHE) at pH 7.0 of a [$CoCo(CN)_6$@FTO]. Black arrow indicates the termination of electrolysis.

5.2.4. Chronocoulometry Measurements

The charge accumulated over time is measured in a controlled potential electrolysis at −0.8 V (vs NHE) in the absence and presence of Co-Co PBA on FTO electrode in 50 mM KPi buffer solution with 1 M KNO_3 as an electrolyte at pH 7.0. The catalyst affords a robust and essentially linear charge build-up over time with no significant loss in activity over the course of at least 2 h. In contrast, negligible charge was passed when a blank FTO electrode was used as the working electrode under the same conditions.

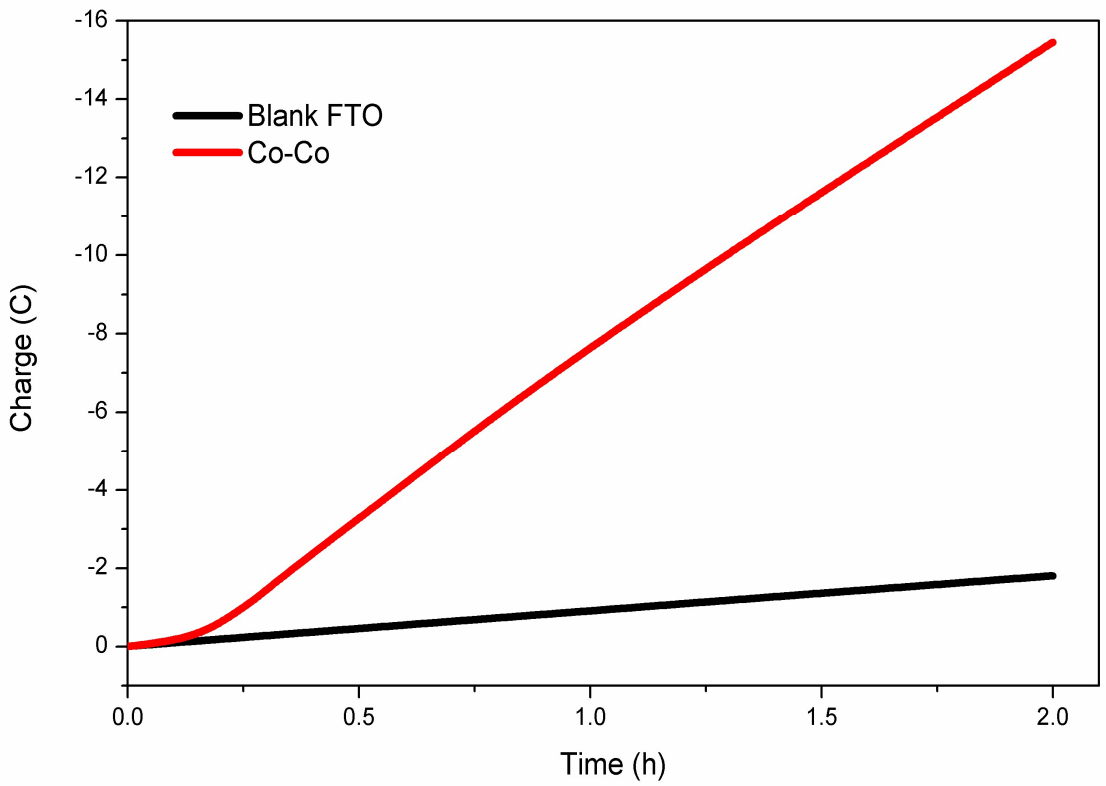

Figure 5. 8. Charge accumulated over time in a controlled potential electrolysis at −0.8 V vs. NHE in the absence (black line) and presence of Co-Co PBA on FTO electrode (red line)

5.2.5. Surface Coverage and Turnover Frequency Studies

Cyclic voltammogram (CV) at different scan rates was recorded in the range of 0.7 – 1.2 V vs NHE to determine the coverage of redox-active Co centers on the electrode. The cyclic voltammograms are shown in Figure 5.9.

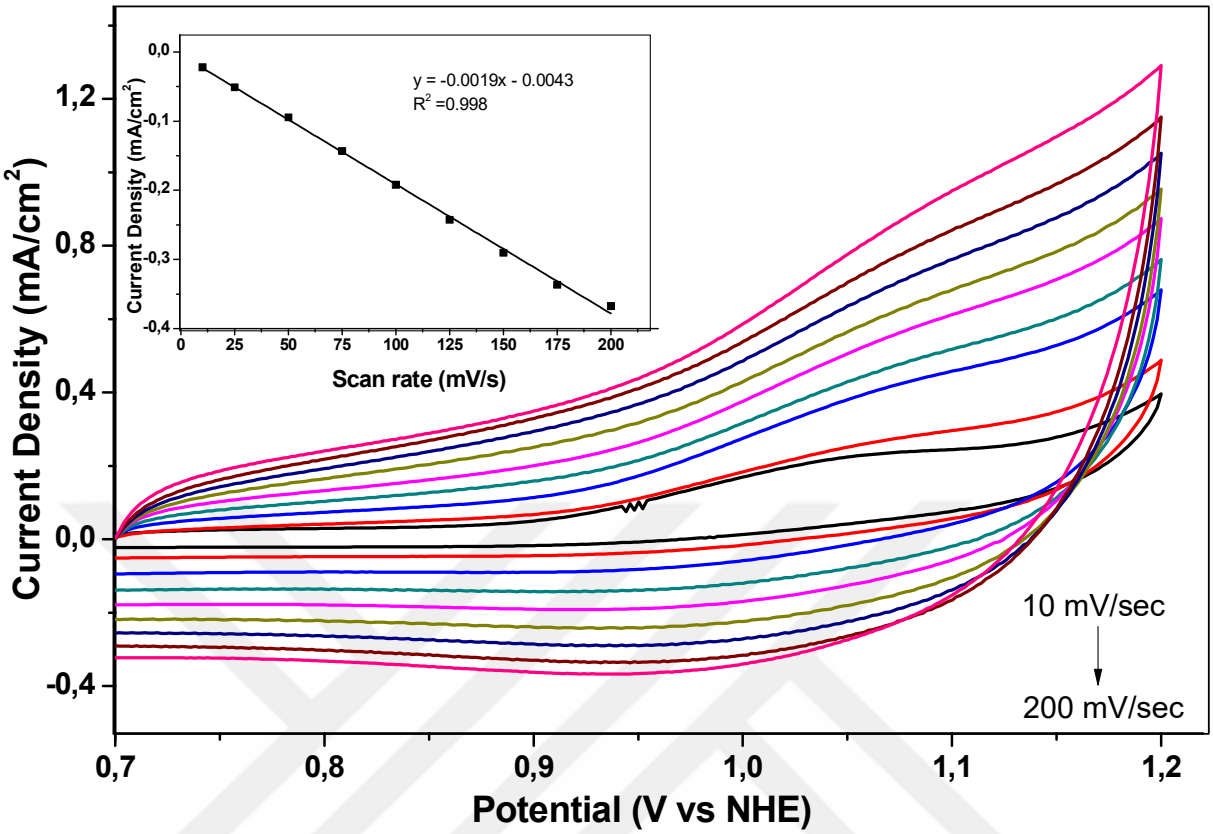

Figure 5. 9. Cyclic voltammograms of [$CoCo(CN)_6$@FTO] electrode recorded at different scan rates (10 - 200 mV sec^{-1}). The inset displays linear dependence of the peak current of the Co^{3+}/Co^{2+} reduction peak vs. scan rate.

The surface concentration, calculated to be 2.0 nmol.cm^{-2} by using equation 3.1, was used to determine the turnover frequency (TOF) for [$CoCo(CN)_6$@FTO]. A TOF value of 0.090 s^{-1} was calculated from Tafel plot at an overpotential of 250 mV, which is higher than that reported for Co-cat (0.022 s^{-1} at 385 mV)[127] and Co–S film (0.017 s^{-1})[117] at pH 7.0. The comparison of TOF for different systems suggests that cobalt sites surrounded with nitrogen atoms exhibit superior catalytic performance compared to the ones surrounded with oxygen and/or sulfur atoms.

5.2.6. Faradaic Efficiency Measurements

Controlled potential electrolysis (CPE) experiment was performed to calculate faradaic efficiency. Protons consumed during H_2 evolution results in the formation of hydroxide anions increasing the pH of the medium. Thus, monitoring this increase of pH during electrolysis, can be used to quantify the faradaic efficiency of a HER catalyst.[124] The charge measured during electrolysis can also be used to calculate the theoretical amount of evolved H_2. Figure 5.10 shows accumulated charge over time during a 60 min CPE experiment at −0.9 V vs NHE using 10 mL 1 M KCl solution. The excellent agreement between calculated and observed pH changes during experiment clearly indicates that the only origin of catalytic current is H_2 evolution.

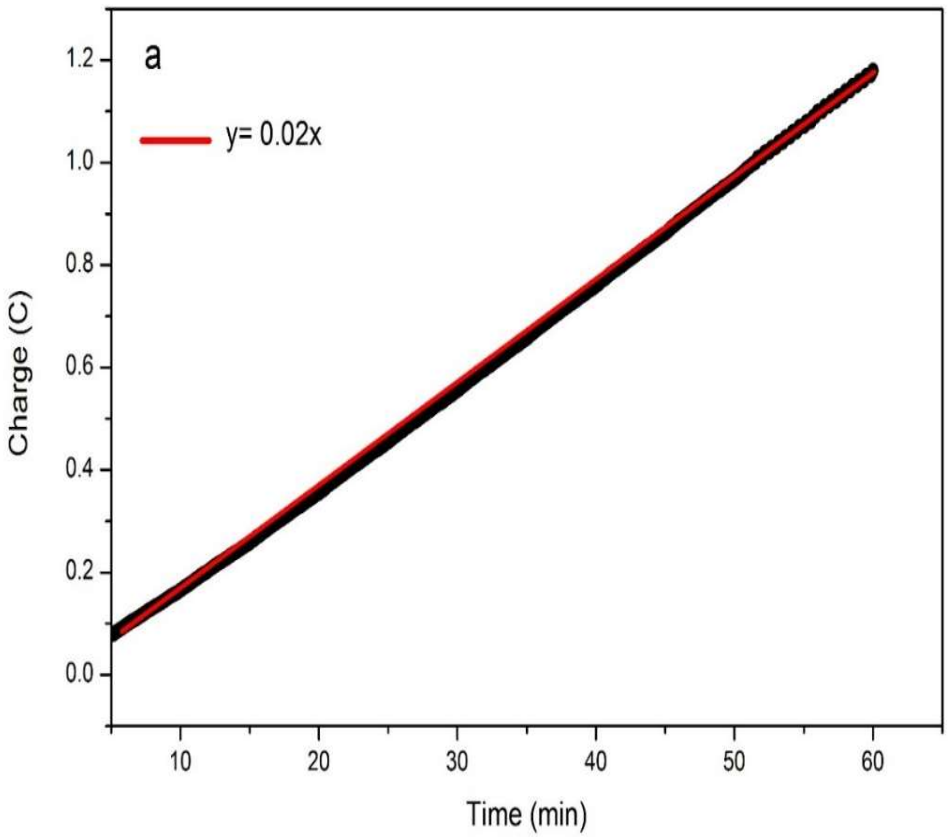

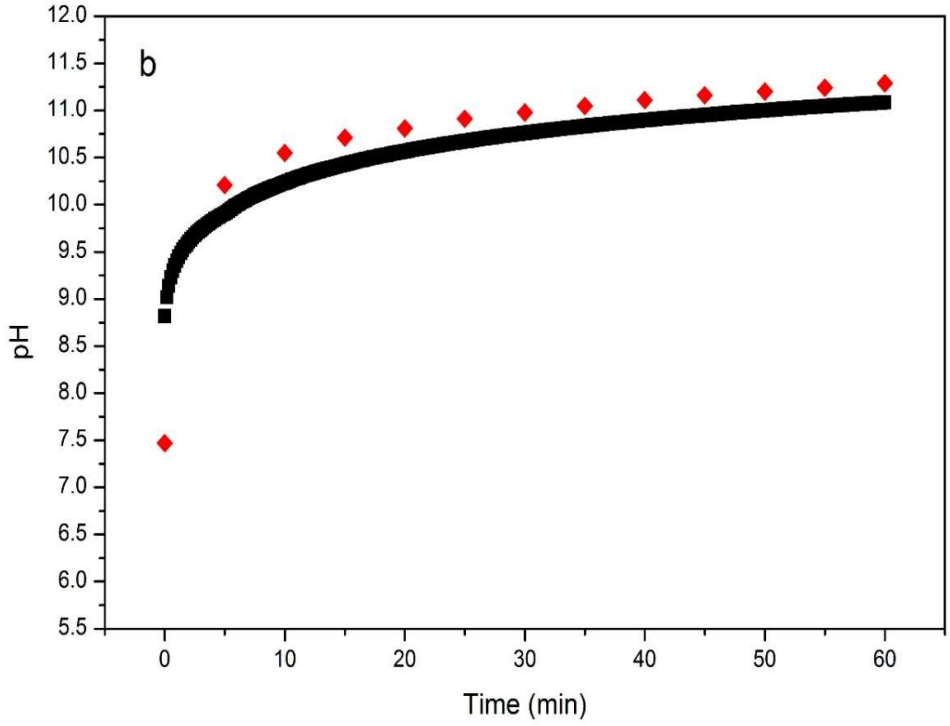

Figure 5. 10. Electrochemical data of Co-Co coated FTO electrode in 1 M KCl for 60 min. a) Charge accumulated over time in a controlled potential electrolysis at −0.9 V (vs.NHE). Linearity is shown in red line b) measured pH change with time during the electrolysis (red diamonds) and the calculated pH change over a ten-minute interval (black squares).

5.3. CHARACTERIZATION OF THE ELECTRODES

Co-Co and Zn-Co PBAs have been studied as water reduction catalysts. Characterization studies of the catalysts on electrodes have been performed by Grazing Incidence X- Ray Diffraction and X-ray Photoelectron Spectroscopy techniques.

5.3.1. Grazing Incidence X-Ray Diffraction Studies of [$CoCo(CN)_6$@FTO]

GI-XRD (grazing incidence) analysis was also performed on [$CoCo(CN)_6$@FTO] to

investigate the change in crystallinity during electrolysis. No distinguishable change was observed between the pristine and post-catalytic electrodes in the patterns as shown in Figure 5.11, which indicates that the structure and the composition of the Co-Co PBA is not affected by the partial reduction of cobalt sites. Therefore, it can be assumed that the partial reduction in the cobalt sites is reversible.

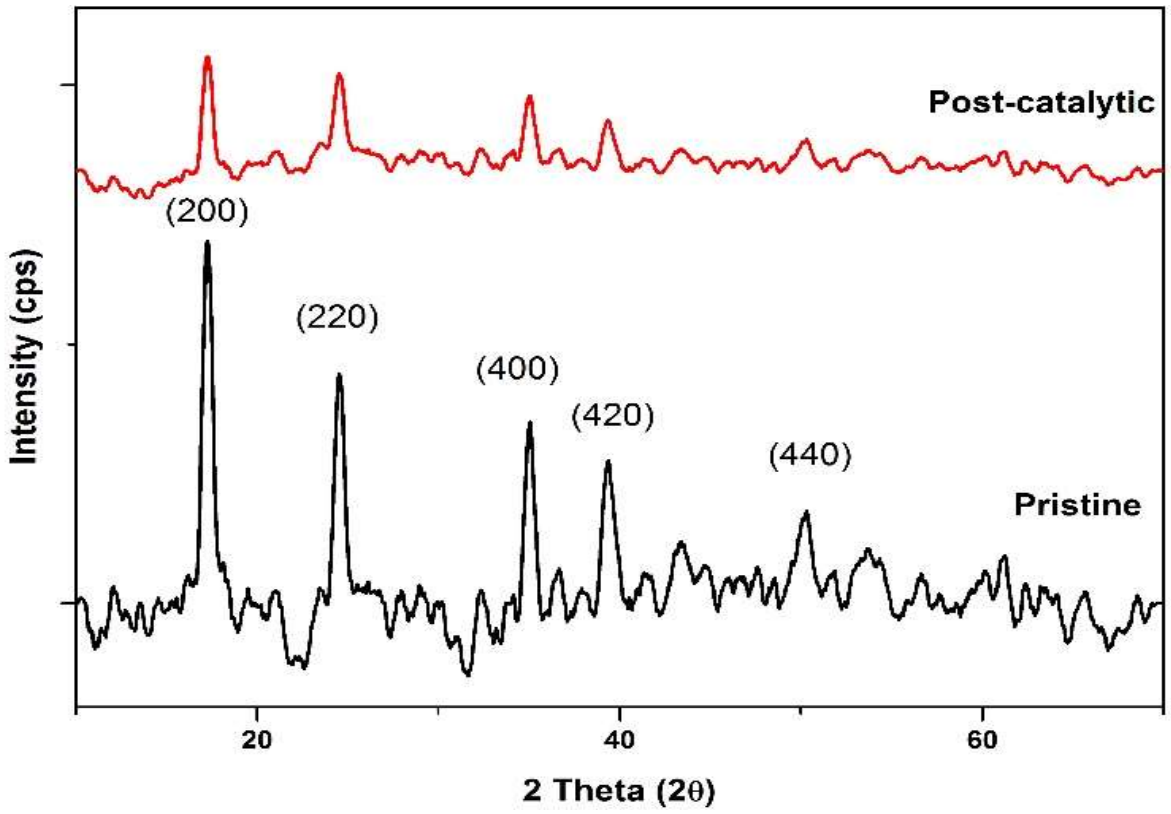

Figure 5. 11. Thin film XRD for pristine and post-catalytic [$CoCo(CN)_6$@FTO] electrodes.

5.3.2. X-Ray Photoelectron Spectroscopy Studies

XPS studies performed on the [$CoCo(CN)_6$@FTO] before (pristine) and after (post-catalytic) bulk electrolysis at −0.8 V (vs NHE) are shown in Figure 5.12.a. The Co2p spectrum of pristine Co-Co PBA shows sharp and distinctive principle $Co2p_{3/2}$ and $Co2p_{1/2}$ signals,

respectively, at 784.38 eV and 799.48 eV [47], [81]with scalable FWHM of ~2 eV while the post-catalytic electrode shows broad principle $Co2p_{3/2}$ and $Co2p_{1/2}$ signals at 782 eV and 797.68 eV, respectively, with relatively wider FWHM of ~3 eV. Furthermore, weak but identifiable satellite signals at 788.38 eV and 803.98 eV were observed for the post-catalytic electrode corresponding to $Co2p_{3/2}$ and $Co2p_{1/2}$, respectively. The appearance of identifiable satellite signals in the post-catalytic electrode suggests partial reduction of the cobalt sites.

The pristine Zn-Co PBA shows sharp, distinctive principle $Co2p_{3/2}$ signal at 786.08 eV and $Co2p_{1/2}$ signal at 801.08 eV, with scalable FWHM of ~3.5 eV. Where in the post-catalytic ZnCo shows sharp principle $Co2p_{3/2}$ signal at 784.68 eV and $Co2p_{1/2}$ signal at 799.48 eV with a FWHM of ~3 eV. The pristine Zn-Co PBA shows sharp, intense principle $Zn2p_{3/2}$ signal at 1025.88 eV and $Zn2p_{1/2}$ signal at 1048.98 eV with a FWHM of ~3 eV. The post-catalytic Zn-Co PBA shows broad but intense principle $Zn2p_{3/2}$ signal at 1024.18 eV and $Zn2p_{1/2}$ signal at 1047.08 eV with a FWHM of ~1.8 eV. The absence of any additional satellite signals in both Co2p and Zn2p lines of the Zn-Co PBA electrodes confirms that there is no change in the oxidation states suggesting the absence of electrochemical activity. XPS studies for Zn2p satellites are shown in Figure 5.12.b.

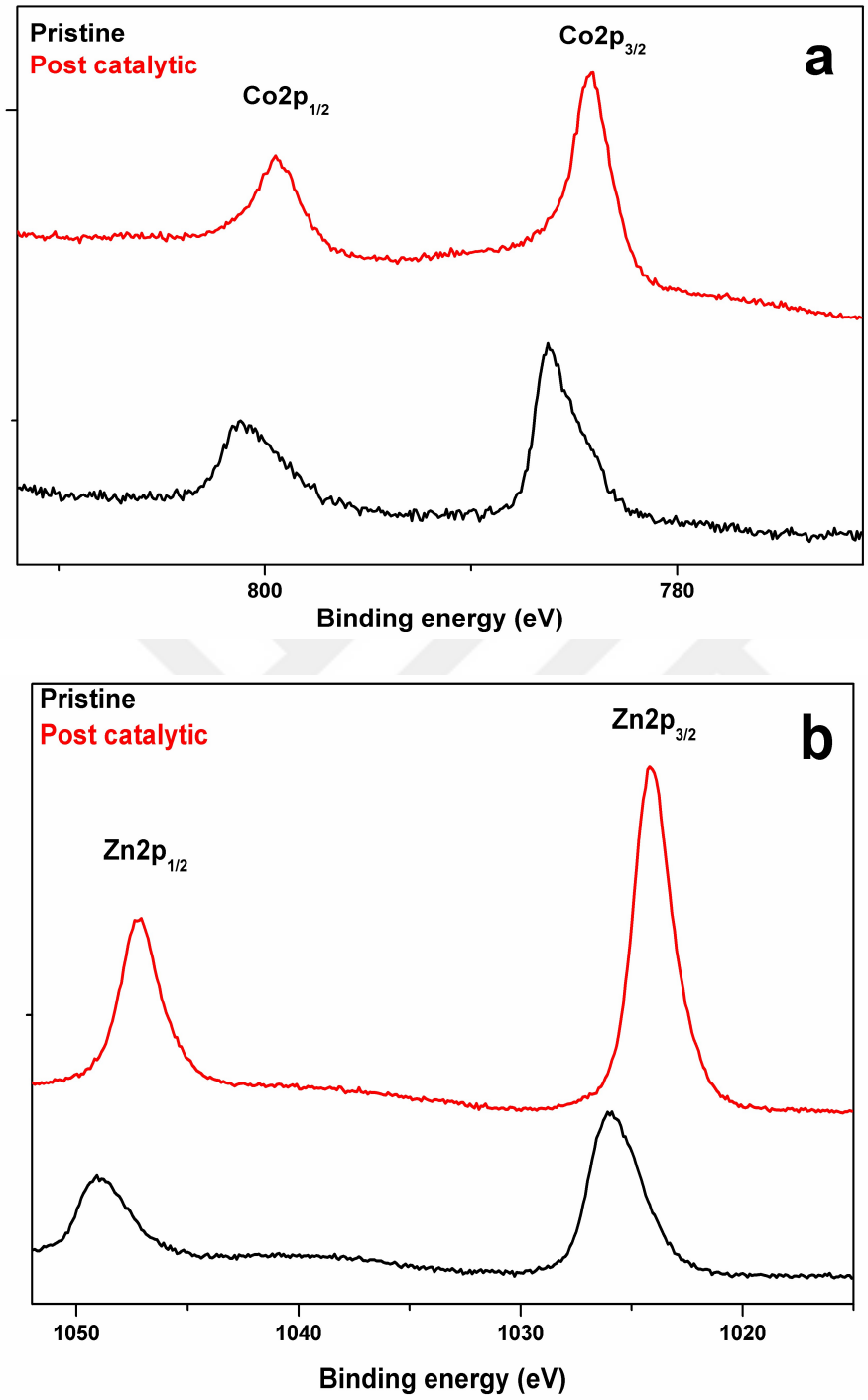

Figure 5. 12. XPS spectra of a) Co2p signals and b) Zn2p signals of Zn-Co PBA.

CHAPTER 6

CONCLUSION

In this thesis, various kinds of Prussian blue Analogues with different metals and ligands are synthesized to show their electrocatalytic water oxidation and water reduction capabilities. These studies are presented in three main themes:

Firstly, previous electrochemical studies on Prussian blue analogues have shown that having a cobalt site coordinated to nitrogen atoms of cyanide bridging group is essential to obtain efficient PBA electrocatalysts for water oxidation. In this part, a series of cobalt hexacyanometalates with a general formula of $K_aCo_b[Fe(CN)_6]$ have been prepared to investigate the effect of hexacyanometal group to the electrocatalytic activity of CHCMs. Tafel analysis and chronoamperometry experiments reveal that [Co^{II}-Co^{III}] serves as the most efficient electrocatalyst for water oxidation among the CHCMs studied. Infrared and XPS studies indicate that it has the Co(II) center with the lowest electron density. Overall, studies lead to the following conclusions:

i) Electron density of Co^{2+} is a decisive electronic criterion for achieving efficient water oxidation electrocatalysis and this parameter could be tuned by changing the type of hexacyanometal group.

ii) The electron density of Co(II) can be reduced by increasing the oxidation state of the metal ion of $[M(CN)_6]^{n-}$ group.

iii) Nucleophilic attack of water to the cobalt-oxo intermediate should be the rate determining step for water oxidation catalysis with Prussian blue analogues.

Secondly, a quite new synthesis route was practiced synthesizing a new Prussian blue Analogue as water oxidation electrocatalyst. Cyanide ligand in hexacyano ferrate complex has been substituted with an N- donor ligand which is 1-heptyl 4-(4 pyridyl) pyridinium bromide. This

ligand helps to prepare an amorphous Prussian blue analogue. With this system, the active cobalt sites are increased. According to surface concentration analysis of the cobalt sites on the electrode is increased at least two-fold. This amorphous nature has positive impact on the catalytic activity when compared to cobalt hexacyanoferrates. A current density of 1 $mA.cm^{-2}$ was achieved at the 421 mV overpotential. This value is much lower than cobalt hexacyano ferrate species (661 mV and 692 mV overpotentials for [Co^{II}-Fe^{III}] and [Co^{II}-Fe^{II}] respectively). Tafel slope was also diminished to 102 $mV.dec^{-1}$ from approximately 120 $mV.dec^{-1}$ for cobalt hexacyanoferrates. For 400 mV overpotential, a turnover frequency value of 0.0414 s^{-1} could be achieved with this path. This study is a subsequent investigation of our group. In the previous study, cobalt- P4VP coordinated- pentacyano ferrate was used as a water oxidation electrocatalyst. These two studies enable to see that new and efficient catalysts, which are stable and easy to synthesize could be presented as water oxidation catalyst with the help of well-known and miscellaneous pentacyanometalate chemistry.

Finally, a wide range of cobalt containing three-dimensional compounds including oxides, sulfides, phosphides, and borides have recently been investigated as water reduction catalysts. While these studies assist researchers in the optimization of the coordination environment of cobalt center for higher catalytic activity and higher stability, it is clear that new systems should be introduced to the field to expand the portfolio of cobalt-based electrocatalysts with convenient anionic groups. It should also be noted that such a catalyst should have a straight-forward synthesis that allows easy modification and superior robustness in a wide range of pH and at high cathodic potentials. PBAs with their unique structural motives wherein metal ions are connected to each other with cyanide groups meet all of the aforementioned requirements. Where in this study, demonstrated for the first time that a Co-Co Prussian blue analogue can be used as an efficient

water reduction catalyst as well. Comparative electrochemical studies indicate that catalytic activity of Prussian blue analogue is due to the cobalt(II) ions surrounded by the nitrogen atoms of nitrile group. Co-Co Prussian blue modified FTO electrode exhibits a significant HER activity with an onset overpotential of 257 mV. The Tafel slope obtained from cyclic voltammetry of the electrode (80.2 $mV.dec^{-1}$) is in good accordance with the previously studied cobalt-based heterogeneous systems, which suggests a mechanism involving the formation of a metal-hydride intermediate followed by reaction of hydride and the proton of water resulting in H_2 evolution. The catalyst performs at a much higher turnover frequency (0.090 s^{-1} at an overpotential 250 mV) compared to other cobalt-based systems. Long-term electrolysis studies together with comprehensive characterization studies confirm that the catalyst retains its structure throughout the catalytic process.

BIBLIOGRAPHY

[1] K. R. Dunbar and R. a Heintz, “Chemistry of Transition Metal Cyanide Compounds: Modern Perspectives,” in *Progress in Inorganic Chemistry*, vol. 45, 1997, pp. 283–391.

[2] W. P. Griffith and G. T. Turner, “Raman spectra and vibrational assignments of hexacyano-complexes,” *J. Chem. Soc. A Inorganic, Phys. Theor.*, vol. 0, no. 0, pp. 858–862, Jan. 1970.

[3] M. F. Amr El-Sayed and R. K. Sheline, “The position of the CN stretching frequency in organic and inorganic molecules,” *J. Inorg. Nucl. Chem.*, vol. 6, no. 3, pp. 187–193, Jun. 1958.

[4] T. P. Hanusa, “Cyanide Complexes of the Transition Metals,” in *Encyclopedia of Inorganic Chemistry*, Chichester, UK: John Wiley & Sons, Ltd, 2006, pp. 1–11.

[5] W. P. Griffith, “Cyanide Complexes of Transition Metals,” *Q. Rev.*, vol. 16, pp. 188–207, 1962.

[6] M. Shatruk, C. Avendano, and K. R. Dunbar, “Cyanide-Bridged Complexes of Transition Metals: A Molecular Magnetism Perspective,” *Prog. Inorg. Chem.*, vol. 56, pp. 155–334, 2009.

[7] K. Nakamoto, *Infrared and Raman Spectra of Inorganic and Coordination Compounds Part B: Applications in Coordination, Organometallic, and Bioinorganic Chemistry*, 6th ed. John Wiley & Sons, Inc., 2009.

[8] D. F. Shriver, S. A. Shriver, and S. E. Anderson, “Ligand Field Strength of the Nitrogen End of Cyanide and Structures of Cubic Cyanide Polymers,” *Inorg. Chem.*, vol. 4, no. 5, pp. 725–730, May 1965.

[9] B. I. Swanson and J. J. Rafalko, “Perturbation of intramolecular vibrations by strong interionic forces. Vibrational spectra and assignments for hexacyanoferrate(4-) ion and cesium magnesium hexacyanoferrate ($Cs_2MgFe(CN)_6$),” *Inorg. Chem.*, vol. 15, no. 2, pp. 249–253, Feb. 1976.

[10] B. I. Swanson, “Aspects of the structure and bonding in Prussian Blues. Single-crystal Raman study of trimanganese hexacyanocobaltate hydrate ($Mn_3[Co(CN)_6].xH_2O$) and tricadmium bis(hexacyanocobaltate) hydrate ($Cd_3[Co(CN)_6]2.xH_2O$),” *Inorg. Chem.*, vol. 15, no. 2, pp. 253–259, Feb. 1976.

[11] S. J. Carter, B. M. Foxman, and L. S. Stuhl, “Cobalt(II) cyanides in aprotic media: effect of varying counterion and solvent,” *Inorg. Chem.*, vol. 25, no. 16, pp. 2888–2894, Jul. 1986.

[12] A. Kraft, “On The Discovery and History Of Prussian Blue,” *Bull. Hist. Chem*, vol. 33, no. 2, pp. 61–67, 2008.

[13] A. Paolella *et al.*, “A review on hexacyanoferrate-based materials for energy storage and smart windows: challenges and perspectives,” *J. Mater. Chem. A*, 2017.

[14] J. Woodward, “Praeparatio Caerulei Prussiaci Ex Germania Missa ad Johannem Woodward, M.D. Prof. Med. Gresh. R.S.S.,” *Philos. Trans. R. Soc. London*, vol. 33, pp. 15–17, 1724.

[15] “Under the Wave off Kanagawa (Kanagawa oki nami ura), also known as The Great Wave, from the series Thirty-six Views of Mount Fuji (Fugaku sanjūrokkei) | Katsushika Hokusai | JP1847 | Work of Art | Heilbrunn Timeline of Art History | The Metropolitan Museum of Art.” [Online]. Available: http://www.metmuseum.org/toah/works-of-art/JP1847/. [Accessed: 19-Sep-2017].

[16] J. F. Keggin and F. D. Miles, “Structures and Formulae of the Prussian Blues and Related Compounds,” *Nature*, vol. 137, pp. 577–578, 1936.

[17] H. J. Buser, D. Schwarzenbach, W. Petter, and A. Ludi, “The crystal structure of Prussian Blue: $Fe_4[Fe(CN)_6]_3.xH_2O$,” *Inorg. Chem.*, vol. 16, no. 11, pp. 2704–2710, Nov. 1977.

[18] F. Herren, P. Fischer, A. Ludi, and W. Haelg, “Neutron diffraction study of Prussian Blue, $Fe_4[Fe(CN)_6]_3.xH_2O$. Location of water molecules and long-range magnetic order,” *Inorg. Chem.*, vol. 19, no. 4, pp. 956–959, Apr. 1980.

[19] P. J. Kulesza *et al.*, “Electrochemical Charging, Countercation Accommodation, and Spectrochemical Identity of Microcrystalline Solid Cobalt Hexacyanoferrate,” *J. Phys. Chem. B*, vol. 102, pp. 1870–1876, 1998.

[20] A. L. Crumbliss, P. S. Lugg, J. W. Childers, and R. A. Palmer, “Fourier Transform Infrared Photothermal Spectroscopic Characterization of Prussian Blue Surface Modified Electrodes. Countercation Effects,” *J . Phys. Chem*, vol. 89, pp. 482–488, 1985.

[21] S. Ferlay, T. Mallah, R. Ouahès, P. Veillet, and M. Verdaguer, “A room-temperature organometallic magnet based on Prussian blue,” *Nature*, vol. 378, no. 6558, pp. 701–703, Dec. 1995.

[22] M. Verdaguer and G. S. Girolami, “Magnetic Prussian Blue Analogs,” in *Magnetism: Molecules to Materials V*, Weinheim, FRG: Wiley-VCH Verlag GmbH & Co. KGaA, 2005, pp. 283–346.

[23] A. Ludi and H. U. Güdel, “Structural Chemistry of Polynuclear Transition Metal Cyanides,” *Struct. Bond.*, vol. 14, no. 1–21, 1973.

[24] F. Ma, Q. Li, T. Wang, H. Zhang, and G. Wu, “Energy storage materials derived from Prussian blue analogues,” *Sci. Bull.*, vol. 62, no. 5, pp. 358–368, Mar. 2017.

[25] J. R. Perumareddi, A. D. Liehr, and A. W. Adamson, “Ligand Field Theory of Transition Metal Cyanide Complexes. Part I. The Zero, One and Two Electron or Hole Configurations,” *J. Am. Chem. Soc.*, vol. 85, no. 3, pp. 249–259, 1963.

[26] D. M. DeLongchamp and P. T. Hammond, “High-Contrast Electrochromism and Controllable Dissolution of Assembled Prussian Blue/Polymer Nanocomposites,” *Adv. Funct. Mater.*, vol. 14, no. 3, pp. 224–232, Mar. 2004.

[27] A. A. Karyakin, O. V. Gitelmacher, and E. E. Karyakina, “Prussian Blue-Based First-Generation Biosensor. A Sensitive Amperometric Electrode for Glucose,” *Anal. Chem.*, vol. 67, no. 14, pp. 2419–2423, Jul. 1995.

[28] F. Ricci and G. Palleschi, “Sensor and biosensor preparation, optimisation and applications of Prussian Blue modified electrodes,” *Biosens. Bioelectron.*, vol. 21, no. 3, pp. 389–407, Sep. 2005.

[29] A. A. Karyakin, “Prussian Blue and Its Analogues: Electrochemistry and Analytical Applications,” *Electroanalysis*, vol. 13, no. 10, pp. 813–819, 2001.

[30] N. R. de Tacconi, K. Rajeshwar, and R. O. Lezna, “Metal Hexacyanoferrates: Electrosynthesis, in Situ Characterization, and Applications,” *Chem. Mater.*, vol. 15, pp. 3046–3062, 2003.

[31] L. Boudjema, E. Mamontova, J. Long, J. Larionova, Y. Guari, and P. Trens, “Prussian Blue Analogues for the Separation of Hydrocarbons in Humid Conditions,” *Inorg. Chem.*, vol.

56, no. 14, pp. 7598–7601, Jul. 2017.

[32] P. K. Thallapally, R. K. Motkuri, C. A. Fernandez, B. P. McGrail, and G. S. Behrooz, "Prussian Blue Analogues for CO_2 and SO_2 Capture and Separation Applications," *Inorg. Chem.*, vol. 49, no. 11, pp. 4909–4915, Jun. 2010.

[33] S. G. Ferrón, "Novel Molecular Catalysts for Water Oxidation : Towards Artificial Photosynthesis," Universitat Rovira I Virgili, 2013.

[34] J. H. Swinehart, "The nitroprusside ion," *Coord. Chem. Rev.*, vol. 2, no. 4, pp. 385–402, Dec. 1967.

[35] W. P. Griffith, "Cyanide complexes of the early transition metals (groups IVa-VIIa)," *Coord. Chem. Rev.*, vol. 17, no. 2–3, pp. 177–247, 1975.

[36] R. P. Cheney, M. G. Simic, M. Z. Hoffman, I. A. Taub, and K. U. Asmus, "One- electron reduction of pentacyanonitrosylferrate(II) ion in aqueous solution," *Inorg. Chem.*, vol. 16, pp. 2187–2192, 1977.

[37] H. E. Toma and J. M. Malin, "Properties and reactivity of some pentacyanoferrate(II) complexes of aromatic nitrogen heterocycles," *Inorg. Chem.*, vol. 12, no. 5, pp. 1039–1045, May 1973.

[38] H. E. Toma and J. M. Malin, "Kinetics of formation and stability constants of some pentacyanoferrate(II) complexes of aromatic nitrogen heterocycles," *Inorg. Chem.*, vol. 12, no. 9, pp. 2080–2083, Sep. 1973.

[39] H. Toma, A. A. Batista, and H. B. Gray, "Pentacyanoferrate(II) complexes of amino acids," *J. Am. Chem. Soc.*, vol. 104, no. 26, pp. 7509–7515, Dec. 1982.

[40] A. E. Almaraz, L. A. Gentil, L. M. Baraldo, and J. A. Olabe, "Mixed-Valence Cyanopyridine-Bridged Complexes of Pentacyanoferrate and Pentaammineruthenium: Electronic Structure, Stability, and Redox Reactivity," *Inorg. Chem.*, vol. 35, no. 26, pp. 7718–7727, 1996.

[41] D. H. Macartney, "Properties and Reactions of Substituted Pentacyanoferrate (II) Complexes," *Rev. Inorg. Chem.*, vol. 9, no. 2–3, pp. 101–152, Jan. 1988.

[42] R. McHale, N. Ghasdian, Y. Liu, H. Wang, Y. Miao, and X. Wang, "Synthesis of Prussian Blue Coordination Polymer Nanocubes via Confinement of the Polymerization Field Using Miniemulsion Periphery Polymerization (MEPP)," *Macromol. Rapid Commun.*, vol. 31, no. 9–10, pp. 856–860, May 2010.

[43] G. Liang, J. Xu, and X. Wang, "Synthesis and Characterization of Organometallic Coordination Polymer Nanoshells of Prussian Blue Using Miniemulsion Periphery Polymerization (MEPP)," *J. Am. Chem. Soc.*, vol. 131, no. 15, pp. 5378–5379, Apr. 2009.

[44] S. Ye *et al.*, "Photoluminescent properties of Prussian Blue (PB) nanoshells and polypyrrole (PPy)/PB core/shell nanoparticles prepared via miniemulsion (periphery) polymerization," *Chem. Commun.*, vol. 47, no. 24, p. 6831, 2011.

[45] Y. Liu and X. Wang, "Synthesis, characterization, micellization and metal coordination polymerization of pentacyanoferrate-coordinated block copolymers for monodispersed soluble Prussian blue nanospheres," *Polym. Chem.*, vol. 3, no. 9, pp. 2632–2639, 2012.

[46] N. Ghasdian, Y. Liu, R. McHale, J. He, Y. Miao, and X. Wang, "Synthesis of Prussian Blue Metal Coordination Polymer Nanocubes via Cyanoferrate Monomer Design," *J. Inorg. Organomet. Polym. Mater.*, vol. 23, no. 1, pp. 111–118, Jan. 2013.

[47] M. Aksoy, S. V. K. Nune, and F. Karadas, “A Novel Synthetic Route for the Preparation of an Amorphous Co/Fe Prussian Blue Coordination Compound with High Electrocatalytic Water Oxidation Activity,” *Inorg. Chem.*, vol. 55, no. 9, pp. 4301–4307, May 2016.

[48] P.-Y. Chen, C.-S. Chen, and T.-H. Yeh, “Organic multiviologen electrochromic cells for a color electronic display application,” *J. Appl. Polym. Sci.*, vol. 131, no. 13, p. 40485, Jul. 2014.

[49] A. Kavanagh, K. J. Fraser, R. Byrne, and D. Diamond, “An Electrochromic Ionic Liquid: Design, Characterization, and Performance in a Solid-State Platform,” *ACS Appl. Mater. Interfaces*, vol. 5, no. 1, pp. 55–62, Jan. 2013.

[50] J. Goldemberg, “Energy Needs in Developing Countries and Sustainability,” *Science (80-.).*, vol. 269, no. 5227, pp. 1058–1059, 1995.

[51] M. Hoel and K. Snorre, “Depletion of fossil fuels and the impacts of global warming,” *Resour. Energy Econ.*, vol. 18, pp. 115–136, 1996.

[52] M. Höök and X. Tang, “Depletion of fossil fuels and anthropogenic climate change—A review,” *Energy Policy*, vol. 52, pp. 797–809, Jan. 2013.

[53] L. Schlapbach and A. Züttel, “Hydrogen-storage materials for mobile applications,” *Nature*, vol. 414, no. 6861, pp. 353–358, Nov. 2001.

[54] D. J. Durbin and C. Malardier-Jugroot, “Review of hydrogen storage techniques for on board vehicle applications,” *Int. J. Hydrogen Energy*, vol. 38, no. 34, pp. 14595–14617, Nov. 2013.

[55] A. Llobet and F. Meyer, “Water Oxidation in the Context of the Energy Challenge: Tailored

Transition- Metal Catalysts for Oxygen-Oxygen Bond Formation," *Angew. Chemie - Int. Ed.*, vol. 50, pp. A30–A33, 2011.

[56] N. S. Lewis, "Research opportunities to advance solar energy utilization," *Science (80-.).*, vol. 351, no. 6271, p. aad1920-9, 2016.

[57] J. Marshall, "Solar energy: Springtime for the artificial leaf," *Nature*, vol. 510, no. 7503, pp. 22–24, Jun. 2014.

[58] J. R. McKone, N. S. Lewis, and H. B. Gray, "Will Solar-Driven Water-Splitting Devices See the Light of Day?," *Chem. Mater.*, vol. 26, no. 1, pp. 407–414, Jan. 2014.

[59] M. G. Walter *et al.*, "Solar Water Splitting Cells," *Chem. Rev.*, vol. 110, no. 11, pp. 6446–6473, Nov. 2010.

[60] K. J. Young *et al.*, "Light-driven water oxidation for solar fuels," *Coord. Chem. Rev.*, vol. 256, no. 21–22, pp. 2503–2520, Nov. 2012.

[61] M. E. G. Lyons and M. P. Brandon, "A comparative study of the oxygen evolution reaction on oxidised nickel, cobalt and iron electrodes in base," *J. Electroanal. Chem.*, vol. 641, pp. 119–130, 2010.

[62] R. D. L. Smith *et al.*, "Photochemical Route for Accessing Amorphous Metal Oxide Materials for Water Oxidation Catalysis," *Science (80-.).*, vol. 340, no. 6128, pp. 60–63, 2013.

[63] Y. Surendranath, M. Dinca, and D. G. Nocera, "Electrolyte-Dependent Electrosynthesis and Activity of Cobalt-Based Water Oxidation Catalysts," *J. Am. Chem. Soc.*, vol. 131, no. 7, pp. 2615–2620, Feb. 2009.

[64] S. Jung, C. C. L. McCrory, I. M. Ferrer, J. C. Peters, and T. F. Jaramillo, “Benchmarking nanoparticulate metal oxide electrocatalysts for the alkaline water oxidation reaction,” *J. Mater. Chem. A*, vol. 4, no. 8, pp. 3068–3076, 2016.

[65] C. C. L. McCrory, S. Jung, I. M. Ferrer, S. M. Chatman, J. C. Peters, and T. F. Jaramillo, “Benchmarking Hydrogen Evolving Reaction and Oxygen Evolving Reaction Electrocatalysts for Solar Water Splitting Devices,” *J. Am. Chem. Soc.*, vol. 137, pp. 4347–4357, 2015.

[66] Gurudayal *et al.*, “Perovskite–Hematite Tandem Cells for Efficient Overall Solar Driven Water Splitting,” *Nano Lett.*, vol. 15, no. 6, pp. 3833–3839, Jun. 2015.

[67] A. Kudo, H. Kato, and S. Nakagawa, “Water Splitting into H_2 and O_2 on New $Sr_2M_2O_7$ (M = Nb and Ta) Photocatalysts with Layered Perovskite Structures: Factors Affecting the Photocatalytic Activity,” *J. Phys. Chem. B*, vol. 104, no. 3, pp. 571–575, 2000.

[68] J. Suntivich, K. J. May, H. A. Gasteiger, J. B. Goodenough, and Y. Shao-Horn, “A Perovskite Oxide Optimized for Oxygen Evolution Catalysis from Molecular Orbital Principles,” *Science (80-.).*, vol. 334, no. 6061, pp. 1383–1385, 2011.

[69] Y. Zhang, C. Zhao, X. Dai, H. Lin, B. Cui, and J. Li, “Amorphous cobalt potassium phosphate microclusters as efficient photoelectrochemical water oxidation catalyst,” *J. Power Sources*, vol. 243, pp. 908–912, Dec. 2013.

[70] L. G. Bloor, P. I. Molina, M. D. Symes, and L. Cronin, “Low pH Electrolytic Water Splitting Using Earth-Abundant Metastable Catalysts That Self-Assemble in Situ,” *J. Am. Chem. Soc.*, vol. 136, no. 8, pp. 3304–3311, Feb. 2014.

[71] T. Reier, M. Oezaslan, and P. Strasser, “Electrocatalytic Oxygen Evolution Reaction (OER) on Ru, Ir, and Pt Catalysts: A Comparative Study of Nanoparticles and Bulk Materials,” *ACS Catal.*, vol. 2, no. 8, pp. 1765–1772, Aug. 2012.

[72] B. Nepal and S. Das, “Sustained Water Oxidation by a Catalyst Cage-Isolated in a Metal-Organic Framework,” *Angew. Chemie Int. Ed.*, vol. 52, no. 28, pp. 7224–7227, Jul. 2013.

[73] Y. Gong *et al.*, “Two Co ^{II} Metal-Organic Frameworks Based on a Multicarboxylate Ligand as Electrocatalysts for Water Splitting,” *Chempluschem*, vol. 79, no. 2, pp. 266–277, Feb. 2014.

[74] Y. Matsumoto and E. Sato, “Electrocatalytic properties of transition metal oxides for oxygen evolution reaction,” *Mater. Chem. Phys.*, vol. 14, no. 5, pp. 397–426, May 1986.

[75] D. E. Hall, “Alkaline Water Electrolysis Anode Materials,” *J. Electrochem. Soc.*, vol. 132, no. 2, p. 41C–48C, 1985.

[76] J. R. Galán-Mascarós, “Water Oxidation at Electrodes Modified with Earth-Abundant Transition-Metal Catalysts,” *ChemElectroChem*, vol. 2, no. 1, pp. 37–50, 2015.

[77] C. C. L. McCrory, S. Jung, J. C. Peters, and T. F. Jaramillo, “Benchmarking Heterogeneous Electrocatalysts for the Oxygen Evolution Reaction,” *J. Am. Chem. Soc.*, vol. 135, no. 45, pp. 16977–16987, Nov. 2013.

[78] Z. Chen, A. R. Rathmell, S. Ye, A. R. Wilson, and B. J. Wiley, “Optically Transparent Water Oxidation Catalysts Based on Copper Nanowires,” *Angew. Chemie Int. Ed.*, vol. 52, no. 51, pp. 13708–13711, Dec. 2013.

[79] D. Ressnig *et al.*, “Photochemical and electrocatalytic water oxidation activity of cobalt

carbodiimide," *J. Mater. Chem. A*, vol. 3, no. 9, pp. 5072–5082, 2015.

[80] S. V. K. Nune, A. T. Basaran, R. Mishra, and F. Karadas, "Metal Dicyanamides as Efficient and Robust Water Oxidation Catalysts," *ChemCatChem*, vol. 9, pp. 300–307, 2017.

[81] S. Pintado, S. Goberna-Ferrón, E. C. Escudero-Adán, and J. R. Galán-Mascarós, "Fast and Persistent Electrocatalytic Water Oxidation by Co–Fe Prussian Blue Coordination Polymers," *J. Am. Chem. Soc.*, vol. 135, no. 36, pp. 13270–13273, Sep. 2013.

[82] S. Goberna-Ferrón, W. Y. Hernandez, B. Rodriguez-Garcia, and J. R. Galan-Mascaros, "Light-Driven water Oxidation with Metal Hexacyanoletallate Heterogeneous Catalysts," *ACS Catal.*, vol. 4, pp. 1637–1641, 2014.

[83] L. Han *et al.*, "Enhanced Activity and Acid pH Stability of Prussian Blue-type Oxygen Evolution Electrocatalysts Processed by Chemical Etching," *J. Am. Chem. Soc.*, vol. 138, no. 49, pp. 16037–16045, Dec. 2016.

[84] Y. Yamada, M. Yoneda, and S. Fukuzumi, "A Robust One-Compartment Fuel Cell with a Polynuclear Cyanide Complex as a Cathode for Utilizing H2O2 as a Sustainable Fuel at Ambient Conditions," *Chem. - A Eur. J.*, vol. 19, no. 35, pp. 11733–11741, Aug. 2013.

[85] Y. Yamada, K. Oyama, R. Gates, and S. Fukuzumi, "High catalytic activity of heteropolynuclear cyanide complexes containing cobalt and platinum ions: Visible-light driven water oxidation," *Angew. Chemie - Int. Ed.*, vol. 54, no. 19, pp. 5613–5617, 2015.

[86] Y. Yamada *et al.*, "Photocatalytic water oxidation by persulphate with a Ca^{2+} ion-incorporated polymeric cobalt cyanide complex affording O_2 with 200% quantum efficiency," *Chem. Commun.*, vol. 53, no. 24, pp. 3418–3421, Mar. 2017.

[87] R. Paggiaro, P. Bénard, and W. Polifke, “Cryo-adsorptive hydrogen storage on activated carbon. I: Thermodynamic analysis of adsorption vessels and comparison with liquid and compressed gas hydrogen storage,” *Int. J. Hydrogen Energy*, vol. 35, no. 2, pp. 638–647, Jan. 2010.

[88] B. Weinberger and F. D. Lamari, “High pressure cryo-storage of hydrogen by adsorption at 77K and up to 50MPa,” *Int. J. Hydrogen Energy*, vol. 34, no. 7, pp. 3058–3064, Apr. 2009.

[89] R. K. Ahluwalia *et al.*, “Technical assessment of cryo-compressed hydrogen storage tank systems for automotive applications,” *Int. J. Hydrogen Energy*, vol. 35, no. 9, pp. 4171–4184, May 2010.

[90] L. Wang, C. Zheng, R. Li, B. Chen, and Z. Wei, “Numerical analysis of temperature rise within 70 MPa composite hydrogen vehicle cylinder during fast refueling,” *J. Cent. South Univ.*, vol. 21, no. 7, pp. 2772–2778, Jul. 2014.

[91] M. T. I. Khan, M. Monde, and T. Setoguchi, “Hydrogen gas filling into an actual tank at high pressure and optimization of its thermal characteristics,” *J. Therm. Sci.*, vol. 18, no. 3, pp. 235–240, Sep. 2009.

[92] M. T. M. Koper and E. Bouwman, “Electrochemical Hydrogen Production: Bridging Homogeneous and Heterogeneous Catalysis,” *Angew. Chemie Int. Ed.*, vol. 49, no. 22, pp. 3723–3725, Apr. 2010.

[93] R. Parsons, “The rate of electrolytic hydrogen evolution and the heat of adsorption of hydrogen,” *Trans. Faraday Soc.*, vol. 54, pp. 1053–1063, Jan. 1958.

[94] L. D. Burke, N. S. Naser, and B. M. Ahern, “Use of iridium oxide films as hydrogen gas

evolution cathodes in aqueous media," *J. Solid State Electrochem.*, vol. 11, no. 5, pp. 655–666, Feb. 2007.

[95] J. Durst, C. Simon, F. Hasche, and H. A. Gasteiger, "Hydrogen Oxidation and Evolution Reaction Kinetics on Carbon Supported Pt, Ir, Rh, and Pd Electrocatalysts in Acidic Media," *J. Electrochem. Soc.*, vol. 162, no. 1, pp. F190–F203, Dec. 2015.

[96] W. Sheng, H. A. Gasteiger, and Y. Shao-Horn, "Hydrogen Oxidation and Evolution Reaction Kinetics on Platinum: Acid vs Alkaline Electrolytes," *J. Electrochem. Soc.*, vol. 157, no. 11, pp. B1529–B1536, Nov. 2010.

[97] S. Rioual, B. Lescop, F. Quentel, and F. Gloaguen, "A molecular material based on electropolymerized cobalt macrocycles for electrocatalytic hydrogen evolution," *Phys. Chem. Chem. Phys.*, vol. 17, no. 20, pp. 13374–13379, May 2015.

[98] F. Gloaguen and T. B. Rauchfuss, "Small molecule mimics of hydrogenases: hydrides and redox," *Chem. Soc. Rev.*, vol. 38, no. 1, pp. 100–108, Dec. 2009.

[99] M. Wang, L. Chen, and L. Sun, "Recent progress in electrochemical hydrogen production with earth-abundant metal complexes as catalysts," *Energy Environ. Sci.*, vol. 5, no. 5, pp. 6763–6778, Apr. 2012.

[100] V. S. Thoi, Y. Sun, J. R. Long, and C. J. Chang, "Complexes of earth-abundant metals for catalytic electrochemical hydrogen generation under aqueous conditions," *Chem. Soc. Rev.*, vol. 42, no. 6, pp. 2388–2400, Feb. 2013.

[101] S. Losse, J. G. Vos, and S. Rau, "Catalytic hydrogen production at cobalt centres," *Coord. Chem. Rev.*, vol. 254, no. 21–22, pp. 2492–2504, Nov. 2010.

[102] V. Artero, M. Chavarot-Kerlidou, and M. Fontecave, “Splitting Water with Cobalt,” *Angew. Chemie Int. Ed.*, vol. 50, no. 32, pp. 7238–7266, Aug. 2011.

[103] E. S. Wiedner and R. M. Bullock, “Electrochemical Detection of Transient Cobalt Hydride Intermediates of Electrocatalytic Hydrogen Production,” *J. Am. Chem. Soc.*, vol. 138, no. 26, pp. 8309–8318, Jul. 2016.

[104] W. K. C. Lo *et al.*, “Synthesis, Characterization, and Photocatalytic H2-Evolving Activity of a Family of $[Co(N_4Py)(X)]^{n+}$ Complexes in Aqueous Solution,” *Inorg. Chem.*, vol. 55, no. 9, pp. 4564–4581, May 2016.

[105] B. Kandemir, L. Kubie, Y. Guo, B. Sheldon, and K. L. Bren, “Hydrogen Evolution from Water under Aerobic Conditions Catalyzed by a Cobalt ATCUN Metallopeptide,” *Inorg. Chem.*, vol. 55, no. 4, pp. 1355–1357, Feb. 2016.

[106] Y. Sun, J. P. Bigi, N. A. Piro, M. L. Tang, J. R. Long, and C. J. Chang, “Molecular Cobalt Pentapyridine Catalysts for Generating Hydrogen from Water,” *J. Am. Chem. Soc.*, vol. 133, no. 24, pp. 9212–9215, Jun. 2011.

[107] S. Cobo *et al.*, “A Janus cobalt-based catalytic material for electro-splitting of water,” *Nat. Mater.*, vol. 11, pp. 802–807, 2012.

[108] Y. Sun *et al.*, “Electrodeposited Cobalt-Sulfide Catalyst for Electrochemical and Photoelectrochemical Hydrogen Generation from Water,” *J. Am. Chem. Soc.*, vol. 135, no. 47, pp. 17699–17702, Nov. 2013.

[109] R. S. Khnayzer *et al.*, “Towards a comprehensive understanding of visible-light photogeneration of hydrogen from water using cobalt(ii) polypyridyl catalysts,” *Energy*

Environ. Sci., vol. 7, no. 4, pp. 1477–1488, Mar. 2014.

[110] S. S. Kaye and J. R. Long, "Hydrogen Storage in the Dehydrated Prussian Blue Analogues M3[Co(CN)6]2 (M = Mn, Fe, Co, Ni, Cu, Zn)," *J. Am. Chem. Soc.*, vol. 127, no. 18, pp. 6506–6507, 2005.

[111] M. R. Hartman, V. K. Peterson, and Y. Liu, "Neutron Diffraction and Neutron Vibrational Spectroscopy Studies of Hydrogen Adsorption in the Prussian Blue Analogue Cu3[Co(CN)6]2," *Chem. Mater.*, vol. 18, no. 14, pp. 3221–3224, 2006.

[112] T. Abe, F. Taguchi, S. Tokita, and M. Kaneko, "Prussian White as a highly active molecular catalyst for proton reduction," *J. Mol. Catal. A Chem.*, vol. 126, no. 2–3, pp. L89–L92, Dec. 1997.

[113] G. Brauer, *Handbook of Preparative Inorganic Chemistry Volume 1*, 2nd ed. New York: Academic Press, 1963.

[114] D. J. Wasylenko, C. Ganesamoorthy, J. Borau-Garcia, and C. P. Berlinguette, "Electrochemical evidence for catalytic water oxidation mediated by a high-valent cobalt complex," *Chem. Commun.*, vol. 47, no. 14, pp. 4249–4251, Mar. 2011.

[115] S. Goberna-Ferrón, W. Y. Hernández, B. Rodríguez-García, and J. R. Galán-Mascarós, "Light-Driven Water Oxidation with Metal Hexacyanometallate Heterogeneous Catalysts," *ACS Catal.*, vol. 4, no. 6, pp. 1637–1641, Jun. 2014.

[116] S. Gupta *et al.*, "Co–Ni–B nanocatalyst for efficient hydrogen evolution reaction in wide pH range," *Appl. Catal., B*, vol. 192, pp. 126–133, 2016.

[117] Y. Sun *et al.*, "Electrodeposited Cobalt-Sulfide Catalyst for Electrochemical and

Photoelectrochemical Hydrogen Generation from Water," *J. Am. Chem. Soc.*, vol. 135, no. 47, pp. 17699–17702, Nov. 2013.

[118] J. Tian, Q. Liu, A. M. Asiri, and X. Sun, "Self-Supported Nanoporous Cobalt Phosphide Nanowire Arrays: An Efficient 3D Hydrogen-Evolving Cathode over the Wide Range of pH 0–14," *J. Am. Chem. Soc.*, vol. 136, no. 21, pp. 7587–7590, May 2014.

[119] J. Tian, Q. Liu, Y. Liang, Z. Xing, A. M. Asiri, and X. Sun, "FeP Nanoparticles Film Grown on Carbon Cloth: An Ultrahighly Active 3D Hydrogen Evolution Cathode in Both Acidic and Neutral Solutions," *ACS Appl. Mater. Interfaces*, vol. 6, no. 23, pp. 20579–20584, Dec. 2014.

[120] Z. Peng, D. Jia, A. M. Al-Enizi, A. A. Elzatahry, and G. Zheng, "Electrocatalysts: From Water Oxidation to Reduction: Homologous Ni-Co Based Nanowires as Complementary Water Splitting Electrocatalysts" *Adv. Energy Mater.*, vol. 5, no. 9, pp. 1402031–1402037, May 2015.

[121] Z. Pu, Q. Liu, P. Jiang, A. M. Asiri, A. Y. Obaid, and X. Sun, "CoP Nanosheet Arrays Supported on a Ti Plate: An Efficient Cathode for Electrochemical Hydrogen Evolution," *Chem. Mater.*, vol. 26, no. 15, pp. 4326–4329, Aug. 2014.

[122] H.-W. Liang, X. Zhuang, S. Brüller, X. Feng, and K. Müllen, "Hierarchically porous carbons with optimized nitrogen doping as highly active electrocatalysts for oxygen reduction," *Nat. Commun.*, vol. 5, pp. 1–7, 2014.

[123] Y. Pan, Y. Lin, Y. Chen, Y. Liu, and C. Liu, "Cobalt phosphide-based electrocatalysts: synthesis and phase catalytic activity comparison for hydrogen evolution," *J. Mater. Chem. A*, vol. 4, no. 13, pp. 4745–4754, 2016.

[124] S. Rioual, B. Lescop, F. Quentel, and F. Gloaguen, “A molecular material based on electropolymerized cobalt macrocycles for electrocatalytic hydrogen evolution,” *Phys. Chem. Chem. Phys.*, vol. 17, no. 20, pp. 13374–13379, 2015.

[125] D. Kong, H. Wang, Z. Lu, and Y. Cui, “$CoSe_2$ Nanoparticles Grown on Carbon Fiber Paper: An Efficient and Stable Electrocatalyst for Hydrogen Evolution Reaction,” *J. Am. Chem. Soc.*, vol. 136, no. 13, pp. 4897–4900, Apr. 2014.

[126] Z. Chen, D. Cummins, B. N. Reinecke, E. Clark, M. K. Sunkara, and T. F. Jaramillo, “Core–shell MoO_3 –MoS_2 Nanowires for Hydrogen Evolution: A Functional Design for Electrocatalytic Materials,” *Nano Lett.*, vol. 11, no. 10, pp. 4168–4175, Oct. 2011.

[127] S. Cobo *et al.*, “A Janus cobalt-based catalytic material for electro-splitting of water,” *Nat. Mater.*, vol. 11, no. 9, pp. 802–807, 2012.

APPENDIX

ELECTROCHEMISTRY TERMS and EXPERIMENTS

An electrochemical **cell** is a device where oxidation and reduction reactions occur. Oxidation takes place at the anode compartment and reduction occurs at the cathode.[1]

Electrolyte contains ions in order to minimize the effect of migration and reducing the resistance of the solution. In this thesis, 1 M KNO_3 used as supporting electrolyte for all of electrochemical experiments. It is added into 50 mM KPi buffer solution.[2]

Overpotential (η) is the difference between intrinsic thermodynamic potential and the applied potential ($\eta = E_{applied} - E^o$) shows the driving force needed to flow current through the system.[3]

Onset potential is the potential where the current sharply starts to increase. It is a good indication of the catalytic activity.[4]

Faradaic efficiency is defined as the ratio of experimentally measured produced hydrogen or oxygen and theoretical amount of produced hydrogen or oxygen as Faraday's Law.[1]

$$\text{Faradaic Efficiency} = \frac{mol\ of\ oxygen\ evolved}{mol\ of\ theoretical\ oxygen} . 100\%$$

Surface Coverage Analysis: The number of electroactive Co^{2+} metal centers has been determined by performing cyclic voltammograms in 50 mM KPi buffer solution with 1 M KNO_3 at pH 7 with different sweep rates in a certain potential range where $Co^{2+/3+}$ redox pair is observed. In order to calculate the concentration of electroactive metal centers ($mol.cm^{-2}$), sweep rate versus current plot is drawn and the slope of this line gives the concentration:

$$Slope = \frac{n^2F^2A\Gamma o}{4RT}$$

Where F is Faraday's constant (96485 $C.mol^{-1}$), A is area, Γ_o is the surface coverage in the unit of $mol.cm^{-2}$. R stands for ideal gas constant, and T is temperature. [1]

Turnover Frequency (TOF) is the number of oxygen (WOC) or hydrogen (HEC) evolved per electroactive metal site per time. It is calculated according to the equation:

$$TOF = \frac{Mol\ of\ Oxygen\ evolved\ per\ second}{mol\ of\ active\ sites} = \frac{Q}{4t\Gamma}$$

Where Q is the charge accumulated (coulomb), t is time (s) and Γ is the surface coverage (mol.s^{-2}). [1], [5]

TOF value for a certain overpotential is calculated by plotting logarithm of TOF versus overpotential and it is calculated by the equation of the trendline of the graph in the Tafel region. For water oxidation catalysis, in order to ease the comparison of the values with the literature, 400 mV overpotential was used to calculate TOF.

Tafel Equation and Tafel Slope

Tafel analysis was performed by electrolysis experiment. Chronoamperometric measurements were conducted at each overpotential for 10 minutes in KPi buffer at pH 7. In order to obtain the value of Tafel slope, which is an important parameter to get insight about the mechanism of the reaction and identifying the rate determining step of the system, the logarithm of the densities of the final current values are plotted versus the overpotential. In the linear trend region, the catalyst shows catalytically active behavior (See Figure 3.6). The linear fit of this linear region is the Tafel equation of the system. Tafel slope is extracted from the Tafel equation.[6]

General form of Tafel Equation: **η=a+b log (j)** where η is overpotential, b is Tafel slope and j is current density. [7]

Pourbaix Diagram: Pourbaix Diagram shows the effect of pH on potential. For this experiment series of cyclic voltammograms were performed at different pH values (between 2-13). For the experiments KPi buffer solution with 1 M KNO_3 was used and pHs were adjusted as adding either KOH or H_3PO_4. The diagram was plotted pH vs. $E_{1/2}$. [8]

Long Term Stability Experiments: In order to check the stability of the catalyst chronoamperometric measurements were applied. Measurements were performed at -0.8 V & +1.2V (vs NHE) using for at least three days in 50 mM KPi solution with 1 M KNO_3 at pH 7.0, with intervals of 24 h. After every 24 hours a cyclic voltammograms were performed to check the stability of the catalysts.

Reference Electrode Potential Conversions

All of the experiments were performed with Ag/AgCl reference electrode (3.5 M KCl). All of the potentials were reported as normal hydrogen electrode (NHE) scale.

In order to convert the potentials, E (NHE) = E (Ag/AgCl) + 0.205 V is used since E (Ag/AgCl) (3.5 M KCl at 298 K) = 0.205 V [9]

References:

[1] S. G. Ferrón, "Novel Molecular Catalysts for Water Oxidation : Towards Artificial Photosynthesis," Universitat Rovira I Virgili, 2013.

[2] A. J. Bard and L. R. Faulkner, *Electrochemical Methods: Fundamentals and Applications*, 2nd ed. WILEY-VCH Verlag, 2001.

[3] V. S. Thoi, Y. Sun, J. R. Long, and C. J. Chang, "Complexes of earth-abundant metals for catalytic electrochemical hydrogen generation under aqueous conditions," *Chem. Soc. Rev. Chem. Soc. Rev*, vol. 42, no. 42, pp. 2388–2400, 2388.

[4] A. Maljusch, E. Ventosa, R. Rincon, A. Bandarenka, and W. Schuhmann, "Revealing onset potentials using electrochemical microscopy to assess the catalytic activity of gas-evolving electrodes," *Electrochem. commun.*, vol. 38, pp. 142–145, Jan. 2014.

[5] M. B. Stevens *et al.*, "Measurement Techniques for the Study of Thin Film Heterogeneous Water Oxidation Electrocatalysts," *Chem. Mater.*, vol. 29, no. 1, pp. 120–140, Jan. 2017.

[6] S. Pintado, S. Goberna-Ferrón, E. C. Escudero-Adán, and J. R. Galán-Mascarós, "Fast and Persistent Electrocatalytic Water Oxidation by Co–Fe Prussian Blue Coordination Polymers," *J. Am. Chem. Soc.*, vol. 135, no. 36, pp. 13270–13273, Sep. 2013.

[7] M. D. Kärkäs, O. Verho, E. V. Johnston, and B. Åkermark, "Artificial Photosynthesis :

Molecular Systems for Catalytic Water Oxidation," *Chem. Rev.*, vol. 114, pp. 11863–12001, 2014.

[8] D. J. Wasylenko, C. Ganesamoorthy, J. Borau-Garcia, and C. P. Berlinguette, "Electrochemical evidence for catalytic water oxidation mediated by a high-valent cobalt complex," *Chem. Commun.*, vol. 47, no. 14, pp. 4249–4251, Mar. 2011.

[9] Y. Sun *et al.*, "Electrodeposited cobalt-sulfide catalyst for electrochemical and photoelectrochemical hydrogen generation from water," *J. Am. Chem. Soc.*, vol. 135, no. 47, pp. 17699–17702, 2013.